©Copyright 2014
Phillip Miller

High Strain-Rate Material Behavior by Short Pulse Laser-Generated Stress Waves

Phillip Miller

A dissertation
submitted in partial fulfillment of the
requirements for the degree of

Doctor of Philosophy

University of Washington

2014

Reading Committee:

Junlan Wang, Chair

Mamidala Ramulu

Mark Tuttle

Program Authorized to Offer Degree:

Mechanical Engineering

University of Washington

Abstract

High Strain-Rate Material Behavior by Short Pulse Laser-Generated Stress Waves

Phillip Miller

Chair of the Supervisory Committee:
Professor Junlan Wang
Mechanical Engineering

The response of materials when subjected to high strain-rate, high pressure loading can vary drastically from static conditions. Dynamic material behavior arises whenever loading is suddenly applied to a material or structure and it is essential that this behavior is well understood for qualitative and quantitative predictability. Stress waves generated from tabletop short pulse lasers allows the study of material behavior in the pressure range of 10's GPa and strain-rates up to 10^8 s^{-1}. In this dissertation, a parametric study was first carried out to understand the effect of various parameters on the stress wave generation by laser pulse absorption. The technique was then applied to several material systems ranging from conventional solids such as Si and aluminum, to biological cells and further to nanoporous oxides, to understand their unique response under high strain-rate loading.

To better understand the applicability of the technique and the role of the loading parameters on stress generation, a parametric study of the laser fluence, pulse duration, and confinement of the laser absorption volume was performed. Similar stress profiles are observed under high fluence, confined conditions for lasers pulse durations spanning picoseconds to nanoseconds. Low fluence and unconfined absorption with picosecond laser pulses allows an order of magnitude enhancement in strain-rate, while still generating peak stresses relevant to dynamic material behavior.

Using the knowledge gained from the parametric study, high strain-rate compressive yielding of aluminum alloys subjected to picosecond and nanosecond pulsed laser loading reveals an elastic-plastic response consistent with observations from other experimental techniques at lower strain-rates. Stress wave evolution as a function of propagation was studied, and no additional rate dependence from picosecond to nanosecond loading was observed.

Previous application of the laser spallation technique was applied to measure the adhesion strength of cells on inorganic substrates. Due to the time scale of the interaction, post mortem observations were used to determine the loading required to remove the cells. Transient finite element analysis was carried out to investigate the detachment mechanism responsible for cell decohesion. Failure is driven by large interfacial strains experienced due to the very rapid acceleration of the substrate into the cell. Stress, strain, and interface failure evolution exhibit no rate or cell geometry dependence, indicating the laser spallation techniques ability to measure an intrinsic, undisturbed, and short time scale adhesion strength.

The final study conducted was the determination of the dynamic behavior of a novel material system, synthetic nanoporous zeolite, measured by laser-induced loading. High strain-rate loading prompts a ductile to brittle transition for zeolite. Compression experiments demonstrate brittle fracture under moderate loading of several hundred MPa. Spallation measurements were performed with peak stresses up to 3 GPa. A spallation strength of 215 MPa for bulk zeolite was measured, with no dependency on peak stress. The low spallation strength, as well as scanning electron microscope

observations of the spallation morphology, confirms that bulk zeolite behaves as the brittle solid at high strain-rates.

Dedication

To my family

Acknowledgements

While this dissertation represents the effort of the author, it nonetheless would not have been possible without the support of several key figures. First and foremost is my advisor, Prof. Junlan Wang, who has been mentoring me since being an undergraduate student. It was due to my early interaction with research in her group that I found my passion for experimental mechanics and the dynamic behavior of materials. Prof. Wang allowed me a great deal of freedom during my dissertation research and provided steadfast support.

Professors Mamidala Ramulu, Mark Tuttle, and Fumio Ohuchi provided invaluable feedback while serving as committee members, often raising issues which allowed me to come to a deeper understanding of my research. This dissertation benefitted greatly from their keen attention.

I would like to thank my labmates during my undergraduate and graduate tenure: Lili Hu, Mark Johnson, Jie Lian, Frank MacDonald, Elias Penilla, Wu-Feng Yeh, Gabe Chow, Zhou Yang, Mark Miller, and Melicent Stossel. The feedback gained in the lab and during group meetings greatly improved the quality of my research. Lili is owed deep gratitude for training me in the use of lasers and optics as well as collaboration on the experimental cell adhesion studies, which were the impetus for the numerical experiments. The training and help in synthesizing zeolite provided by Gabe saved me a great deal of time and effort when it mattered most during the final stages of my dissertation research.

The unwavering love, help, and encouragement of family and friends provided a deep pool of support which allowed steady progress until completion. Unfortunately, life generally demands a great deal more than just being a diligent student and dedicated researcher. The buffering provided by loved ones was as important to my success as my research progress, the latter being impossible without the former.

Financial support was instrumental in realization of this dissertation. Procurement of the magenetron sputtering system as well as the Contiuum Leopard SS-2 picosecond laser were made possible by DOD DURIP grants. Research into the behavior of synthetic zeolites and their applications was supported by the NSF. Finally, a Department of Education GAANN fellowship allowed the successful completion of this dissertation.

Table of Contents

List of Tables

List of Figures

Chapter 1. Introduction

1.1. Background

In many situations materials or structures are subjected to loading which may vary over time. How the load varies may strongly affect the response. For slowly varying loads the observed response may correspond to creep/relaxation for viscous materials, or static/quasi-static response for materials which do not exhibit a rate dependence. The time scale relevant for observation is also important, as objects that appear static on the second-hour-day time scale may behave dynamically on longer time scales. A dramatic example is the famous pitch drop experiment in the Department of Physics at the University of Queensland in Brisbane [1]. In this experiment (one of the longest running experiments to date), pitch (a viscoelastic, solid polymer tar derivative) was heated to a liquid and placed into a funnel in 1927 by Professor Thomas Parnell. The pitch was allowed to settle in a funnel for 3 years, then the funnel was cut open to allow the pitch to flow. It took 8 years for the first drop to fall. This is due to the very high viscosity of pitch, $2.3\times10^{8}\ \mathrm{Pa\cdot s}$ [1]. For comparison the viscosity of water is $1.0\times10^{-3}\ \mathrm{Pa\cdot s}$, eleven orders of magnitude smaller. To date only 8 drops have fallen, with the 9th drop imminent (months to years).

On the other side of the spectrum, loading may vary considerably over short periods of time. The example given in Marc Meyers' excellent book on the subject, *Dynamic Behavior of Materials* [2], is very illustrative and will be paraphrased here. An ordinary sand bag can effectively stop impact from a bullet with a velocity on the order of 1 mile/s. The same sandbag, though, is easily defeated with a

knife. Now consider instead a piece of wood or steel. A bullet would be able to pierce both (of moderate thickness), whereas the knife would be useless for penetration.

The difference between the pitch and knife versus the bullet is due to the dynamic nature of the bullet. Upon being fired the bullet is endowed with a high velocity, hence kinetic energy. By virtue of the principle of inertia, the bullet wants to keep moving even when it impacts another object. During impact the bullet's kinetic energy may be dissipated away by a variety of mechanisms including momentum transfer into the impacted object (i.e. the radiation of stress waves), deformation, and phase changes as the result of high pressures and temperatures. The large difference between the bullet impacting the sand bag and the wooden board is due to the sand's compaction, densification, and tendency to promote fragmentation of the bullet, delocalizing the dissipated energy, whereas the board is unable to dissipate the absorbed energy and retain integrity.

The critical factor controlling whether the response of the material is dynamic is that the rate of deformation is sufficiently high such that static equilibrium is not maintained throughout the material or structure. This rate of deformation is the strain-rate, and in general rates above 10^2 s^{-1} are considered dynamic or high strain-rate. The strain-rate regimes are typically separated into the categories of 10^2 $s^{-1} < \dot{\varepsilon} < 10^4$ s^{-1} for high strain-rate, 10^4 $s^{-1} < \dot{\varepsilon} < 10^6$ s^{-1} for very high-strain-rate, and $\dot{\varepsilon} > 10^6$ s^{-1} as ultra-high strain-rate [3]. This is shown schematically in Figure 1.1. The captioned boxes are some of the techniques for the different ranges of strain-rate and will be discussed in Chapter 2.

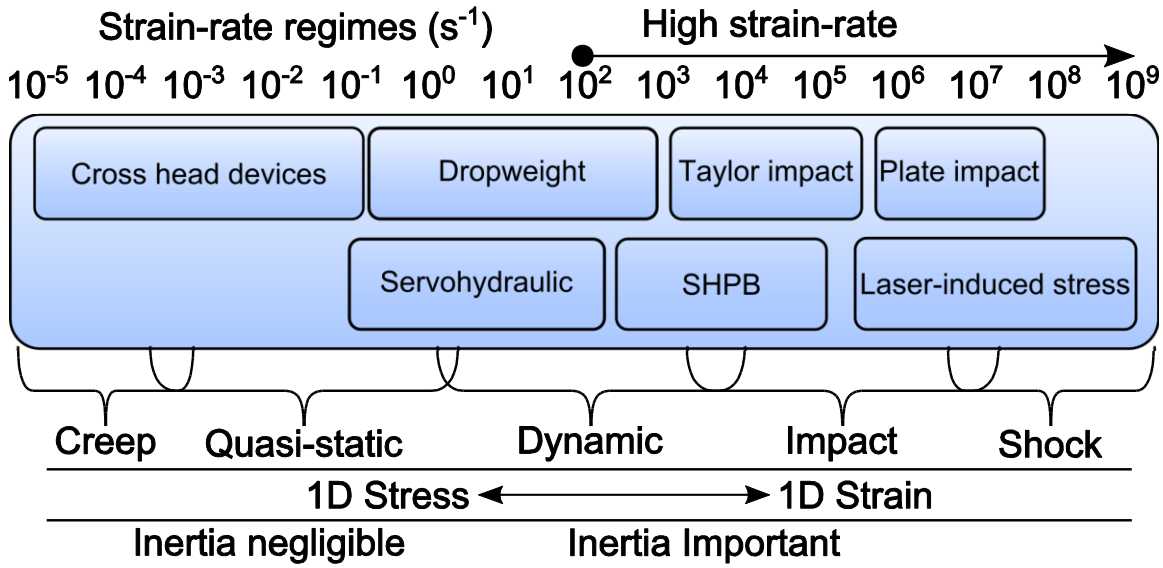

Figure 1.1: Schematic of strain-rate regimes and relevant experimental techniques, adapted from Field et al. [4].

Although some differences between low and high strain-rate behavior may be intuitive, what drives the need for distinguishing them is the observation of changes in material response, which can be drastic for some materials. It is not completely understood all the mechanisms which govern high strain-rate behavior. Most knowledge is confined to the specific material being investigated, with generalizations to the structure usually only qualitative in nature (e.g. BCC metals tend to be more rate and temperature sensitive than FCC metals). Campbell and Ferguson's now classic investigation into the rate and temperature dependence of strength in mild steel shows that the yield stress increases with strain-rate, and that the amount of increase depends on the temperature [5]. Specifically, there is a much greater increase in yield stress from low to high strain-rates at low temperature.

Even under static conditions the strength of a material is known to be influenced by work-hardening and temperature. Rate independent work hardening can be modeled by an empirical power law relationship of the form:

$$\sigma = \sigma_0 + K\varepsilon^n \tag{1}$$

where σ is the flow stress and is a function of the yield strength, σ_0 , and the strain, ε , to the power of n, known as the strain hardening coefficient, and K is a constant prefactor. A similar expression can be written for the effect of temperature, and is given by:

$$\sigma = \sigma_r \left[1 - T_{\mathrm{h}}^m\right] \tag{2}$$

where $T_{\mathrm{h}} = \dfrac{T - T_{\mathrm{r}}}{T_{\mathrm{m}} - T_{\mathrm{r}}}$ is the homologous reference temperature and is the ratio of the difference between the current temperature, T , and the reference temperature, T_{r} , and the melting temperature, T_{m} , and the reference temperature. σ_r is the reference stress and is measured at the reference temperature, and m is an experimentally determined constant. Finally, over many decades of strain-rate, e.g. $10^{-4}\ \mathrm{s}^{-1} < \dot{\varepsilon} < 10^{2}\ \mathrm{s}^{-1}$, stress is observed to vary with the logarithm of the strain-rate, $\sigma \propto \ln \dot{\varepsilon}$. Johnson et al. [6–8] combined these to form a work hardening, rate and temperature dependent empirical constitutive relation of the form:

$$\sigma = \left(\sigma_0 + B\varepsilon^n\right)\left(1 + C \ln \frac{\dot{\varepsilon}}{\dot{\varepsilon}_0}\right)\left[1 - T_{\mathrm{h}}^m\right] \tag{3}$$

Equation 3 is the Johnson-Cook model and is widely used due to its ability to describe a large variety of material behavior. A drawback of this model, though, is that all the parameters are coupled to one another, thus many experiments need to be performed in order to fit all the coefficients. It is also purely empirical, giving no insight into the underlying mechanisms governing the rate or temperature dependence. Fortunately, due to its designation as the "workhorse" model, coefficients are available for many materials. Many other empirical models have been developed, many with small variations to

Johnson-Cook, such as Andrade et al. [9] incorporating a reducer function to model the sudden loss of strength in oxygen-free high thermal conductivity copper at 600 K due to dynamic recrystallization.

Other models have been proposed which try to account for the underlying mechanisms governing rate dependent material behavior. For metals dislocation dynamics become more important as the strain-rate increases. The transition of rate dependence from low to high strain-rates, that is the often observed bilinear yield-strain-rate behavior, can be understood as the transition from thermally activated dislocation motion at low strain-rates, to dislocation drag at higher strain-rates [10]. The model of Zerilli and Armstrong [11] is based on thermally activated dislocation motion (itself a function of temperature, strain-rate, and the microstructure), athermal flow stress, (due to long range dislocation barriers), and grain boundary strengthening by reduced grain size through the Hall-Petch relationship.

$$\begin{aligned} &\text{FCC: } \sigma = \sigma_G + C_2\varepsilon^{1/2}\exp\left(-C_3T + C_4T\ln\dot{\varepsilon}\right) + kd^{-1/2} \\ &\text{BCC: } \sigma = \sigma_G + C_1\exp\left(-C_3T + C_4T\ln\dot{\varepsilon}\right) + C_5\varepsilon^n + kd^{-1/2} \end{aligned} \tag{4}$$

σ_G is the aforementioned athermal flow stress, $kd^{-1/2}$ is the Hall-Petch factor (with d as the grain diameter), $-C_3T + C_4T\ln\dot{\varepsilon}$ describes the rate and temperature dependence, and $\varepsilon^{1/2}$ or ε^n are the strain hardening components. A large part of the difference observed between BCC an FCC metals can be understood from short range dislocation barriers. For BCC metals the principle barrier is the Peierls-Nabarro barrier, which is the energy needed for the dislocation to move from one equilibrium position to the next. For FCC metals the dominant short range energy barrier is dislocation forests, which are dislocations moving in other slip planes. In the Zerilli-Armstrong model the thermally activated dislocation motion is different for BCC and FCC metals (see Equation 4). For BCC metals the strain-rate dependence is uncoupled to the plastic strain, whereas for FCC metals the thermally

activated barrier is dependent on the plastic strain. This is due to the Peierls-Nabarro barrier being due to the lattice (assumed to be independent of the strain), whereas forest dislocations are due to slip system interactions which inherently depends on strain.

Zerilli-Armstrong's model shows good agreement with experiments, but only up to strain-rates of the order 10^4 s^{-1}. This limitation is due to only considering thermally activated dislocation motion, which dominates when the applied loading and loading rate is comparable to the thermally activated barrier. When strain-rates are increased further, dislocation drag becomes dominant and needs to be accounted for accurate modeling of flow stress. Dislocation motion requires energy and much of this energy (up to 95% of the total energy) is dissipated as the dislocation moves [12]. This energy dissipation can be understood as viscous effects from the dislocation interactions during motion through the material. Parameswaran et al. [13] found that for aluminum the primary dissipative effects were due to phonon and electron viscosity. Phonon viscosity is due to the interaction of the dislocation with lattice vibrations (phonons), and electron viscosity is due to the dislocation interaction with electrons, mechanisms originally prosed by Mason [14] and Gilman [15]. Parameswaran et al. found that for low temperatures (<100 K), electron viscosity was dominant, and above this temperature phonon viscosity is significant. Another dislocation mechanism becomes important at high strain-rates and high applied loading. Under these conditions the dislocation velocity begins approaching the elastic shear wave speed. At these dislocation velocities relativistic effects (dislocation velocity relative to shear wave velocity) come into play and limit the maximum dislocation velocity. The essence of this mechanism is that the stress field (lattice displacements) which propagates the dislocation cannot be overtaken.

The shortcomings of predicting the mechanisms operating at strain-rates higher than $\dot{\varepsilon} \approx 10^4\ \mathrm{s}^{-1}$ from the most common flow stress models (i.e. Johnson-Cook[6–8], Steinberg-Guinan [16]) prompted Preston et al. [17] to formulate a physically based flow stress model incorporating the effects observed in the strong-shock-wave limit with those operating in the thermally activated regime. The Preston-Tonks-Wallace (PTW) model is a conditional model with an Arrhenius relation for the plastic strain-rate in the thermally activated regime, with work hardening that saturates as an error function. At very high strain-rates the saturation and yield stresses are given as a power law, with the exponent being near ¼. Transition between the two regimes is treated by conditional expressions of the form $\tau = \max\left\{\tau^L, \min\left[\tau^M, \tau^H\right]\right\}$, where τ is the flow stress, and τ^L, τ^M and τ^H are the flow stress prediction for low, medium, and high strain-rates (see Preston et al. [17] or Hanson [18] for full treatment). In total the PTW model has 13 parameters. Though this is more than double that of the previously mentioned models, PTW has the advantage of being a physically based model and some of the parameters can be estimated from the underlying mechanisms. Thus they can at least be reasonably estimated or inferred from similar materials, or determined independently (since the parameters are not coupled as they are for the Johnson-Cook model).

For all the proposed models experiments are needed to determine the model parameters and for validation, as it is generally desired to interpolate or extrapolate behavior between or outside of experimental conditions. Additionally, most of the model parameters cannot be obtained or estimated from other experiments. To date no theory or tools exist which can predict material behavior over the entire range of pressures and strain-rates of interest in dynamic material behavior. In general actual loading of a structure will provide a wide range of strain-rates and stresses. For example, ballistic

impact at velocities of 1-2 km/s will generate a peak strain-rates of the order of $\dot{\varepsilon} \approx 10^5 - 10^6\ \mathrm{s}^{-1}$ during initial contact, but considerable deformation may take place after impact and at lower strain-rates.

1.2. Overview of the Dissertation

This dissertation presents the results of studies of the laser spallation technique and its application to several material systems. Chapter 2 reviews experimental techniques that have been developed for investigating dynamic material behavior. The techniques are grouped by the different strain-rate regimes, with the ultra-high strain-rate regime discussed in the context of stress waves generated from short pulse lasers. Chapter 3 is a parametric study of the laser spallation technique. Effects of laser pulse duration and confinement of the laser-matter interaction volume are studied by measurement of the stress histories in single crystal Si substrates. Quantitative measurements are correlated with nanosecond time-resolved microscopy of the stress generating plasma blow-off process, as well as surface fracturing and spallation. In Chapter 4, the high strain-rate behavior of aluminum alloys from laser-generated stress waves is examined. These studies reveal that the elastic limit of aluminum alloys at ultra-high strain-rate is consistent with that observed at lower strain-rates. Chapter 5 details the results of a finite element simulation to understand the interfacial behavior and cell detachment process when the laser spallation technique is applied to measuring the adhesion of cells to inorganic substrates. The application of the laser spallation technique for studying the dynamic behavior of nanoporous zeolite is the focus of Chapter 6. Despite the large degree of porosity, bulk zeolite undergoes a ductile to brittle transition at high strain-rates and behaves as a brittle solid. The spallation strength of zeolite is measured, and the spallation features are discussed. Chapter 7 summarizes the major findings and presents some suggestions for future research directions.

Chapter 2. Literature Review

2.1. Review of Techniques Used for Dynamic Material Testing

As demonstrated in the introduction, there is a clear need to understand material behavior under dynamic, high pressure, high strain-rate conditions. Over the last century many techniques have been developed to assess material behavior under specific conditions. While some techniques are capable of loading a material in such a way as to elicit response covering a wide range of dynamic phenomenon, the interpretation of such tests is difficult and isolating key qualitative or quantitative features may be impossible. To remedy the difficulty of interpreting realistic and complex loading scenarios, experimental methods have been developed to isolate material behavior over a narrow range of conditions. This naturally splits the techniques into various ranges of strain-rates. The strain-rate is intimately connected to the duration and amplitude of the applied stress. The ramification of this is that for dynamic material testing, simultaneous high strain-rate, high strain, and high applied stress are very difficult to achieve. Most high strain-rate experiments are limited to either high applied stress, high strain-rate, and low strain, or high strain, low strain-rate, and low applied stress. Another implication of high strain-rates is that as the applied stress duration is shortened to raise the strain-rate, the ideal state of uniaxial stress transforms to one of uniaxial strain. This can have a dramatic effect on the observed material behavior and will be discussed in the ultra-high strain-rate section.

2.1.1. Intermediate Strain-Rates: $0.1 < \dot{\varepsilon} < 500\ \mathrm{s}^{-1}$

The intermediate strain-rate regime presents some unique challenges for experimentalists. In this regime effects due to wave propagation are relevant, but are difficult to account for [3]. This is due to speed of propagation in solid materials being on the order of 1000 m/s for elastic and plastic waves

and the characteristic time of these experiments can be as long as $1\ \text{ms}$, allowing wave propagation of distances of hundreds of meters. This requires much too large a sample for reasonable experimentation, so samples smaller than this are used and suffer from multiple transmissions and reflections at all boundaries. This effectively couples the test specimen with the testing device, so wave propagation and reverberation within the sample and vibration of testing structure constantly interact throughout the experiment. If the sample is small enough, such that the characteristic length, L, is much less than the wave propagation distance, $L \ll c \cdot \tau$, then a state of uniform stress can be achieved. When this is not true the individual waves need to be accounted for, or the strain-rate needs to be limited. The maximum applied stress is also limited, since if failure occurs at the location of the loading there is no way to extract the material behavior without measuring the failure wave. Nevertheless, a number of experimental methods have been developed for this strain-rate regime and will be briefly discussed.

A common instrument in this strain-rate regime is the servo-hydraulic load frame. These systems are very similar to conventional screw-driven cross head systems used for quasi-static testing, but use servo actuated hydraulics to apply a load. Typical systems are limited to strain-rates of $\dot{\varepsilon} \approx 1\ \text{s}^{-1}$, mostly due to the maximum velocity the system can achieve with loading. Specialized grips are required, which have slack in them and allow the system to accelerate before loading the specimen. Systems have been adapted with higher pressure and achieve higher velocities, allowing maximum strain-rates of $\dot{\varepsilon} \approx 10 - 100\ \text{s}^{-1}$. ASTM standard D3763 has been developed for using such machines to determine the puncture properties of plastics. The appendix of ASTM D3763 [19] contains a useful discussion on interpreting signal features due to inertial effects from acceleration loads, bending loads, or ringing due to vibration; due to possible fracture initiation and crack propagation; and due to failure modes

and processes. The discussion is only of qualitative features though, and no rigorous method is provided for extracting dynamic properties from these tests.

If higher strain-rates are required specialized instruments are needed. Extending the maximum strain-rate up to $\dot{\varepsilon} \approx 1000\ \mathrm{s}^{-1}$ are two similar systems which make use of a large rotating flywheel. The flywheels can be a meter or more in diameter (for tension experiments, typically smaller for compression) and rotate upwards of $1000\ \mathrm{RPM}$, resulting in a linear velocity of up to $100\ \mathrm{m/s}$. Once the flywheel is up to speed the loading fixture is actuated and engages the sample. The mass of the flywheel is sufficient to ensure a constant strain-rate throughout deformation. For compression testing there is the cam plastometer, in which the flywheel has a profile and rotates freely until a cam follower is inserted between the cam/flywheel and sample [20]. The specimen is then compressed against a load cell. The load cell output is combined with the known profile of the cam to obtain the stress-strain behavior. For tension testing instead of a cam and cam follower a hammer is employed. The hammer is in a retracted position as the flywheel accelerates up to the desired velocity. Then the hammer is released and extends outward due to inertia. A stop on the flywheel limits the rotation of the hammer and ensures even, planar contact. The sample lies in the path of the now extended hammer, which strikes an anvil attached to the bottom of the specimen. The displacement of an elastic bar or load measuring gauges near the gauge length measures forces in the sample, while the displacement at the bottom of the specimen, where the hammer contacts the anvil, is monitored for measurement of strain. Strain-rates of up to $\dot{\varepsilon} = 2500\ \mathrm{s}^{-1}$ have been achieved with this method [21].

The final technique considered as an intermediate strain-rate method is the drop weight or drop tower test. This is the most widely used method in this strain-rate regime and that is reflected in the relatively

large number of standards for testing. A search of "drop weight" in the ASTM standards and engineering digital library, restricted to active standards of test methods for mechanical tests, returns 90 results. This is partly due to its wide adaptation as a quality control measurement method. One interesting use of drop weight testing is outlined in ASTM standard E6890-90e1, "Standard Test Method for Drop Weight Impact Sensitivity of Solid-Phase Hazardous Materials," [22] which is used to measure the safety and stability of solid explosive ordnance. The basis of this technique is to use a falling weight to impact a sample. Very large masses can be used, up to 900 kN [21]. The strain-rate can be nearly constant by ensuring the energy of the driver is an order of magnitude greater than needed to deform the sample. Quantitative interpretation of results is difficult and may rely on unreasonable assumptions (such as assuming the weight is a rigid body). As a quality control measure an appropriate driver mass is used for the expected loading severity and only a certain percentage of samples are allowed to fail.

2.1.2. High Strain-Rates: $10^2 < \dot{\varepsilon} < 10^4 \text{ s}^{-1}$

The high strain-rate regime is of intense interest as this is a common range when a sharp increase in the rate sensitivity is observed. Figure 2.1 shows the classic result of Campbell and Ferguson [5] demonstrating the rate sensitivity of mild steel in various regions, from low to high temperature. These results were obtained with screw-driven and hydraulic cross head machines at low rates, drop weights at intermediate rates, and Split-Hopkinson Pressure Bar (SHBP) for high strain-rates (SHBP to be described). The dashed lines distinguish 3 regions where different behavior is observed. In region I, corresponding to low rate and/or moderate temperatures a small, constant slope is measured for the rate dependence. In region II a much higher rate dependence is observed for low temperatures and higher strain-rates for moderate temperatures. In this region thermally driven dislocation motion is

dominant and at low temperatures there is not enough thermal motion to overcome short range energy barriers, greatly increasing the flow stress. The limited strain-rate range at low temperatures is due to brittle failure at higher strain-rates. Region IV marks the emergence of the bilinear rate dependent behavior observed for many metals. This transition is largely due to the activation of additional microstructural mechanisms which are strongly coupled to the applied loading rate, e.g. dislocation drag.

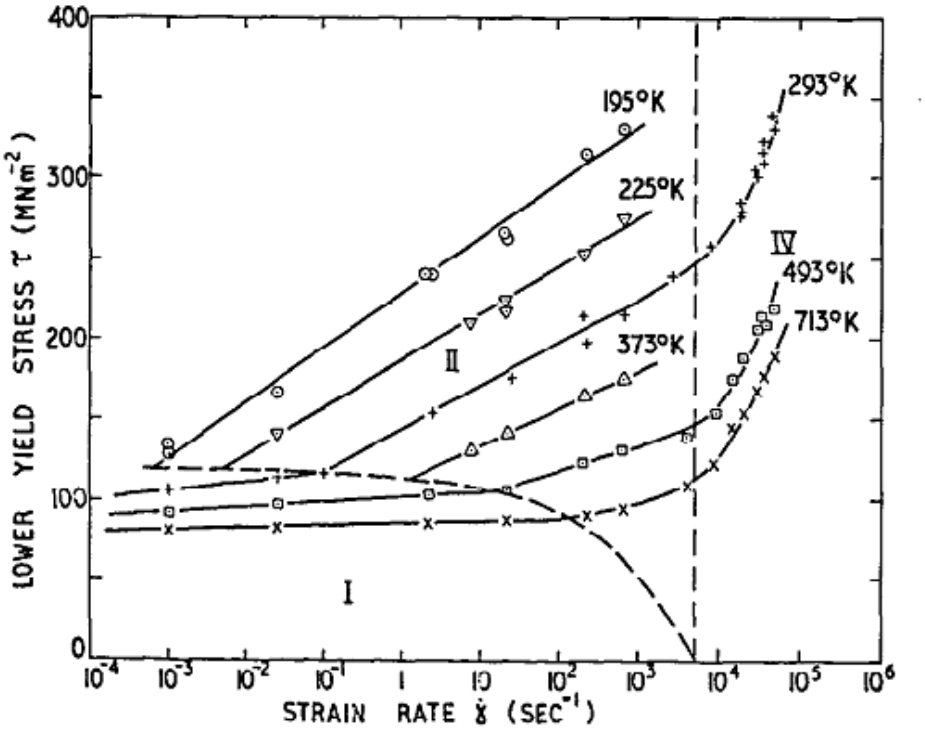

Figure 2.1: Flow stress versus logarithmic strain-rate for mild steel from low to high temperature [5].

One technique in this strain-rate regime was developed by G.I. Taylor, A.C. Whiffin, W.E. Carrington, and Marie L.V. Gayler at the Road Research Laboratory of the Department of Scientific and Industrial Research for the Experiments Department of the Ministry of Home Security, a wartime effort on understanding the strength and performance of various materials under conditions of high strain-rate from impact and penetration [23–26]. In Taylor impact a cylindrical rod is fired at high velocity into a

rigid target. The before and after states are compared against one another to determine the flow stress by:

$$\sigma = \frac{\rho V^2 (L - X)}{2(L - L_1)\ln(L/X)} \tag{5}$$

where σ is the flow stress, ρ is the density, V is the rod velocity at impact, L is the initial rod length, X is the length of the undeformed section after impact, and L_1 is the length of the deformed section. Figure 2.2 shows a schematic of the rod before and after impact, as presented by Taylor [24]. This analysis assumes one dimensional rigid-plastic analysis and requires accurate identification of the transition from undeformed to deformed, which for most materials will not be abrupt.

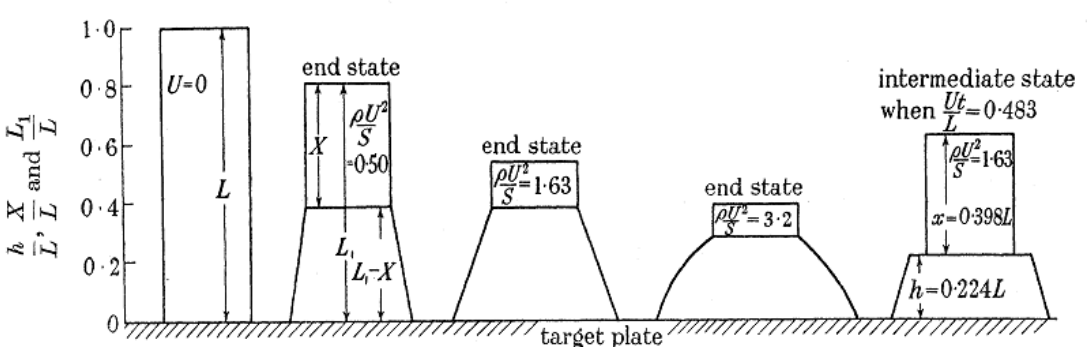

Figure 2.2: Schematic of Taylor rod before (left) and after (right) impact [24].

Despite its simplicity, the Taylor impact test was not widely adopted due to the difficulties of making accurate measurement of the deformed sample. Wilkins and Guinan at Lawrence Livermore National Laboratory used computer simulations of an elastic-plastic rod impact and developed a scaling law which agreed well with experiments [27]. Further improvements have been made, such as symmetric impact tests proposed by Erlich et al. [28], who used high speed photography to measure the time resolved deformation of two rods impacting. This greatly improved the quality of data for comparison to simulation, since intermediate states of deformation were now captured. By impacting rods with

one another the target boundary conditions (typically rigid plate) were eliminated, along with its uncertainties (e.g. friction or sliding during contact, or the deformation of the target itself). Taylor's impact test is now widely used for verifying constitutive relations, as it "exercises" the model by having a large range of pressures and strain-rates, and is inhomogeneous deformation.

Taylor impact and symmetric Taylor impact are used to study the high strain-rate compression of materials (tensile stress are generated upon reflection and interaction, but they are not the focus of the Taylor impact technique). To study high strain-rate tension other techniques are required, since at high loading rates a typical tension experiment sample would not undergo homogeneous loading. One technique of producing uniform tension is by pressurizing thin walled pressure vessels, which will experience pure tensile hoop stresses away from the cylinder caps. This is the basis for the expanding ring technique, in which a large pressure is suddenly applied to the inside wall of a thin ring. This was originally proposed by Johnson et al. [29], who used rings of stainless steel, aluminum alloys, and titanium alloys loaded with an explosive core. A sufficiently thin ring ensures uniform stress through the radial thickness. Upon experiencing the detonation wave the ring quickly expands. Real time measurement of the radial displacement during deceleration of the ring, via e.g. optical interferometer, provides all the data needed for determining the stress, strain, and strain-rate from the experiment ($\sigma = \rho r\ddot{r}\,; \varepsilon = \ln r/r_0\,; \dot{\varepsilon} = \dot{r}/r$). One setback of this experiment is evident in the expression for the strain-rate; unless the expansion and deceleration of the ring is constant, the strain-rate varies over the duration of the experiment. Many tests are needed to obtain stress-strain behavior at a specific strain-rate. They are also preloaded by large compressive stresses due to the loading technique. The compressive preload may involve permanent deformation, which is known to affect the material response.

By far the most common technique in this strain-rate regime is originally due to Hopkinson [30, 31], with advancements and refinements due to Davies [32], and Kolsky [33] and is shown in Figure 2.3. This technique is known as the split-Hopkinson pressure bar (SHPB) or Kolsky bar experiment, as Kolsky introduced the split incident/output bar arrangement (Kolsky bar can also refer to compression, tension, torsion, or a combination thereof, whereas SHPB is compression only [3]). For compression testing a striker bar is accelerated, typically pneumatically, to a velocity of the order $\sim 10^{+}$ m/s. The striker bar impacts the incident bar, generating a compressive stress wave which travels through the incident bar towards the sample and is measured by a strain gauge mounted on the incident bar. Upon reaching the sample the incident stress wave is transmitted and reflected. The transmitted wave is measured by the output bar strain gauge, and the reflected wave is measured by the same strain gauge on the incident bar. Care must be taken so that the incident compressive pulse and reflected tensile pulse do not overlap on the incident bar strain gauge, which limits the maximum length of the striker back (striker bar of length L will produce a pulse of duration $\tau = 2L/c_B$, where c_B is the bar wave speed of the striker/incident bar and is the characteristic 1D stress elastic wave speed). The incident, transmitted, and reflected strain histories of the elastic bars is combined to determine the stress, strain-rate, and strain of the sample. The sample must be short enough that the applied pulse duration is longer than the sample transit time, i.e. $\tau > l_0/c_{sB}$, c_{sB} is the sample wave speed, l_0 is the initial sample length, allowing the assumption of uniform stress. Friction must also be minimized at the sample-elastic bar interfaces since these will greatly affect the stress state. Dispersion of the waves due to the bar geometry, as well as inertial effects from the sample place further restrictions of the sample size. All of these effects have been rigorously studied and an entire section of the *ASM Handbook, Volume 8, Mechanical Testing and Evaluation, High Strain Rate Testing, Classic Split-*

Hopkinson Pressure Bar Testing has been written by George T. (Rusty) Gray III of LANL to address such issues and what limitations they imply on the sample geometry [34]. K. T. Ramesh [3] also provides an excellent overview of SHPB and its modifications in the *Springer Handbook of Experimental Solid Mechanics*. SHPB is now routinely performed in compression, tension, and torsion on a wide variety of materials including soft materials and ceramics, and miniaturized systems have been built allowing strain-rates 5x higher than conventional Kolsky bar systems (miniaturization is necessary to get around inertial strain-rate limiting effects).

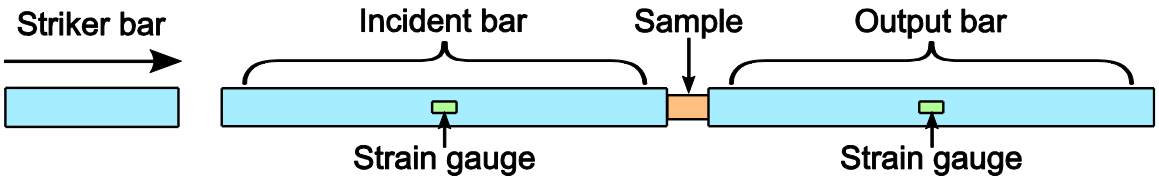

Figure 2.3: Schematic of SHPB/Kolsky bar experiment. Sample is sandwiched between two elastic sensor bars with strain gauges mounted on them. A striker bar is fired towards and impacts the incident bar, exciting a compressive stress wave. The wave travels through the incident bar and is measured by the incident bar strain gauge. When the stress wave reaches the sample a portion is transmitted through the sample, while the rest of the stress wave is reflected in tension. The output bar measures the transmitted wave. Combination of the strain histories allows determination of the stress, strain, and strain-rate in the sample.

2.1.3. Very High and Ultra-High Strain-Rates: $\dot{\varepsilon} > 10^4\ \mathrm{s}^{-1}$

The very high and ultra-high strain-rate regimes widely make use of the same techniques but with slight variations for achieving the desired strain-rate and investigating a specific phenomenon. Those phenomena include high strain-rate properties (e.g. flow stress), wave propagation, and failure processes. With a rich suite of diagnostics it is usually possible to extract data and features relevant to several phenomena. This becomes increasingly important as the maximum strain-rate and pressure are increased due to the limited facilities which can accomplish such loading, and the cost associated with sample preparation and experimentation. As mentioned earlier, in this strain-rate regime there is a transition from uniaxial stress to uniaxial strain. In the very center of the loading the material only sees

uniform displacements in all directions. The material within the stress wave experiences no lateral boundary conditions, thus no lateral strains. The velocity of a plastic wave, V_p, is determined by: $V_p = \sqrt{(d\sigma/d\varepsilon)/\rho}$, where $d\sigma/d\varepsilon$ is the slope of the plastic region and ρ is the density. In a typical tension experiment where the sample is experiencing uniaxial stress the slope in the plastic region is decreasing, even with strain hardening. Under conditions of uniaxial strain, especially at very high pressures, it may no longer be the case that the plastic wave speed is slower than the elastic wave speed. This behavior is nonlinear in general, allowing momentum diffusion throughout the wave. If the plastic wave speed is higher than the elastic wave speed the wave front will steepen up, forming a shock. These shocked states give invaluable information on the material behavior. Shocking a material to different pressure levels allows the determination of the equation of state over very broad conditions and represents some of the most researched information in high pressure, high strain-rate material testing. Three common methods are employed in this regime for loading: gas/powder launcher-driven, explosively-driven, or radiation-driven.

For all three loading scenarios a common experiment to be performed is the plate-impact or flyer-plate experiments [35–38]. During plate impact a flyer-plate is accelerated into a stationary target. Figure 2.4 shows a schematic time-distance (t-x) diagram of a flyer plate impacting a target. Upon impact a compressive wave propagates into the flyer and target. In this case the flyer and target are of the same material and the waves have the same characteristics (this is called a symmetric impact experiment). For generality these characteristics are shown as curved, which will be the case in very strong shock waves. For such waves the wave speed or shock velocity, U_s, may be a function of the particle velocity, u_p, e.g. a linear dependence is observed for many materials, $U_s = c_0 + Su_p$, where c_0 is the low amplitude bulk wave speed, and S is a material constant. When the compressive wave

reaches the free surface of the flyer or target it will be reflected into a tensile release wave, commonly called a rarefaction. Since the unloading does not follow the same thermodynamic path as loading, the release wave can form a rarefaction fan which spreads out as it propagates. If the two reflected tensile release waves intercept they will suddenly load the target in very high tension. Depending on the nature of the target material and the loading, the target may fail at the interface of intersection. Ductile failure evolves through void nucleation, growth, and coalescence. If a sufficiently large area fails in this manner the material will rupture and spall. This type of failure, known as spallation, is an intrinsic dynamic property of a material. Dynamic fracturing by spallation can also be achieved in brittle materials, which may begin with micro cracking and branching to form intergranular or transgranular fracture surfaces. These will also coalesce in the plane of the intersecting rarefaction waves and form a planar spallation fracture. Brittle materials will typically continue to fail from multiple wave interactions, leading to complete fragmentation of the sample.

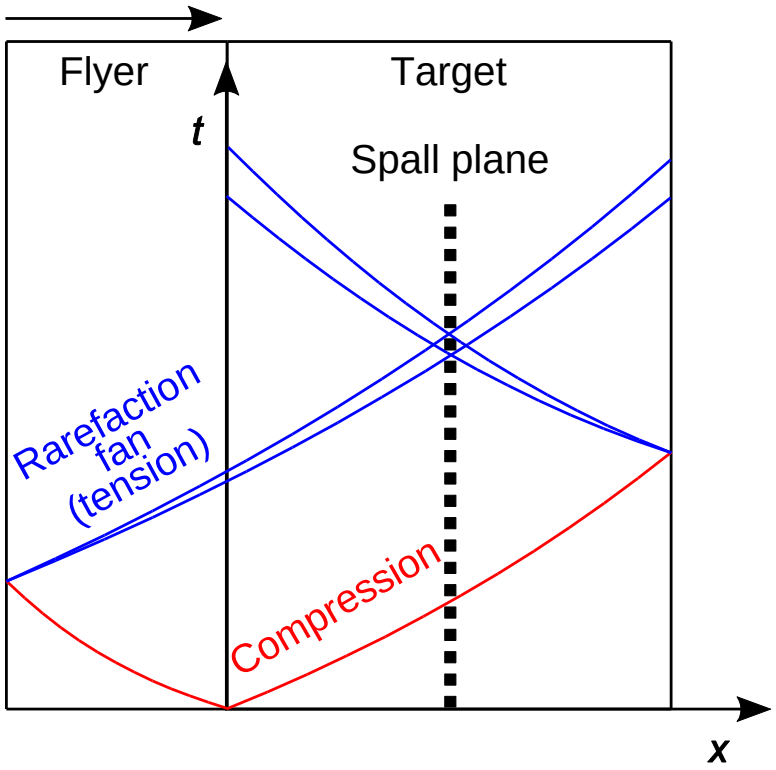

Figure 2.4: Time-distance (t-x) diagram from impact of a flyer onto a target of the same material (symmetric impact). The vertical axis is the time and the horizontal axis is the material coordinate. The impact creates a compressive wave which propagates away from the interface into both the flyer and target. Reflection at free surfaces creates tensile or release waves which spread out as a fan since the release is isentropic. The rarefaction fans can intercept within the target and superimpose, suddenly creating an area with very high tensile stress. In a ductile material this will drive void nucleation and nucleation. In brittle material transgranular fracture is commonly observed.

Flyer plate velocity is varied to achieve the desired peak stress. At lower desired strain-rates and peak stresses, gas guns project the flyer and are the subject of "low velocity" impact testing [39]. Flyer velocity ranges from ~ 10 m/s to ~ 1 km/s for these facilities. If higher velocities are required powder guns or multiple stage guns can be used. These systems achieve flyer plate velocities as high as 8 km/s [40], resulting in pressure in the target of ~ 800 GPa [41]. Electromagnetic acceleration of flyers by railguns can achieve velocities of 15 km/s and pressures of ~ 2000 GPa [41]. Use of explosives can also propel a flyer plate into a target (or directly load the target). These systems offer the main advantage that very large samples compared to gun systems can be used (flyer mass limited to ~ 1 g

for the highest velocities [3]). Experiments can also be performed with multiple samples being loaded simultaneously, and flyer velocities of $6\ \mathrm{km/s}$ and pressures of $\sim 500\ \mathrm{GPa}$ can be achieved [40]. Compared to gun facilities, though, the control of flyer velocity and impact planarity is poor. Higher flyer velocities and pressures for large samples are only achievable by the sudden expenditure of lots of energy achieved through nuclear explosions. As early as 1977 Ragan et al. reported on the shock compression of molybdenum via a nuclear explosion in open literature [42], attaining pressures of $2\ \mathrm{TPa}$, while the first record in the Russian literature was Al'tshuler et al. achieving $3.4\ \mathrm{TPa}$ in steel in 1968 [43] . Ragan published several more papers in the early 1980's and reported shock pressures up to $7\ \mathrm{TPa}$ in a variety of metals [44–46]. R.F Trunin documents Soviet research efforts in this field in several papers, with pressures of $10-20\ \mathrm{TPa}$ being investigated in the 1970's and 1980's, and reported in the 1990's [47, 48]. In general most of these experiments were carried out under the highest classifications and little has been made publically available.

2.2. Short Pulse Lasers for High Strain-Rate Testing

An alternative radiation-driven loading mechanism is provided by very intense light produced from short pulse lasers. Lasers are devices for amplifying light and possess very desirable features from a science and engineering perspective. Laser is an acronym standing for light amplification by stimulated emission of radiation. The theoretical basis was established in 1917 by Albert Einstein's [49] quantum theory of radiation, which proposed that stimulated absorption, spontaneous emission, and stimulated emission were necessary for equilibrium between matter and radiation. Stimulated absorption is the energy promotion of an atom by absorbing radiation with the same energy as the difference between the ground and excited state. In this excited state the atom may spontaneously emit a photon of energy corresponding to the difference between the energy states. Stimulated emission occurs when an atom

is already in the excited state and a photon with energy corresponding to the difference of the ground and excited state interacts with the atom, stimulating the transition from the higher energy state to the ground state. The result of stimulated emission is two photons with the same energy, direction, phase, and polarization [50]. This allows the light intensity to be amplified. Successful production of laser light requires that the number of atoms in the excited state must be greater than those which are reverting to the ground state from either spontaneous or stimulated emission, a condition termed population inversion. The produced light also has the very useful characteristic of being highly monochromatic, allowing coherence (the interference of the light is meaningful, e.g. the phase difference can correspond to a physical quantity of interest). Laser development succeeded that of the maser (microwave amplification by stimulated emission of radiation), developed by Charles Townes et al. in 1954 at Columbia university [51, 52]. After development and realization of the maser, Townes and Schawlow proposed the extension of techniques applied to the maser to the infrared and optical wavelength regime [53]. The first laser was built by Theodore Maiman at Hughes Research Laboratories [54] and was a ruby pulsed laser with a wavelength of 694.3 nm. Charles Townes was awarded the Nobel Prize in physics in 1964 for his contribution to the production of coherent radiation.

Lasers are broadly separated into two categories: continuous wave lasers (CW), and pulsed lasers. Continuous wave lasers are characterized by outputting light that has steady power, whereas pulsed lasers generate short pulses of light with high albeit temporary power. To produce the intense light necessary for high strain-rate material testing pulsed lasers must be used. Short pulses of laser light are produced by several methods, with modern laser systems possibly using a combination of these methods to produce the desired light pulse. In normal pulse operation typically a solid state medium,

possibly doped, is pumped by a flash lamp. The intensity and duration of the flash lamp influences the pulse characteristics and typically generates pulse durations from $100\ \mu\text{sec}$ to several milliseconds [55]. An alternative method exists which allows the production of much shorter pulses, as short as $1\ \text{ns}$. These lasers are Q-switched (also called Q-spoiled or giant pulse), the Q referring to a quality of the laser cavity which describes its ability to store energy. A high Q value means the cavity stores energy efficiently and only emits a small portion, allowing it to maintain population inversion and lasing. This is how CW lasers operate, with one cavity mirror reflecting nearly all light, and a partial mirror for the other cavity mirror which allows a small amount of light to escape. A low Q value indicates that energy is quickly lost in the cavity. In Q-switched lasers the Q value of the laser cavity is initially very high, with little to no light output. During this time the cavity is pumped, storing the pump energy. The Q value is suddenly decreased and the stored energy is rapidly lost, resulting in a very intense, short laser pulse. Techniques for Q-switching include rotating mirrors, electro-optic elements, acousto-optic elements, and bleachable dyes [55]. The first Q-switched laser was reported by McClung and Hellwarth in 1962 at Hughes Research Laboratories [56], who used a Kerr cell in a ruby laser to produce laser pulses with a $40\ \text{ns}$ rise time, $120\ \text{ns}$ duration, and peak power of $600\ \text{kW}$. Q-switched lasers with high peak power generally cannot produce pulses with shorter duration than $\sim 1\ \text{ns}$. To achieve shorter pulses other methods must be used. A common method, which can produce laser pulses in the picosecond range, is that of mode-locking. In mode-locked lasers active and passive optical elements modulate the laser light at the round trip cavity frequency [55]. This effectively transforms a single laser pulse of long duration (nanoseconds) to many pulses of very short duration (picoseconds), forming a pulse train. Then a single pulse within the pulse train is extracted (cavity dumped), typically by an electro-optic element. This single pulse may then be amplified to higher energy (peak energy produced may be limited to microjoules due to the working principles of optics required for mode-locking, e.g. satuarable absorbers).

Shortly after the first Q-switched laser was demonstrated there began to appear in the literature research into the mechanical effects resulting from laser absorption. In 1963 R. White reported on the generation of elastic waves from a pulsed ruby laser impinging the tip of an acoustic probe [57]. Using various coatings they demonstrated that the waves produced were not due to radiation pressure. Radiation pressure, P_{rad}, is given by: $P_{\text{rad}} = \frac{qI}{c}$, where I is the light intensity, c is the velocity of light in a vacuum, and q is a factor ranging from 1 for a perfect absorber to 2 for a perfect reflector. He observed that when the acoustic probe was coated with a higher absorbing material the response was a larger amplitude elastic wave, contrary to the expectation based on radiation pressure. In 1965 J. Ready irradiated tungsten targets in hydrogen atmosphere and measured the production of thermal electrons from the heated surface [58], finding that the laser heated the metal surface to several thousand K, with decent agreement between experimental and theoretical predictions. Later that same year Ready published a paper on the effects due to absorption of laser radiation [59] and presented an analytical model of the heat distribution within the material from a normal pulsed laser, in which any vaporized material is being removed fast enough that the width of the vaporized region is approximately constant. Also described is how the situation changes when a Q-switched pulse laser is used, which supplies energy so fast that a large volume may be vaporized, which creates a high pressure as the vapor recoils. Following these initial reports on the effects from high laser radiation, researchers applied short pulsed lasers to studies of electron emission [60], mass analysis [61], interactions with a solid bar [62], plasma formation [63], plasma expansion [64], shock induced in liquids [65, 66], and stress waves [67–71]. To increase the amplitude of stress generated from a given laser fluence various films and coatings have been investigated. Anderholm used a transparent quartz disk to impede the expansion of the vapor [71], O'Keefe and Skeen used transparent volatile materials [72] which reacted

during illumination, and Fox found that paint and water coatings efficiently augmented the laser-induced stress [73]. By the end of the 1970's pulse energies of tens of joules and durations as short as 300 ps were being produced with large lasers at the national labs. L. Vesser and J. Solem at Los Alamos National Laboratory (then Los Alamos Scientific Laboratory) produced $200\ \text{GPa}$ in thin films of aluminum [74], while Trainor et al. at Lawrence Livermore National Laboratory reported a peak stress of $1.8\ \text{TPa}$ [75].

Using Q-switching and mode-locking, tabletop lasers can produce pulses with energy of 10's J and durations as short as picoseconds. These pulses can have very high energy and power density (energy density is energy per unit area, unit J/cm^2; power density is peak power per unit area, unit W/cm^2). For example, a $300\ \text{mJ}$ laser pulse with a duration of $5\ \text{ns}$, focused to a spot size of $1\ \text{mm}$ in diameter has an energy density (often referred to as fluence) of: $0.3\ \text{J}\Big/\frac{\pi}{4}(1\ \text{mm})^2 \cong 38.2\ \frac{\text{J}}{\text{cm}^2}$, a peak power of $0.3\ \text{J}/5\times10^{-9}\ \text{s} = 60\times10^{6}\ \text{W}$, and a power density (often referred to as intensity) of $60\times10^{9}\ \text{W}\Big/\frac{\pi}{4}(1\ \text{mm})^2 \cong 7.4\times10^{9}\ \frac{\text{W}}{\text{cm}^2}$. At this laser fluence and intensity it is possible to generate pressures in the GPa range. The resulting pressure wave inherits the temporal nature of the incident laser pulse, resulting in stress waves with nanoseconds duration. The very sudden loading and unloading from short pulse lasers can result in strain-rates in excess of $10^{8}\ \text{s}^{-1}$. The highest energy and power lasers in the world can achieve pressures in the $100\ \text{TPa}$ range [76]. In this regard short pulsed lasers are unmatched for generating high pressures (at least terrestrially) and high strain-rates.

2.3. Laser Spallation of Bulk Materials and Interfaces

As pulse energy increased and pulse duration shortened with the development of new lasers, the induced mechanical waves were observed to permanently deform materials beyond the immediate vicinity of the ablation area [77]. In 1973 Fox and Barr reported on the effect of a $100-150\ \mathrm{J}$, $1\ \mathrm{ns}$ Nd:glass laser at $1.06\ \mu\mathrm{m}$ irradiating an aluminum target at a fluence of $>1000\ \mathrm{J/cm^2}$ [78]. In addition to the ablation spot on the front surface of the sample, where the laser impinged the target, they observed that the rear of the target had completely separated from the bulk of the sample, i.e. the first report of laser spallation. The observation was qualitative only since they lacked the diagnostics necessary to extract the quantitative information about the spallation process. Nevertheless, postmortem examination of the cross-sectioned sample reveals gross failure due to the large size, number, and density of voids in the spall plane. Eliezer et al. reported spallation of thin foils of copper and aluminum from laser-generated shocks in the 10's of GPa range, with a strain-rate of $\sim 10^7\ \mathrm{s^{-1}}$ [79]. In the article, written in 1990, they comment on the scarcity of laser spallation studies, which appeared to be mostly confined to internal studies at the national labs [80, 81]. Several other investigations followed theirs, mostly reporting on similar materials with different lasers (different energies, pulse widths, wavelengths) [82–90].

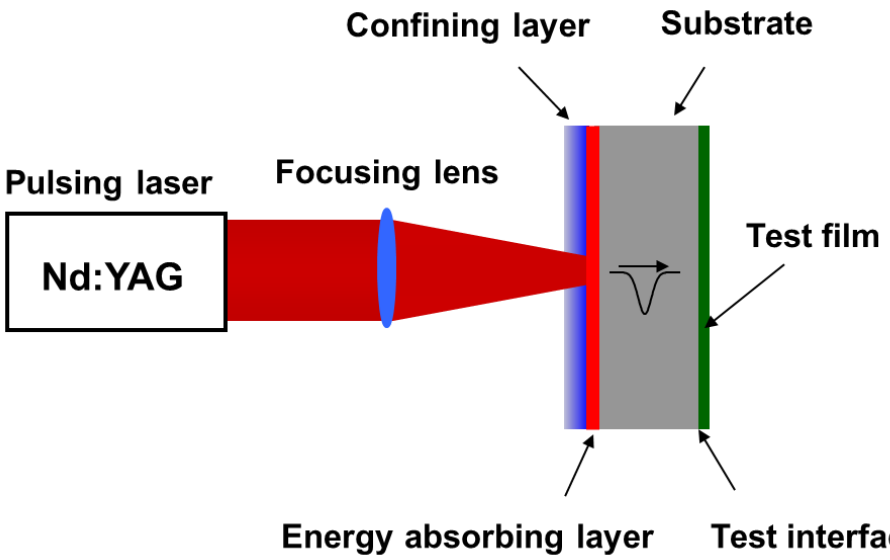

Figure 2.5: Schematic of typical laser-induced thin film adhesion measurement. Sample geometry consists of a film-substrate system whose strength is of interest, as well as an energy absorbing layer and transparent confining layer. Stress waves are generated by the focusing of short pulse laser light on the sample back surface, where the energy is absorbed.

Another area where stress waves generated from short pulse lasers find natural application is probing of interfacial properties, especially of thin films as illustrated in Figure 2.5. This is due to the laser-generated stress wave's transient nature, which allows a large temporal gradient at the interface between film and substrate. Many methods have been developed for measuring adhesion strength, such as the scratch test [91, 92], peel test [93, 94], pull test [95–97], and blister test [98, 99]. All of these tests suffer from shortcomings, such as not providing quantitative data or requiring elaborate sample preparation. A serious disadvantage is that of inducing significant inhomogeneous deformation in the film before the onset of delamination, which drastically alters the state of the interface and prevents measuring the intrinsic adhesion strength [100]. Measurement of interfacial strength by laser spallation was proposed by Stephens and Vossen [101, 102], who patterned small cuboids of metal onto a glass substrate. An absorbing coating is deposited onto the back of the glass substrate, which is illuminated by a short pulse laser. The laser-induced compressive stress propagates towards the film-substrate interface and reflects at the free surface, converting to a tensile wave. If the stress amplitude is

sufficiently high the metal is removed. Later investigations by Gupta et al. incorporated a thin aluminum film as an energy absorbing layer and a thin transparent coating of solid waterglass as a confining layer, as well as using an optical interferometer to measure the real time displacement of the film surface [103, 104]. Wang et al. further developed this technique by introducing rigorous analytical modeling and a shock wave loading mechanism through a fused silica pulse shaping material, thus significantly improving the loading efficiency for ultra-thin films [105, 106]. However, all the previous laser spallation work were limited to tensile model loading. In practical applications, materials, especially thin film interfaces, tend to fail under a much more complex stress state. By changing the planar substrate into a triangular prism and allowing the originally generated longitudinal wave to mode-convert into a shear wave, Wang et al. successfully extended laser spallation to mixed-mode [107, 108] and pure-shear loading [109]. The application of this technique has been extended from the adhesion of blanket thin films [102, 105, 108, 110–112], to patterned thin films [113, 114], and adhesion between biological cells and inorganic substrates [115, 116].

Chapter 3. Effect of Confinement and Pulse Duration in Laser Spallation

In laser spallation technique, the pulse duration, energy, and wavelength of the laser as well as the sample geometry can all influence the behavior of the material being investigated. A $1\,\mathrm{J}$ energy deposited in $1\,\mathrm{s}$ is very different from $1\,\mathrm{J}$ deposited in $1\,\mathrm{ns}$. Additionally, the sample geometry in the vicinity of the laser-matter interaction plays a crucial role in dictating the stress generation. The difference in acoustic impedance, $z = \rho c$, where ρ is the density and c is the wave speed, between a gas and a solid is very large. For example, the acoustic impedance of air at $20°\,\mathrm{C}$ and ambient pressure of $1\,\mathrm{atm}$ is $\sim 400\ \mathrm{N\cdot s\cdot m^{-3}}$, whereas for aluminum it is $\sim 14\times10^{6}\ \mathrm{N\cdot s\cdot m^{-3}}$. Pressure generated is proportional to the impedance mismatch, which is found by adding the reciprocal of each, then taking the inverse, i.e. $1/z_{\mathrm{tot}} = 1/z_{\mathrm{air}} + 1/z_{\mathrm{Al}}$ [117]. The mismatch between aluminum and air is:

$z_{\mathrm{tot}} = \left(z_{\mathrm{Al}} \cdot z_{\mathrm{air}}\right)/\left(z_{\mathrm{Al}} + z_{\mathrm{air}}\right) = \left(14\times10^{6}\cdot 400\right)/\left(14\times10^{6} + 400\right) \approx 400\ \mathrm{N\cdot s\cdot m^{-3}}$. Now compare that to the mismatch between aluminum and another solid which we assume has an impedance of $1\times10^{6}\ \mathrm{N\cdot s\cdot m^{-3}}$: $z_{\mathrm{tot}} = \left(z_{\mathrm{Al}} \cdot z_{\mathrm{solid}}\right)/\left(z_{\mathrm{Al}} + z_{\mathrm{solid}}\right) \approx 9.3\times10^{5}\ \mathrm{N\cdot s\cdot m^{-3}}$. The result is that energy deposited between materials with higher acoustic impedance results in higher pressure. This has made confinement a common practice for increasing stress generation.

Short pulse durations also play a critical role on stress generation. For a given energy content, as the pulse duration is shortened the peak power increases. Pressure has been found to scale with peak power for a wide range of pulsed lasers with different pulse durations, pulse energy, and wavelength [118], so shorter pulse lasers offer the potential advantage of generating higher stress. As the pulse duration is shortened, however, other mechanisms besides heating and expansion of the irradiated

material begin to become important. Since absorption of the laser energy is due to the behavior of the electrons, changes in electron behavior can affect stress generation. One particular effect that is important at short pulse durations is the electron-phonon coupling. The deposited laser energy is first absorbed by outer electrons, which transfer this energy into the bulk material through coupling with lattice vibrations. For ordinary materials at time scales as short as nanoseconds this process can be described with conventional heat conduction, treating the laser light as a heat flux. Even with melting and vaporization Fourier's law holds. The electron-phonon coupling has a characteristic time scale, and as the pulse is shortened and becomes comparable to the coupling time the system can be driven into non-equilibrium. Non-equilibrium is the result of the electrons being much more energetic than the lattice due to the limiting transfer rate. The characteristic time scale of the electron-phonon coupling is a few to 10's of picoseconds in metals [119]. As the pulse duration approaches this time scale the thermal conduction rate in the lattice is no longer the governing process and the non-equilibrium dynamics of the electron and phonon systems becomes dominant.

3.1. Stress Generation by Lasers

As laser light impinges onto a material outer electrons interact with the incoming radiation. The incident radiation is either absorbed, reflected, or transmitted. Metals are opaque to the visible and near IR wavelengths typical of pulsed lasers, so the laser light is reflected and absorbed. The absorbed light excites the outer electrons and, if given sufficient time, the outer electrons transfer their energy to the bulk of the material. The material heats up in response to the absorbed energy. The laser light is absorbed down to the skin depth, δ, given for metals by $\delta = \sqrt{2\rho/\omega\mu_0}$, where ρ is the resistivity, ω is the angular frequency of the laser light, and μ_0 is the permeability of free space (assuming the

relative permeability is ~ 1). For an Nd:YAG pulsed laser operating at the fundamental wavelength of $\lambda = 1064\ \text{nm}$ the angular frequency is given by $\omega = 1.77 \times 10^{15}\ \text{rad/s}$. The skin depth for Nd:YAG light illuminating an aluminum target of resistance $\rho = 28.2\ \text{n}\Omega \cdot \text{m}$ is given by:

$\delta = \sqrt{2\left(28.2 \times 10^{-9}\ \text{n}\Omega \cdot \text{m}\right) / \left(1.77 \times 10^{15}\ \text{rad/s}\right) \cdot \left(1.2566 \times 10^{-6}\ \text{N} \cdot \text{A}^{-2}\right)} = 5.15\ \text{nm}$. The majority of the deposited energy is being absorbed in a very small volume proportional to the spot size multiplied by the skin depth, a volume of a fraction of a nanoliter. Even millijoules of energy deposited into such a small volume is capable of heating any element well past its melting or boiling temperature. While the material is heating up, though, the energy is being diffused away from the absorption volume by heat conduction. The characteristic thermal diffusion depth is given by $l_{\text{th}} = 2\sqrt{\alpha \tau}$, where α is the thermal diffusivity, and τ is the pulse duration. Again assuming an aluminum target with diffusivity of $\alpha = 8.4 \times 10^{-5}\ \text{m}^2 \cdot \text{s}^{-1}$ and a pulse width of $\tau = 5\ \text{ns}$, the diffusion length will be $l_{\text{th}} = 2\sqrt{\left(8.4 \times 10^{-5}\ \text{m}^2 \cdot \text{s}^{-1}\right) \cdot \left(5 \times 10^{-9}\ \text{s}\right)} = 1.3\ \mu\text{m}$. To heat a volume of aluminum corresponding to the spot size area and thermal diffusion depth to $6000\ \text{K}$ would require approximately $12\ \text{mJ}$. The actual energy required to vaporize the target material is between these two extremes and the effective thermal diffusion depth, as well as the energy needed for vaporization, will be reduced accordingly [120].

Once the material begins to vaporize, which may only take a small fraction of the applied pulse duration, the process of ionization will begin. Absorption of laser light by the incipient plasma proceeds via classical or collisional absorption by a plasma, also referred to as inverse Bremsstrahlung absorption. Although it is known that this process is not truly responsible for absorption, and a number of important features are not accurately predicted, it is nonetheless qualitatively informative. In collisional absorption the free electrons in the nascent plasma are excited by the laser electric field.

They begin to oscillate in the electric field and collide with ions, transferring their energy. The collisions heat up the plasma, increasing the ionization, which will also increases the absorption. Quantitatively, inverse Bremsstrahlung predicts ionization many orders of magnitude lower than observed [121]. It is believed that other processes, such as multiphoton ionization, enable cascade processes which allow the plasma to rapidly ionize. Once a plasma forms the bulk material is effectively shielded due to the very high absorption of the plasma. This is termed plasma shielding, and is one of the factors which allows confinement to generate much higher stresses. Without confinement the plasma shielding effectively reduces the impulse coupling between the laser and the target. With confinement, even if the laser energy is not being directly deposited into the target, the now confined interaction volume continues to deliver energy into the target, augmenting stress generation.

3.2. Laser Spallation Experiment

Figure 3.1 shows a schematic of a typical laser spallation experiment to measure the interfacial strength of a thin film on a substrate. The sample consists of the substrate-film system whose properties are of interest, an energy absorbing layer, and a confining layer. The energy absorbing layer is a thin film of aluminum sputter deposited from a base pressure of 10^{-7} Pa at 150 W to a thickness of 400 nm. Undiluted waterglass is spin coated at 2000 RPM, resulting in a thickness of ~10 μm. Spin coated waterglass has the advantage over transparent materials that are nominally solid since it forms a very intimate bond with the energy absorbing layer, and reduces the need to precision plane, lap, and polish the back of the sample substrate and confining layer. When working with high powered lasers reflection of the laser light back into the laser optical system (back reflection) can cause serious damage

to the optical components. It is desirable for the back of the sample to be rough and diffusive. This can also enhance absorption of the light since the diffusive nature may scatter or reflect the laser light onto adjacent material.

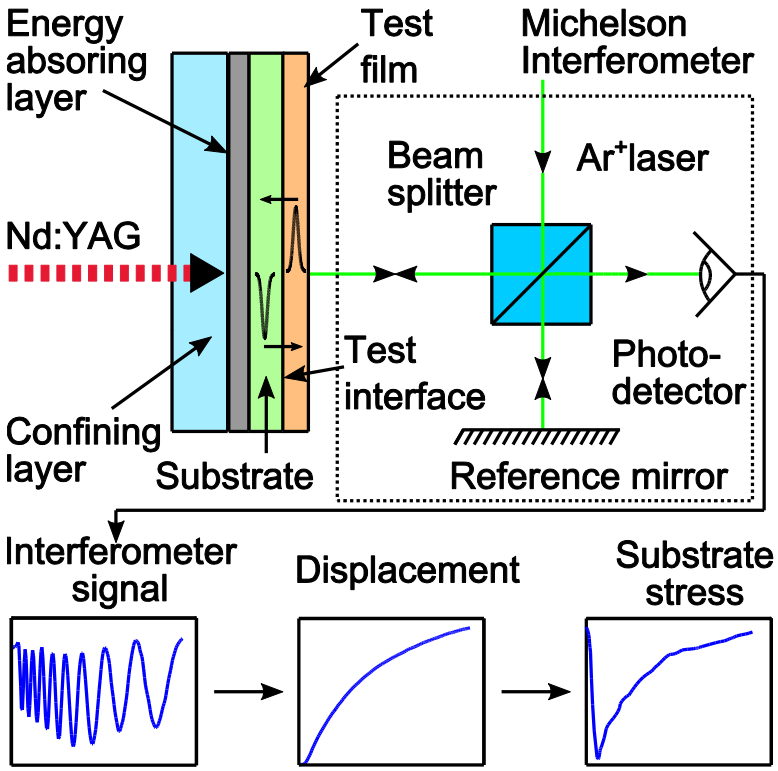

Figure 3.1: Schematic of laser spallation setup for thin film adhesion testing. Sample consists of a transparent confining layer, energy absorbing layer, substrate and film. Compressive stress is generated at the interface of the confining and energy absorbing layers by the rapid expansion of irradiated material. The stress travels through the substrate and film. Upon reflection at the film free surface the interface is loaded in tension. The surface displacement history is measured with a Michelson interferometer.

The sample is loaded by a short pulse Nd:YAG laser (Nd:YAG stands for neodymium doped yttrium aluminum garnet). Pulse durations range from 1–10's ns for Q-switched lasers to sub nanosecond for mode-locked lasers. Highest energy output is from the fundamental wavelength of 1064 nm. Our investigation utilized a Q-switched Nd:YAG laser with a 5 ns pulse width (New Wave Research Tempest 300), as measured by the full-width-half-maximum (FHWM), and a mode-locked, cavity dumped Nd:YAG laser with a pulse width of 50 ps FWHM (Continuum Leopard SS-2). The 5 ns

laser produces $300\ \mathrm{mJ}$ while the $50\ \mathrm{ps}$ produces $260\ \mathrm{mJ}$. The laser is focused from its nominal diameter to a spot size of $\sim 1\ \mathrm{mm}$ for most experiments. It is important that the spot size is no smaller than $\sim 1/3\times$ the sample thickness to ensure that the uniaxial plane wave travels the sample thickness without experiencing transverse relief. Geometric stress attenuation will also become significant at these distances. In practice the spot size is typically comparable or less than the sample thickness to mitigate factors such as intrinsic attenuation.

Upon absorption of the incident laser pulse, a compressive stress wave is generated and propagates away from the interaction volume. The wave travels towards the sample surface with the test film, as well as towards the surface of the confining layer at the back of the sample. The interface at the energy absorbing layer is destroyed during stress generation, which prevents the back surface reflected tensile wave from interacting with the wave propagating toward the test film (this generates the immediate unloading or release wave characteristic of loading from short pulse lasers). The wave traveling towards the test-film-substrate interface will reach the free surface and reflect into a tensile wave. The now tensile wave loads the interface in tension. If the amplitude of the tensile stress at the interface is sufficiently high the film will be spalled from the substrate. The adhesion strength is found by determining the threshold interfacial stress for film debonding.

Quantitative measurements of the spallation process are conducted with a Michelson interferometer. The Michelson interferometer is a path length difference interferometer in which the measureable phase difference of two coherent waves is proportional the difference in path length. A continuous, single-mode, argon ion laser operating at the standard $514.5\ \mathrm{nm}$ green line (Coherent Innova 90)

corresponding to the $4p\,^4D^o_{5/2} \rightarrow 4s\,^2P_{3/2}$ transition [122] of singly ionized argon was used for the Michelson interferometer (the $4p \rightarrow 4s$ transitions are favorable due to their long lifetime). Single-mode/single-frequency output is ensured by inserting an etalon between the plasma tube and the rear frequency selector prism-mirror assembly. The etalon suppresses the longitudinal modes associated with round trip frequency of the $1\ \mathrm{m}$ oscillator cavity, greatly reducing the spectral line width and ensuring a long coherence length. The argon light enters the interferometer, whose first optical element is a cubic beam splitter. Part of the light is transmitted through the beam splitter interface, and part of the light is reflected. The transmitted light goes to a stationary reference mirror and this distance designates the nominal balanced path in which the path length difference is zero. The reflected light is incident on the sample and forms the diagnostic leg of the interferometer. Careful alignment of the Nd:YAG loading laser spot and that of the reflected diagnostic beam ensure that any measured path difference is due to the laser-generated stress. To further ensure this, and to simplify data reduction and analysis, the argon light is focused to a small spot size of $\sim 50\ \mu\mathrm{m}$. The small spots size allows $1\mathrm{D}$ wave analysis relating the measured surface motion to the stress wave. After refection at the reference mirror and the sample surface the light returns to the beam splitter. The returning beams are steered to ensure they intercept and interfere (some degree of tilt is necessary to ensure no specular back reflections into the argon laser, which drastically alters the output power, can destroy coherence, and could damage the laser optics). The now interfered light is collected and its intensity is measured with a high speed GaAs biased photodetector (Electro Optic Technologies ET-4000A) with rise and fall times $< 40\ \mathrm{ps}$. The photodetector signal is recorded by a $5\ \mathrm{GHz}$ digital oscilloscope (LeCroy Wavemaster 8500) capable of sampling at $50\ \mathrm{ps/point}$.

The fringe intensity varies as the surface is displaced, and the intensity, $I(t)$, is related to the displacement by:

$$I(t) = \frac{I_{\max} + I_{\min}}{2} + \frac{I_{\max} - I_{\min}}{2} \sin\left(\frac{4\pi}{\lambda_{Ar^+}} u(t) + \phi \right) \tag{6}$$

where $I_{\max}$ and $I_{\min}$ are the maximum and minimum intensity for a given half fringe, λ_{Ar^+} is the wavelength of the argon-ion laser, $514.5\,\text{nm}$, ϕ is a phase factor that increments by π each half fringe, and $u(t)$ is the surface displacement. $(I_{\max} + I_{\min})/2$ is the mean fringe value, while $(I_{\max} - I_{\min})/2$ is the fringe amplitude. In reality $I_{\max}$ and $I_{\min}$ can shift each half fringe due to moving away from the point of maximum sensitivity, or surface motion causing less of the specularly reflected light to be collected by the photodetector. Once the displacement is determined, by proper accounting of $I_{\max}$ and $I_{\min}$ as well as the phase shift, the stress in the substrate can be calculated from 1D wave analysis (see Appendix A for derivation):

$$\sigma_{\text{sub}} = -\frac{1}{2}(\rho c_{\text{L}}) \cdot \frac{\partial u_{\text{fs}}}{\partial t} \tag{7}$$

where ρ is the substrate density, c_{L} is the substrate longitudinal wave speed, and $\partial u_{\text{fs}}/\partial t$ is the free surface velocity. The $-1/2$ factor arises due to the free surface having twice the velocity as the bulk (both incoming compression wave and reflected tension wave displace in the same direction, as required by the traction-free boundary condition of the free surface). The interfacial stress experienced between a film and substrate was extensively studied by Wang [105, 107, 108, 123], who derived a simple expression for the interface stress based on transmission and reflection at the substrate-film boundary, valid for thin films:

$$\sigma_{\text{int}} = -(\rho h)_{\text{film}} \frac{\partial^2 u_{\text{fs}}}{\partial t^2} \tag{8}$$

where ρ and h are the density and thickness of the film coating, and $\partial^2 u_{fs}/\partial t^2$ is the acceleration of the free surface.

3.3. Effect of Pulse Duration in Si

In addition to its predominant application for thin film interfaces, laser spallation can also serve as a powerful tool for probing high strain-rate behavior of bulk materials. In the absence of a surface coating, the technique has been used to characterize the bulk spallation strength of various materials [82–85, 112, 124, 125]. Due to the high pressure and short duration of the stress pulse, high strain-rate but low total strain is achieved which is advantageous since damage to the sample is minimal, and in the case of spallation the damage is localized. This allows for easy sample recovery and postmortem examination, even for brittle materials which may be completely destroyed by other techniques.

Previous theoretical model based on the thermoelastic expansion of the absorbing layer under nanoseconds laser pulse illumination predicts that the peak stress and strain-rate in laser spallation increase with decreasing pulse width of similar energy content, and that the pressure follows the same time evolution of the laser pulse [123]. A shorter stress pulse would also spall the material closer to the surface and allows the fully spalled area to be exposed and examined, rather than just the cross-section if spallation is deep in the sample. This is especially beneficial for brittle materials which may suffer additional damage during sectioning. Therefore it is generally viewed that a shorter laser pulse duration should be more effective in high strain-rate material testing due to the ability to produce a much higher stress and shorter duration of the stress wave pulse. However, due to the complex mechanisms involved in the photomechanical coupling for laser-induced stress waves such as

thermoelastic expansion, phase transformation, ionization, the generated stress profile may also depend on the time scale of the interaction, e.g. electron-phonon coupling, as the laser pulse shortens [59, 63, 64, 71, 74, 118, 119, 121, 126]. One objective of this study is to investigate the effect of the pulse duration on the laser-generated stress wave profile and to verify whether the previous prediction based on nanosecond laser absorption [123] can still hold as the duration of the applied laser pulse shortens from nanoseconds to a few tens of picoseconds (two orders of magnitude difference).

Spallation experiments were carried out using an experimental setup similar to that described in Figure 3.1. Since the diagnostics in laser spallation is obtained from the sample surface it is important to differentiate the characteristics arising from the stress generation, from those due to the wave interaction within the material (e.g. stress wave profile being influenced by plasticity). Based on this consideration, single crystal silicon was chosen to be the substrate due to its ability to maintain purely elastic behavior to high pressure and strain, even under shock loading [127]. As shown in Figure 3.2, components of the sample include a transparent waterglass confining layer, an Al energy absorbing layer, and Si substrate. The $500\ \mu\text{m}$ thick planar $\langle 100 \rangle$ single crystal Si wafers were magnetron sputter coated with a $400\ \text{nm}$ thick Al thin film energy absorbing layer, which were followed by spin coating of waterglass confining layer with a thickness of $10\ \mu\text{m}$. The quantities of most interest for comparison between the $50\ \text{ps}$ and $5\ \text{ns}$ laser are the peak stress generated, the profile of the stress history, and the strain-rate variation. While our experiment does not directly measure any deformation of the sample, it is possible to calculate the strain-rate in terms of material properties and the measured displacement by combining the balance of momentum:

$$\frac{\partial \sigma}{\partial X} = \rho \frac{\partial v}{\partial t} \tag{9}$$

with material conservation:

$$\frac{\partial \varepsilon}{\partial t} = \frac{\partial v}{\partial X} \tag{10}$$

resulting in:

$$\frac{\partial \varepsilon}{\partial t} = \rho \left(\frac{\partial \sigma}{\partial v} \right)^{-1} \frac{\partial v}{\partial t} \tag{11}$$

where X is the material coordinate, v is the particle velocity, and ε is the strain. Invoking the previously defined momentum conservation relating stress and material velocity, Equation 7, we arrive at the instantaneous strain-rate in terms of elastic wave speed and the free surface velocity:

$$\frac{\partial \varepsilon}{\partial t} = -\frac{1}{2c_L} \frac{\partial^2 u_{fs}}{\partial t^2} \tag{12}$$

The time averaged strain-rate is obtained by:

$$\left\langle \dot{\varepsilon}(t) \right\rangle = \frac{1}{\bar{\tau}_{\text{fall}}} \int_{t}^{t+\bar{\tau}_{\text{fall}}} \dot{\varepsilon}(\xi) d\xi \tag{13}$$

and is averaged over the mean fall time, $\bar{\tau}_{\text{fall}}$, for the pertinent loading condition. The reason for introducing the time averaged strain-rate is due to the variation of the strain-rate across the tensile relief wave after reflection.

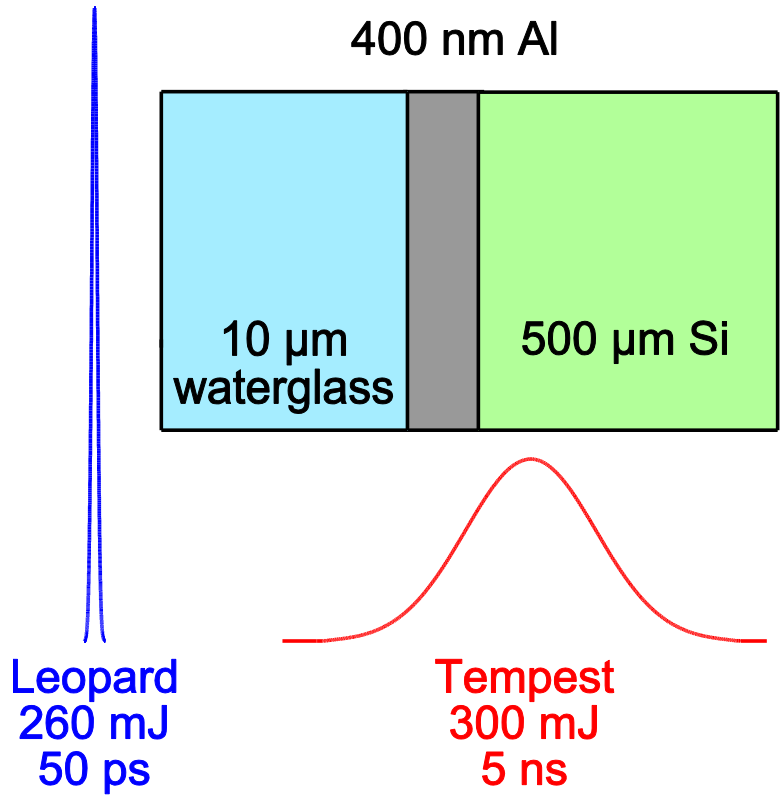

Figure 3.2: Schematic of laser spallation sample geometry. 500 µm Si is sequentially coated with a 400 nm thin film of aluminum as an energy absorbing layer, followed by a 10 µm spin coated waterglass confining layer. 50 ps or 5 ns laser pulse provided by an Nd:YAG laser with energy up to 300 mJ is deposited onto the energy absorbing layer, leading to the generation of a compressive stress pulse which propagate towards the substrate free surface. Upon reflection at the free surface the substrate is loaded in tension.

Figure 3.3(a) shows a plot of a typical fringe record measured from spallation of Si at high energy. Time zero corresponds to the beginning of surface motion, and we can see that the initial fringes are of subnanosecond wavelength. Figure 3.3(b) shows the displacement profile resulting from the interferometer record. Over the duration of $10\ \text{ns}$ the substrate has been displaced $\sim 3\ \mu\text{m}$, but achieves nearly $500\ \text{nm}$ in $1\ \text{ns}$. This corresponds to peak substrate velocity of $\sim 800\ \text{m/s}$, which is attained in less than $1\ \text{ns}$, an acceleration of $>15\times10^{9}\ \text{g's}$. This prodigious acceleration is due to a peak stress of $>7\ \text{GPa}$ being realized in the Si.

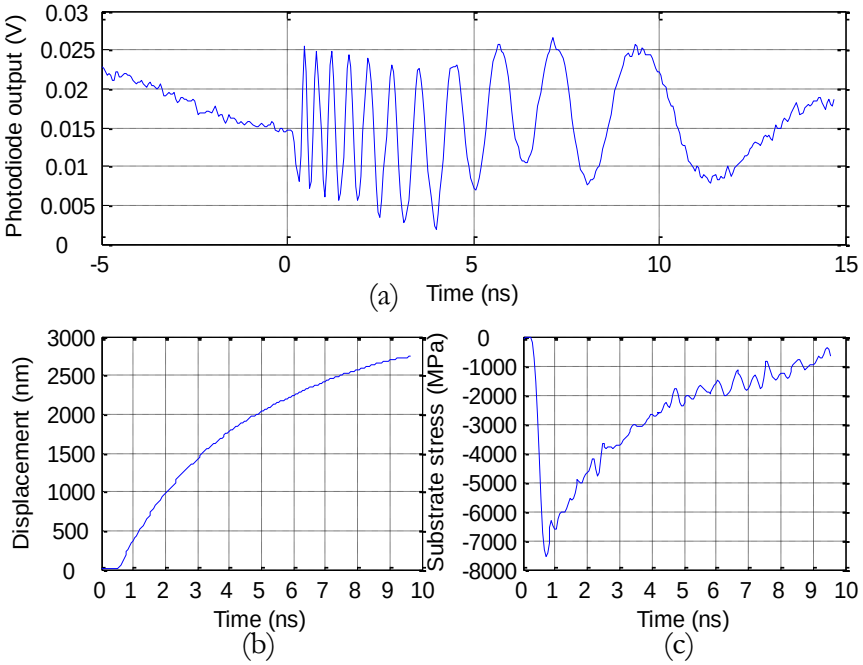

Figure 3.3: Typical data from loading of Si wafer at high energy: (a) the raw interferometer signal, (b) the displacement, and (c) the stress history derived from the displacement.

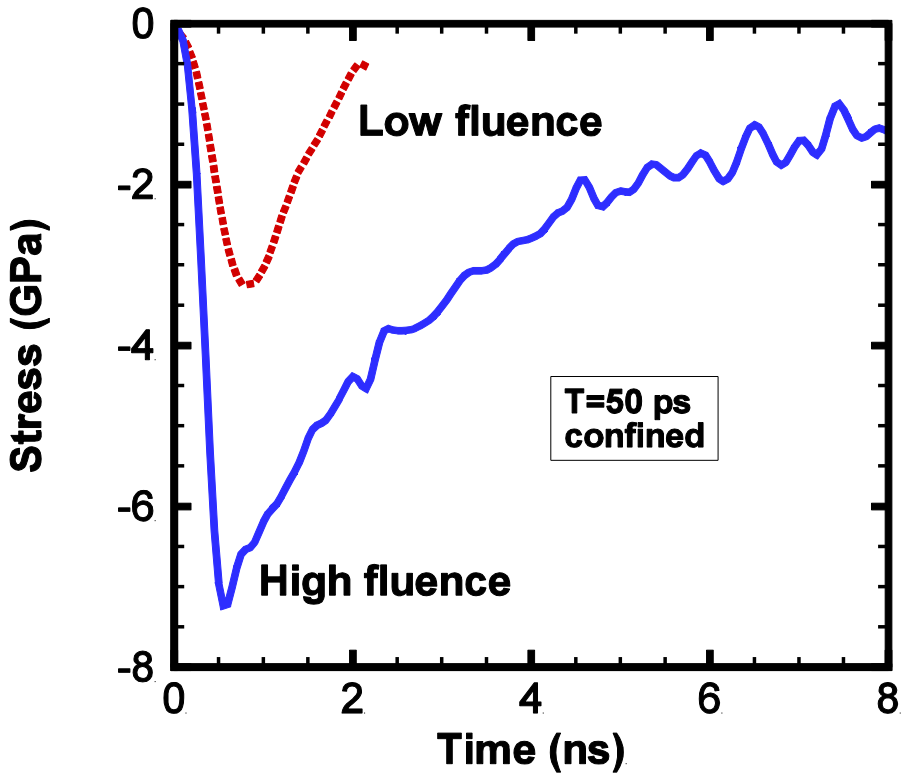

Figure 3.4: Stress history for 50 ps loading at low fluence of 6.4 J/cm² and high fluence of 33 J/cm² under confined conditions. At low fluence the stress profile is similar to the input laser profile, while the high fluence stress profile exhibits very rapid loading, with stretched unloading.

Figure 3.4 shows the stress profiles for low ($6.4\ J/cm^2$) and high ($33\ J/cm^2$) fluence loading of silicon with the $50\ ps$ laser. At low fluence the peak stress recorded was $3\ GPa$, with a rise time of $0.5\ ns$, and a fall time of $1\ ns$ (rise time is the time from 10%-90% signal maximum; fall time is the opposite). At high fluence peak stresses of $9\ GPa$ were measured, with similar rise time, but the unloading was stretched to $6.6\ ns$. For comparison Figure 3.5 shows the measured stress history from the $5\ ns$ laser at the same low and high fluence values. The low fluence peak stress only reached $2\ GPa$, and the temporal profile was a faithful copy of the input Gaussian laser pulse. As the fluence is increased a dramatic transition is observed in the stress profile. The profile is no longer Gaussian,

instead showing a very fast rise time of ~1 ns, and stretched unloading with a mean fall time of 6.6 ns.

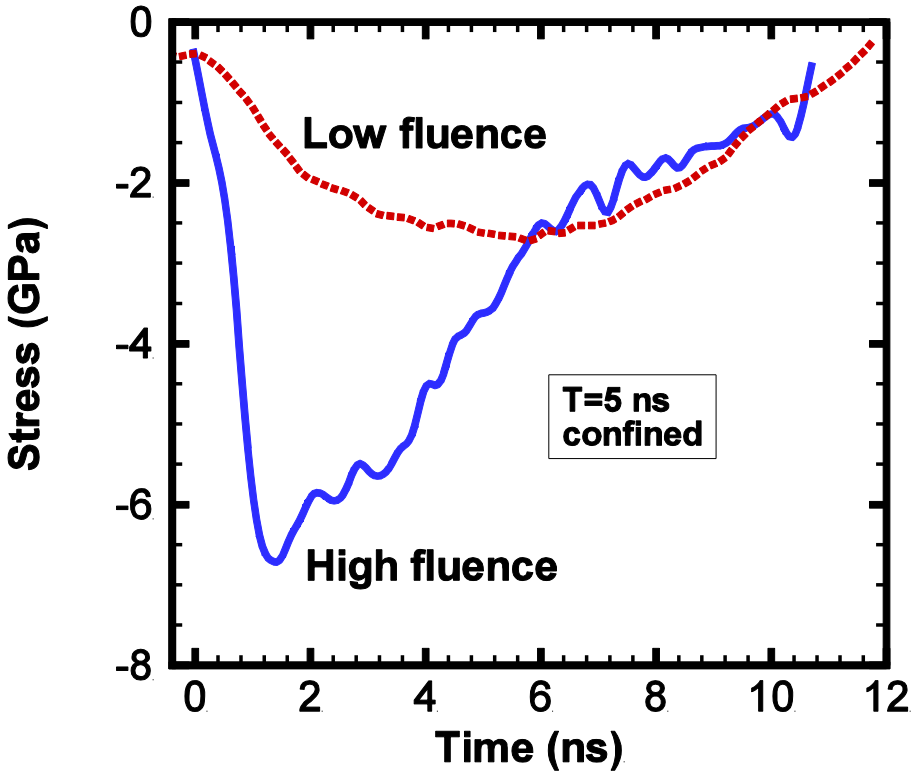

Figure 3.5: Stress history measured from the 5 ns laser at low fluence of 6.4 J/cm² and high fluence of 33 J/cm² under confined conditions. At low fluence the stress profile is a faithful copy of the input laser profile, while the high fluence stress profile exhibits similar rapid loading with stretched unloading as observed with the 50 ps laser.

3.4. Effect of Confinement in Si

In addition to the laser pulse duration, another parameter which can influence the laser-generated stress wave is the confining layer. In order to increase the amplitude of the laser-generated stress wave, it has been a common practice to confine the interaction volume with a liquid or solid layer transparent to the laser light, increasing the laser impulse coupling by preventing the free expansion of the

irradiated material [71–73, 117, 128]. Without confinement, the free expansion of the laser-generated plasma generates a stress pulse of similar temporal profile as the laser. With confinement, energy relaxation through expansion is inhibited, forcing other, possibly slower relaxation channels, such as heat conduction into the confining layer, to contribute. Since the energy relaxation mechanisms under confinement might depend on time scale of the laser pulse duration, it is important to understand how the confining layer influences the stress profile for laser pulses with picosecond duration from those of nanosecond duration, allowing differentiation of the confining layer influence from novel material behavior.

The sample geometry is the same as that used for the pulse duration study, as shown in Figure 3.2, but the spin coated waterglass confining layer is omitted for the unconfined sample. Additionally, only the 50 ps laser was used in this study as the 5 ns laser could not produce stress waves of sufficient amplitude for reliable and are repeatable detection without confinement.

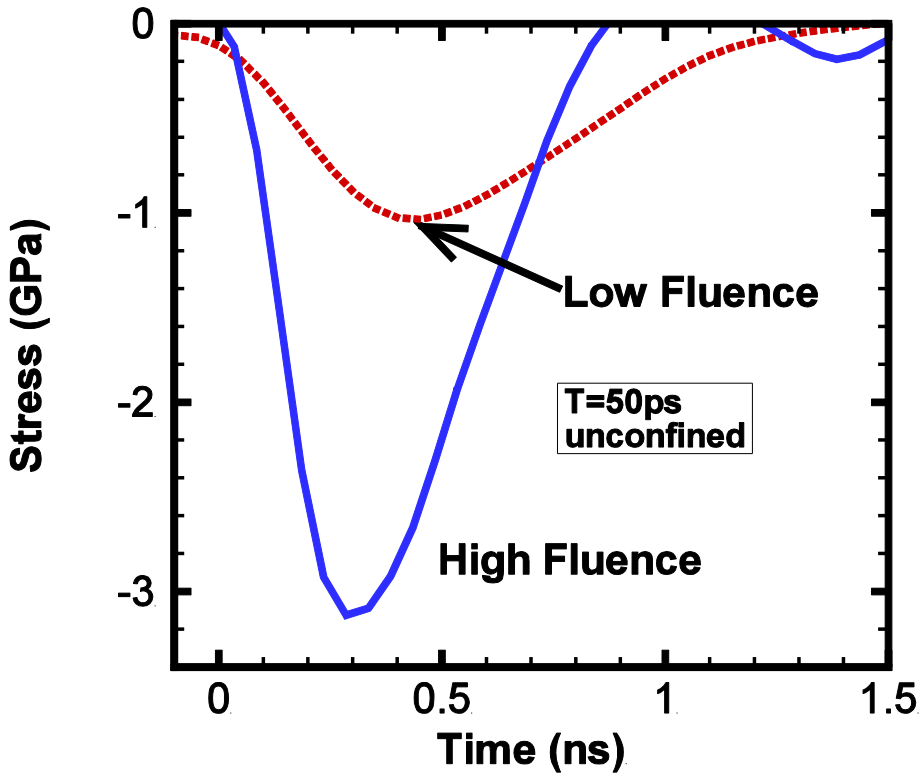

Figure 3.6: Stress profiles from the 50 ps laser without confinement. At low fluence a 1 GPa stress wave is observed whose profile is similar that that of the laser. Under high fluence conditions 3 GPa stress is produced which also has a temporal profile similar to the input laser.

Figure 3.6 shows the stress histories observed without confinement. At both low and high fluence the stress profile is now observed to be slightly asymmetric Gaussian with 0.5 ns rise times and 1 ns fall times. Peak stresses were 1 GPa and 3 GPa for low and high fluence, respectively. Comparing with the confined testing results a stress enhancement of ~ 3× is observed. At low fluence under confined and unconfined conditions the resulting stress profile is Gaussian, but at high fluence the stress profile is only Gaussian when the absorbing layer in unconfined.

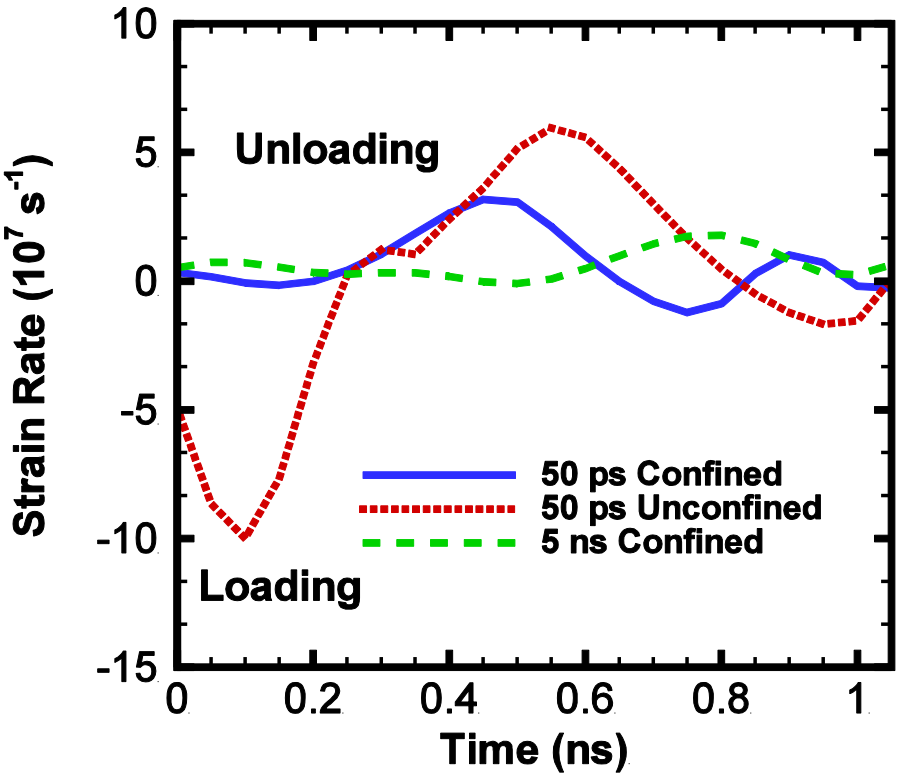

Figure 3.7: Comparison of the time averaged strain-rate for the high fluence stress histories shown in Figures 3.4, 3.5 & 3.6. The 50 ps data is averaged over the mean fall time of 1.2 ns, while the 50 ps and 5 ns confined data was averaged over the mean fall time of 6.6 ns. The 50 ps and 5 ns have similar strain-rate profiles in the relevant unloading (tension) regime, with peak strain-rate approaching 4×10^7 s^{-1}. The 50 ps unconfined strain-rate has a peak strain-rate of 7×10^7 s^{-1}.

Figure 3.7 is a comparison of the time averaged strain-rates for the high fluence stress profiles shown in Figure 3.4, Figure 3.5, and Figure 3.6. Initially the strain-rate is negative while the sample is being compressed, but this strain-rate is not very meaningful since we are averaging over the mean fall time of the stress histories. The 50 ps and 5 ns confined strain-rate profiles are very similar during unloading, with a slight difference of time due to the rise time of the 50 ps stress profile being quicker than the 5 ns. Both reach a peak strain-rate of $\sim 4\times10^7$ s^{-1} in tension. The 50 ps laser loading the unconfined sample is able to reach a peak time averaged strain-rate of $\sim 7\times10^7$ s^{-1}, nearly double that of the confined samples. For all samples the instantaneous strain-rate is an order of magnitude higher.

Figure 3.8 shows SEM images of the spallation planes produced by the 5 ns (a) and 50 ps (b) lasers at high fluence with the confining layer. For both lasers the most prominent feature of the spall surface is the fracturing along the {111} planes. The {111} planes were identified by tilting the sample such that one of the planar faces was being imaged head-on, Figure 3.8 (c) & (d). The angle between opposing faces was measured to be 109°, closely matching the actual angle of ~109.5° and within the margin of error for alignment and measurement. The spallation from the 50 ps laser produced a much more uniform spall plane, with a smaller variation in the height of the fracture surface. The spall surface is also closer to the sample surface. The uniformity and reduced variation from the 50 ps laser indicates that the post shock tension loading from the 50 ps laser is more uniform and quicker, as seen in the unloading portion of the stress profiles of Figure 3.4 and Figure 3.5.

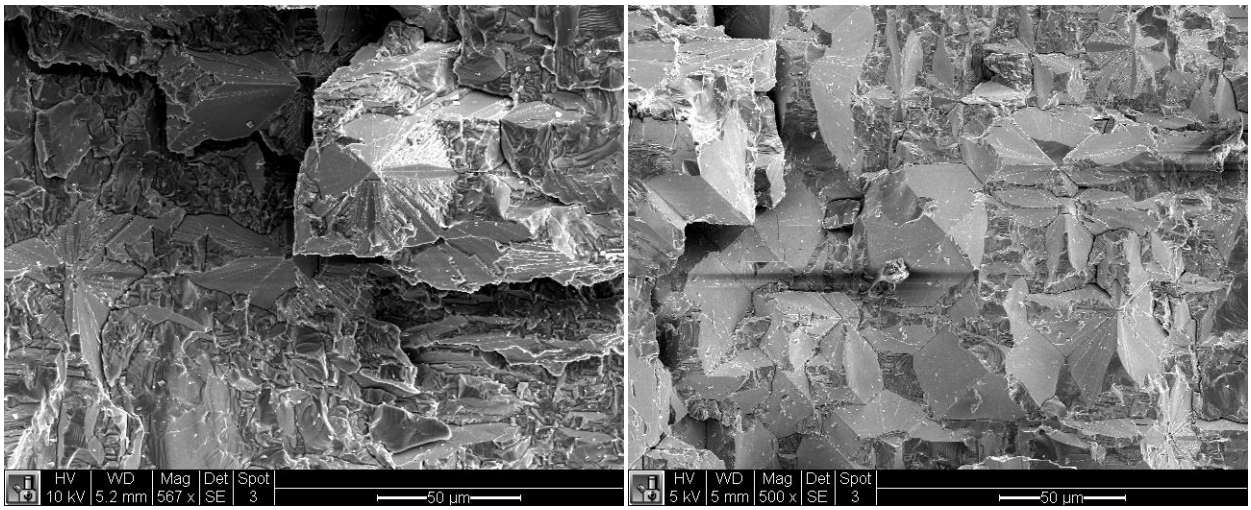

(a) (b)

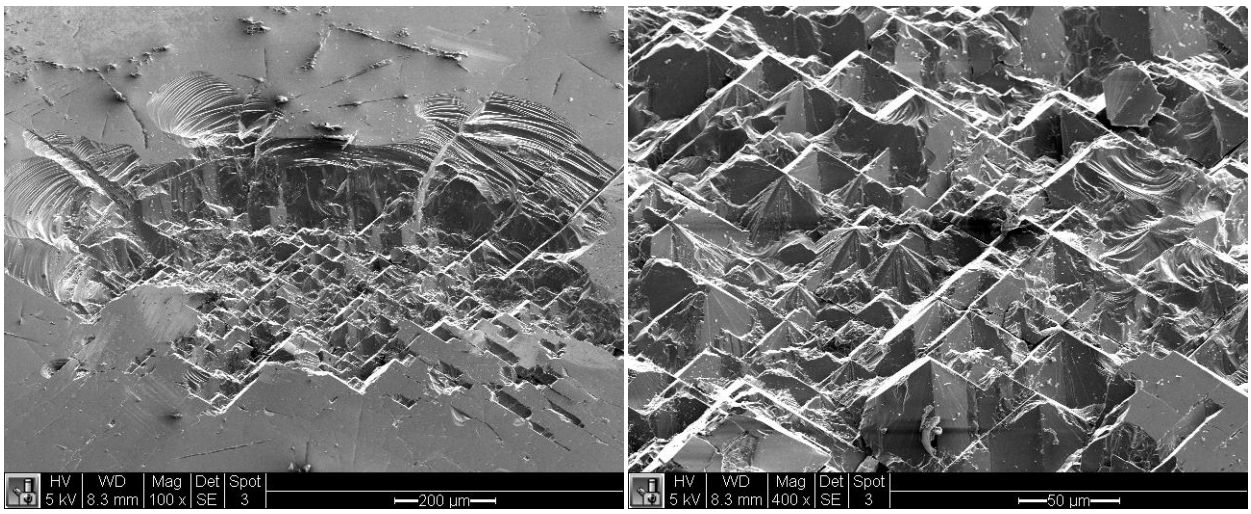

(c) (d)

Figure 3.8: SEM images showing the spall plane from the 5 ns laser (a) and the 50 ps laser (b). (c) and (d) show SEM images of the tilted area from the 50 ps laser spalled area shown in (b). The head-on images allowed accurate measurement of the angles between planes, identifying the {111} surface by their separation angle of ~109.5°.

The peak stress, time averaged strain-rate, rise time, fall time, and full-width-half-maximum for the tests are summarized in Figure 3.9. Under the same energy fluence of $33\ \mathrm{J/cm^2}$ the two lasers are capable of producing $9\ \mathrm{GPa}$ and $7.5\ \mathrm{GPa}$ stress waves, respectively, near the surface of a $500\ \mu\mathrm{m}$ monocrystalline Si wafer. Similar strain-rate (time averaged) of $1-3\times10^{7}\ \mathrm{s^{-1}}$ were achieved in the $50\ \mathrm{ps}$ laser loading with or without confinement, and in the $5\ \mathrm{ns}$ with confinement. Lasers with shorter pulses showed advantage of producing high stresses and strain-rates, even without confinement. This can be advantageous if the power density of interest induces an electric field exceeding the dielectric strength of the confining medium. The shorter pulse duration also showed advantage in producing a more uniform spall plane closer to the surface, allowing better identification of the microstructural features governing the fracture process. Confinement effect showed distinct advantage for longer pulse durations.

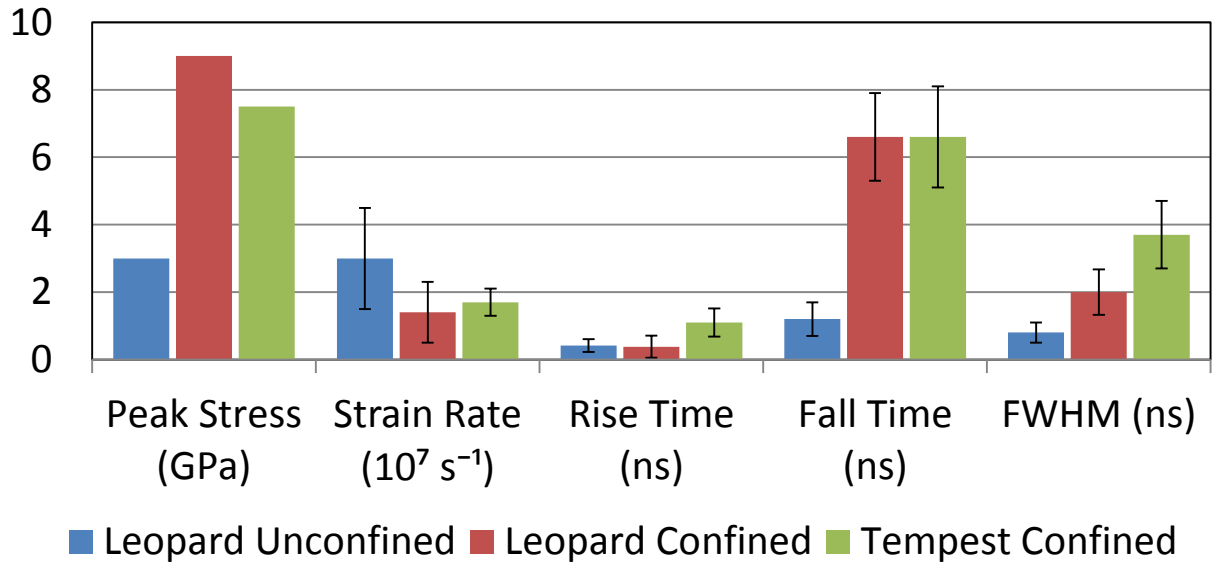

Figure 3.9: Bar graph comparing the peak stress, average strain-rate, rise time, fall time, and FWHM of the four loading cases.

3.5. Direct Observation of Stress Generation and Spallation

The quantitative information gained from interferometry of the surface displacement history was supplemented by nanosecond time-resolved imaging of the rear surface absorption and ablation process, as well as substrate spallation. A single frame intensified camera with 3 ns exposure (Cooke Corportation, dicam pro) was used to capture images of the stress generation and spallation process at the nanosecond time scale. For the stress generation imaging, the laser absorption region was imaged at a shallow angle with respect to the surface to ensure no specularly reflected light from the Nd:YAG pulsed laser was directed into the camera. The laser produced plasma was the object and light source for these images. To ensure the intensified CCD was not saturated by the high intensity of the plasma, two linear polarizers rotated 85° from one another were used to reduce the light intensity to ~1% before entering the camera. A long distance microscope (Infinity K2) was used to capture the ~1 mm diameter spot. During the spallation experiment a flash-lamp with a pulse width

of 30 μs, and a constant intensity plateau of 10 μs, was used to illuminate the surface. Precise timing for triggering of the laser lamp, laser q-switch, illumination flash-lamp, and camera was required to capture the event at the desired time. The delay of the camera was adjusted to vary when each image was taken. Precision timing was achieved by a 4 channel digital delay generator (Quantum Composer). Table 3.1 shows the triggering scheme for each channel (Tempest pulse production is actual light production, which occurs ~123 ns after q-switch pulse and delay) while Figure 3.10 is a schematic of the pulse timing. For both the stress generation and spallation imaging the 5 ns q-switched Tempest Nd:YAG laser was used. The 5 ns laser is superior in its much lower jitter, ~31 ps vs the 500 ns jitter of the 50 ps laser. This makes the 5 ns laser better for accurate timing and trigger performance. The very low jitter of the 5 ns laser is due to its using q-switching for short pulse generation, whereas the 50 ps laser uses active and passive mode locking with cavity dumping.

Table 3.1: Triggering scheme for nanosecond time-resolved optical microscopy.

Delay generator channel:	Pulse width	Delay
1: Tempest lamp	100 μs	0
2: Tempest q-switch	100 μs	190 μs
Tempest pulse production	~ 5ns	190.123 μs ± 31.64 ps (std)
3: Flash-lamp	300 ns	166.623 μs
4: Camera	20 ns	Varies based on sample thickness, but at least 45 ns before pulse production

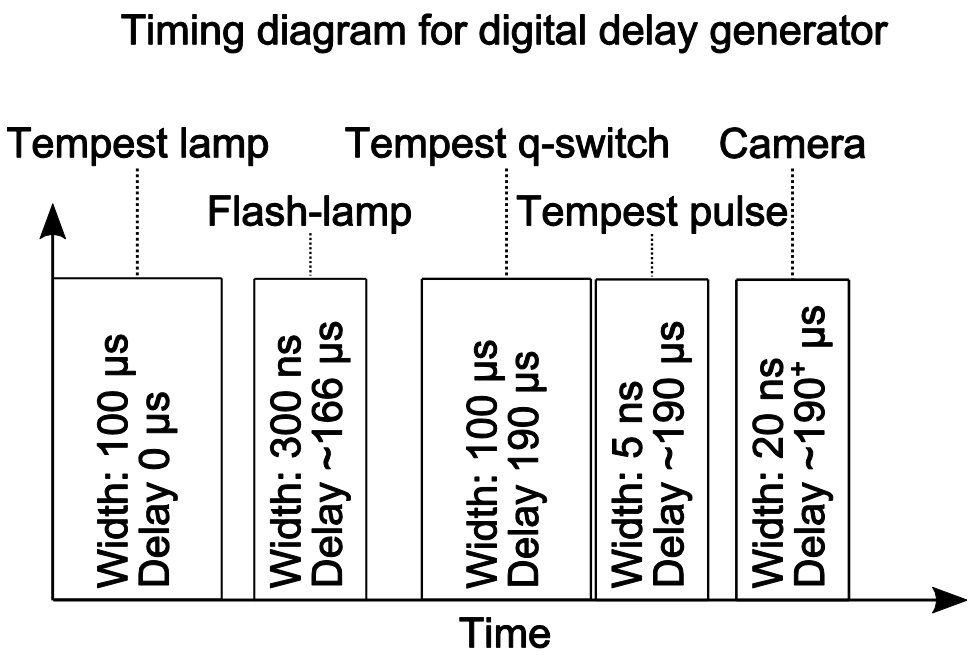

Figure 3.10: Schematic of pulse timing (width and delay) used for nanosecond time-resolved microscopy.

For the stress generation imaging, a bare aluminum plate was used as the target. A single 3 ns exposure was taken, with 1 ns delay between subsequent exposures. Figure 3.11 shows the images taken from delay times of 1-50 ns (time 0 corresponds to the 5 ns laser reaching the target surface). By 2 ns the laser-generated vapor/plasma is bright enough to be readily observed with only 3 ns exposure time. This is the "Knudsen layer", a high electron density layer that forms near the surface due to the rapid ionization. The intensity and diameter of this layer increases as the laser light continues to be absorbed. Starting at 8 ns the layer is observed to grow, expanding away from the target surface. At 19 ns we begin to see the development of the plasma corona. The opacity of the plasma now begins to affect our view of the Knudsen layer, which is becoming obscured due to the increased radiation emission from the volume of the plasma. Whereas initially we are observing the increasing intensity of the circular but flat plasma, at this point the pressure is high enough to cause significant motion, even at the nanosecond time scale. The high pressure causes plasma blow-off, creating a spherical volume. As the intensity of the expanding spherical volume grows the increased opacity prevents the light from

the volume of plasma not within the camera's line of sight from reaching the detector. By 25 ns this spherical volume is well established and continues to expand.

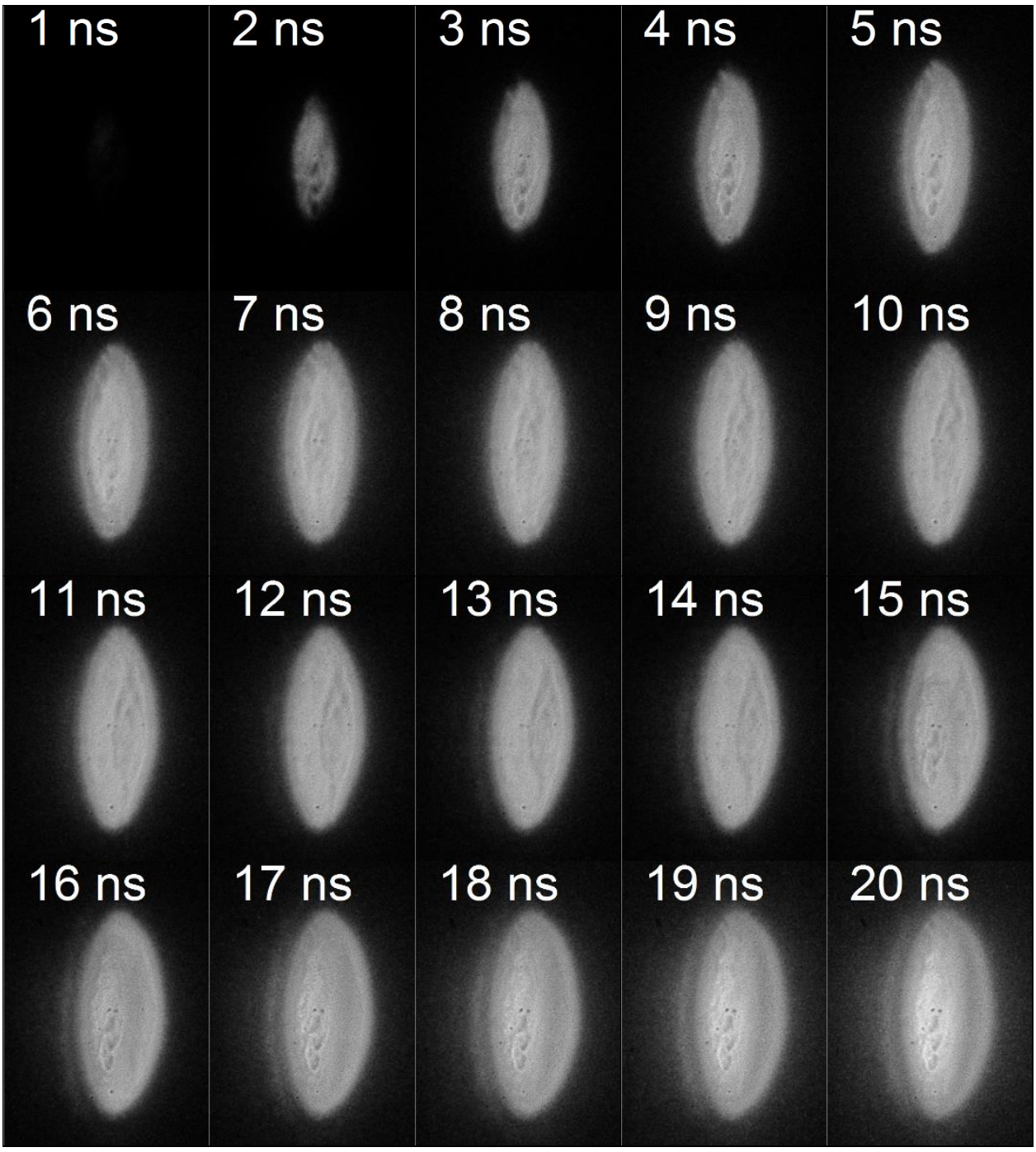

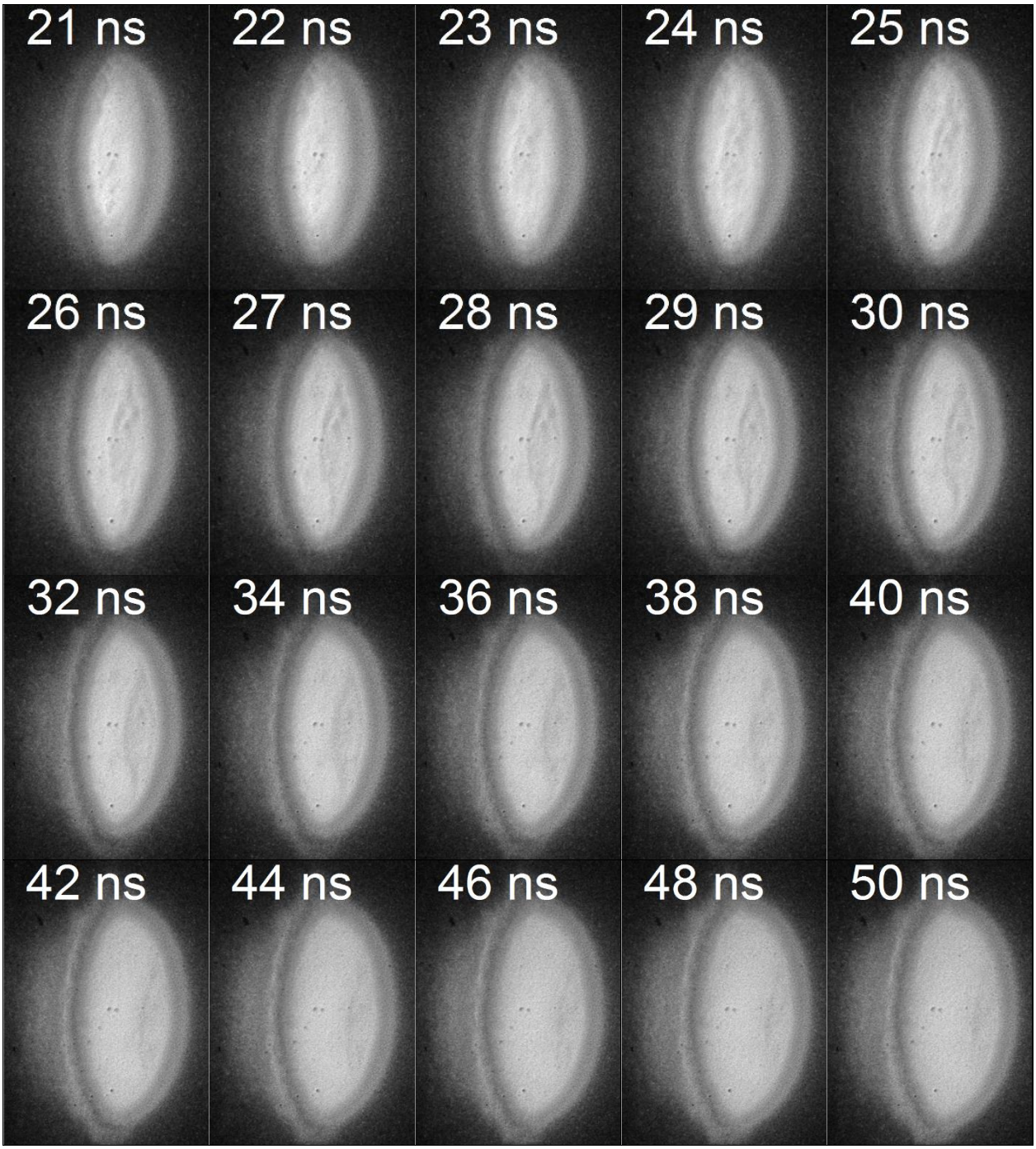

Figure 3.11: 3 ns exposure micrographs of the target ablation, showing the formation and blow off of the laser-generated plasma.

Figure 3.12 shows the normalized light intensity from spatially integrating the intensity of each frame. Peak intensity is achieved at 80 ns. The inset shows the plasma intensity development compared to the 5 ns laser profile. Initially the plasma intensity follows the laser intensity profile for the first 8 ns,

corresponding to the increased area and increased intensity of the laser-generated plasma. From 8-13 ns the plasma intensity levels off. During this time the Knudsen layer is expanding from the initial thin circular profile to the spherical profile characteristic of the plasma blow-off. At 24 ns the rapid growth of the intensity slows down, corresponding to the steepest drop from the 5 ns laser loading profile. The intensity continues to increase, albeit slower, to the peak intensity observed at 80 ns. During this period the energy from the bulk volume of the plasma is being transported from the interior of the plasma to the edge of the radiating surface. From 80-120 ns the light intensity is nearly constant due to equilibrium being reached between the energy transport from the interior of the plasma, due to emission and reabsorption, and the edge of the now spherical plasma volume. From this time onward the intensity steadily decays as the plasma radiates away all the absorbed energy. Stress development corresponds to the initial rapid absorption and expansion of the plasma blow-off while the 5 ns loading laser is actively supplying energy.

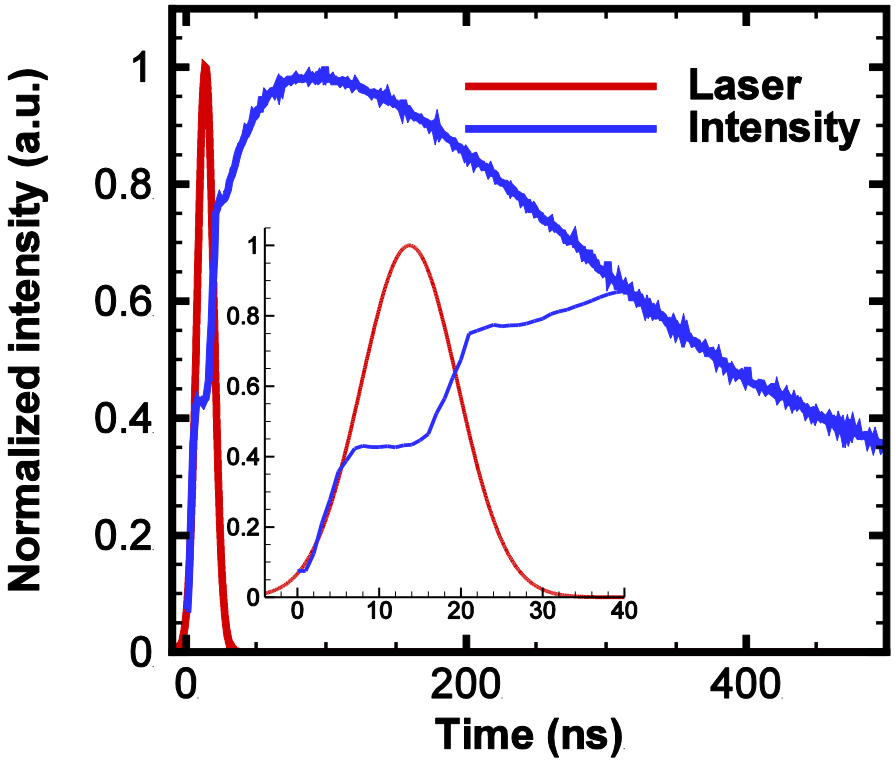

Figure 3.12: Spatially integrated light intensity of the laser-generated plasma vs time (blue). The laser profile is also plotted for comparison to the intensity development (red). Inset is zoomed in on the profile while the laser is supplying energy.

Observation of the spallation process in the silicon substrate was achieved by placing the camera and long distance microscope optics directly in front of the region where the laser-generated stress wave reflects from the sample free surface. Figure 3.13 shows the progression of the surface fracturing from the spallation of the silicon substrate. These images were processed by subtracting the image taken during the experiment from an image taken before stress generation, to highlight any differences as a result of the stress wave interaction. At time t=0 ns a 5^{+} GPa compressive stress wave arrives at the sample free surface and reflects into a tensile wave. At 10 ns a small difference is observed due to the stress wave induced displacement. By 15 ns we see the arrival of the first surface fracture resulting from the spallation process happening below the surface. As time progresses we observe that the

surface fracturing favors the horizontal and vertical directions, corresponding to the [100] in plane crystal directions. The surface fractures branch out in the preferred [100] orientations, quickly expanding to encompass the 1 mm diameter loading region. By 100 ns we observe the beginning of the fragmentation process. At this point the material within the spall thickness (the depth at which the spallation strength was exceeded) continues to fracture and fragment. It carries away with it enough momentum to be completely ejected from the sample. This process continues on a much longer time scale than the stress wave interaction, and we observe at times as long as microseconds the spallation material continues to be ejected from the sample.

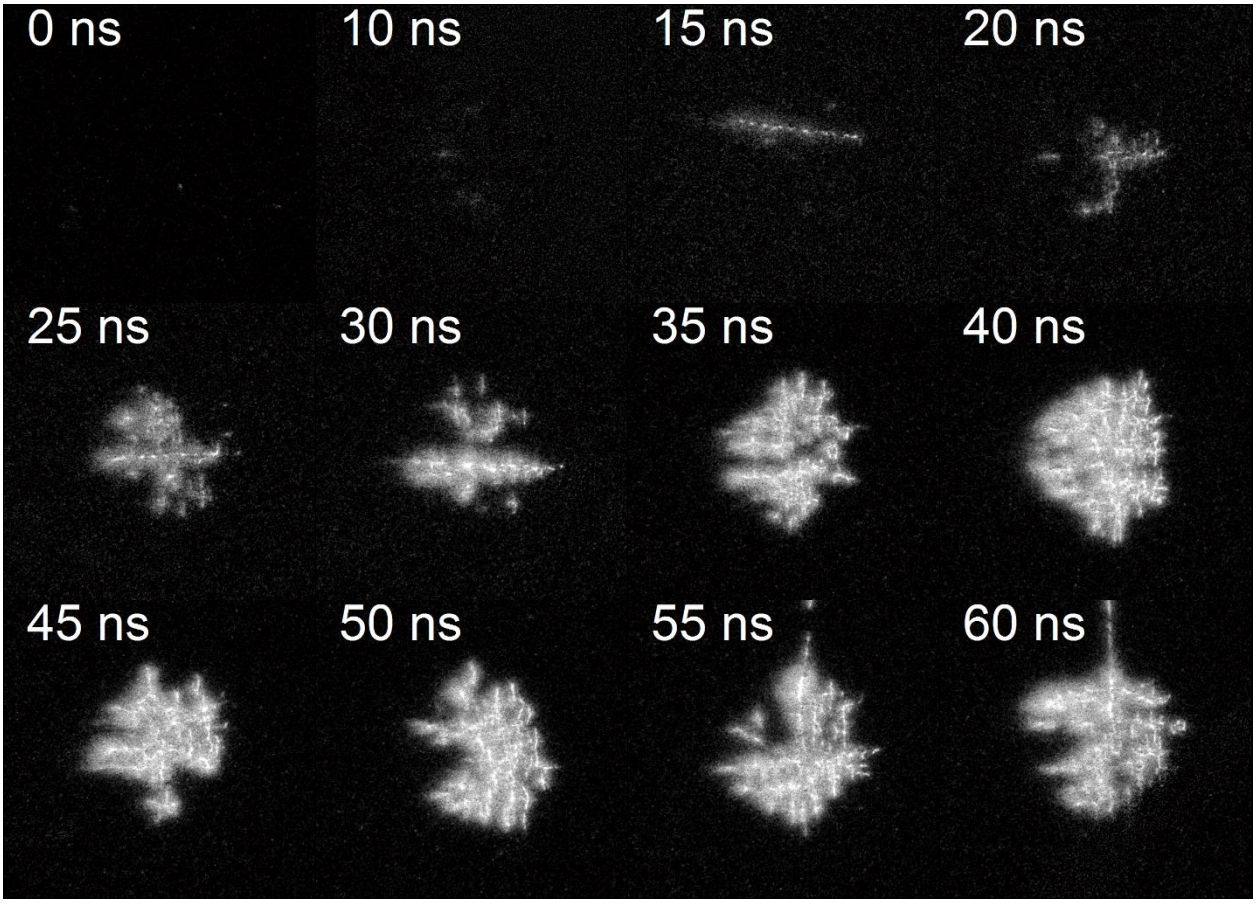

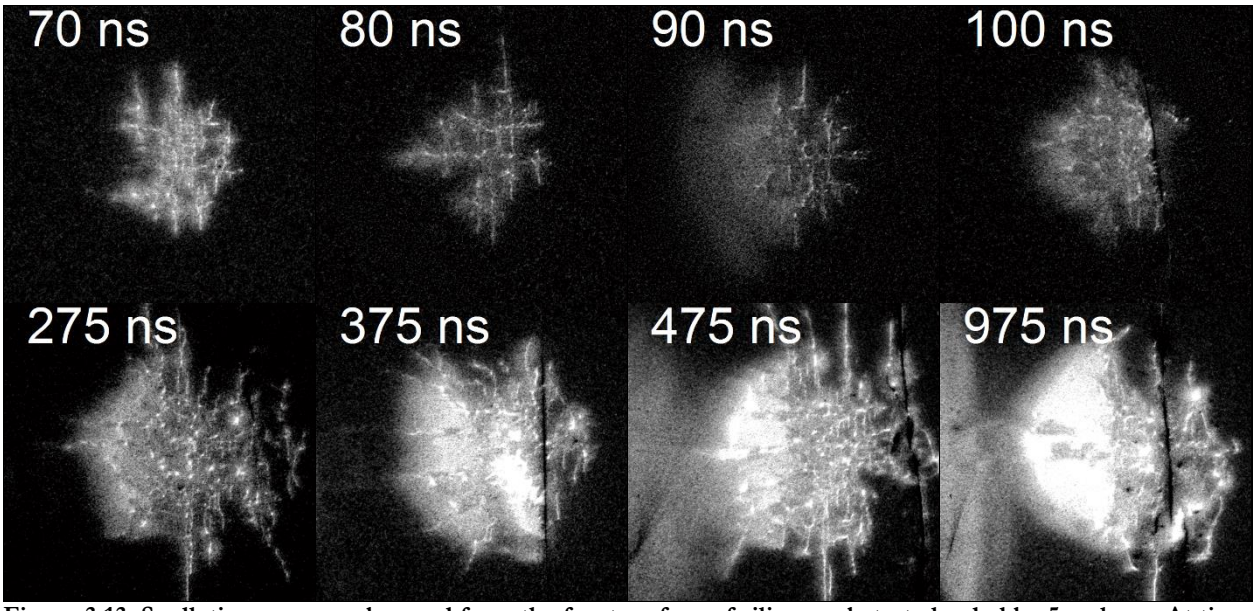

Figure 3.13: Spallation process observed from the front surface of silicon substrate loaded by 5 ns laser. At time t=0 ns a 5^{+} GPa stress wave reflects from the sample free surface. Once the spallation strength of silicon is reached the spallation process begins, with the first surface crack observed at 15 ns.

3.6. Discussion and Conclusion

Quantitative measurement of the stress profiles showed that at low fluences or unconfined conditions, the temporal profiles from both lasers are comparable to that of the input laser pulse. When the fluence is increased or the interaction volume is confined the induced stress wave forms a strong shock loading with decaying unloading profile. Although with a laser pulse duration of two orders of magnitude difference, the 5 ns and 50 ps lasers produced a very similar stress profile under high fluence confined situation. This transition may be attributed to the energy density exceeding that needed to vaporize the energy absorbing layer down to the skin depth, where laser-plasma interactions dominate and dictate the pressure evolution. Classical or collisional absorption of the laser light via electrons oscillating in the laser electric field colliding with ions allows efficient absorption within the laser-generated plasma up to the critical surface (the critical surface develops when the plasma become excited enough that the plasma frequency matches the incoming pulse laser frequency, in which case the laser light is no longer efficiently absorbed). This may explain why the 5 ns loading exhibits such

a drastic difference as the fluence is increased (even at low fluence the energy density is above the threshold for vacuum plasma ignition of $\sim 2\ \mathrm{J/cm^2}$ [118]). At low fluence the time to vaporization is comparable to the pulse width, while at high fluence it becomes negligible. For the $50\ \mathrm{ps}$ Leopard laser, due to the reduced pulse width, the time to vaporization is negligible for both low and high fluence. Additionally, due to the difference in pulse duration, the $5\ \mathrm{ns}$ laser has a much larger thermal diffusion depth than the $50\ \mathrm{ps}$ laser ($1.3\ \mu\mathrm{m}$ vs $130\ \mathrm{nm}$ for the diffusion depth for $5\ \mathrm{ns}$ vs $50\ \mathrm{ps}$ laser pulses, respectively). This requires the $5\ \mathrm{ns}$ laser to expend more pulse energy on heating/melting/vaporizing since the interaction volume will be larger. Stress generation with confinement with the $5\ \mathrm{ns}$ laser at low fluence allows low pressure, low strain-rate (for laser spallation) loading. If the stress being produced is adequate but increasing the strain-rate is of interest, the $50\ \mathrm{ps}$ Leopard laser without confinement can be used to generate a similar level of stress, but the strain-rate is doubled. Postmortem SEM imaging of the spallation plane showed a dominance of spall fracture along the {111} planes. For the 50 ps laser the spall fracture was closer to the surface and the {111} fracture surfaces were more uniform and prominent. This is attributed to the much faster unloading from the 50 ps laser profile which allows the spallation to happen in a narrow plane. Nanosecond time-resolved microscopy of the stress generation process revealed formation of a thin plasma layer near the surface, which rapidly expands during laser absorption. The increase in the laser-generated plasma intensity correlates with the loading laser profile. Direct observation of the spallation process indicated that the first process observable at the sample surface is fracturing. The surface fracturing favors the in plane [100] directions. The [100] directions coincide with the intersection of the favored {111} planes, indicating that the process and mechanism of the spallation agree on both the nanosecond time scale (observation of surface fracturing in the [100] direction) and postmortem long term observation (SEM indicating preferable {111} spallation planes).

The study confirmed that the previous thermoelastic model [123] is only valid for low laser intensity or unconfined absorption volumes. Under such conditions, the laser-generated stress profile remains as a copy of incident laser pulse. As the laser intensity increases or under the effect of confinement, the stress will lose the conformity to the incident laser pulse. As the pulse duration shortens from nanoseconds to picoseconds, the generated stress profile converges to that generated by nanosecond laser.

Chapter 4. Compressive Yielding of 6061 & 7075 Al from Pulsed Lasers

Aluminum is a widely used structural material due to its reasonable compromise between strength, ductility, corrosion resistance, and density. As such it is desired to understand the behavior of aluminum subjected to a wide variety of loading conditions, including high strain-rate loading. Impacts which induce high rate deformation of aluminum occur frequently, e.g. vehicle crashes. Aluminum is largely rate insensitive, though some measurements at ultra-high strain-rate indicate a sudden increase in the spall strength in the region of 10^8 s^{-1} [88]. Thus aluminum provides a material which may help elucidate differences in laser-induced material behavior between nanosecond and picosecond illumination.

4.1. Sample Preparation

6061 and 7075 Al alloys were obtained from McMaster-Carr in 1" diameter bar stock with precision ground finish. The precision ground rods have tight tolerances for the diameter and straightness. Both are specified by ASTM standards ASTM B211 or B221. ASTM B221 scope specifies certain aluminum and aluminum alloys of extruded bars, rod, wire, profile and tubes with certain tempers whereas ASTM B211 covers much of the same materials but those which are rolled or cold-rolled bar, rod and wire. Table 4.1 lists the Al alloy composition limits for alloys 6061 and 7075 given by ASTM B211 & B221.

Table 4.1: Aluminum Alloy Composition Limits per ASTM B221. If no range is given the number represents the maximum allowed.

Alloy	Si	Fe	Cu	Mn	Mg	Cr	Zn	Ti	V	Other (total)	Al
6061	0.40-0.8	0.7	0.15-0.40	0.15	0.8-1.2	0.04-0.35	0.25	0.15	…	0.15	remainder
7075	0.40	0.50	1.2-2.0	0.3	2.1-2.9	0.18-0.28	5.1-6.1	0.20	…	0.15	remainder

Alloy 6061 has magnesium (Mg) and silicon (Si) as its major alloying elements and is characterized (among the aluminum alloys) by good formability and corrosion resistance. The major alloying elements for alloy 7075 are zinc (Zn), magnesium, and copper (Cu) and are characterized by high strength and fatigue performance. 6061 is a widely used general purpose Al alloy while 7075 is a high strength alloy with better corrosion resistance than other high strength Al alloys (e.g. 2024). Both alloys are heat treatable for precipitation or age hardening, where dislocation barriers are created by fine impurity particles solubilized out of the solid solution at high temperature. Both were provided with the T6511 temper which specifies (per ANSI H35.1, "Alloy and Temper Designation Systems for Aluminum") that (T) the alloy has been thermally treated to produce stable tempers. T6 designation indicates the alloy was solution heat treated and artificially aged. Solution heat treatment consists of heating to and holding at a suitable temperature to allow constituents to enter solid solution, then cooling rapidly to ensure they remain. By this process the alloying elements are allowed to substitutionally diffuse into Al atom positions to form the solid solution, then the material is quickly cooled to prevent them from diffusing back. Due to the small percentage of the alloying elements the precipitates tend to be small and finely dispersed through the metal. Temper T6 alone produces residual stresses due to the thermal gradient produced when quenched in water after heat treatment. The designation T_511 indicates the alloy was stress relieved by stretching after heat treatment to 1-3% permanent set, then straightened after stretching.

Table 4.2: Aluminum Alloy Strength Specification (per ASTM B221). Other tempers included for comparison. Temper O is annealed to achieve lowest strength. Temper T1 are cooled from elevated temperature and naturally aged.

Alloy	Temper	Tensile Strength, ksi (MPa) [min or max]	Yield Strength, ksi (MPa) [min or max]
6061	O	22.0 (151.7) [max]	16.0 (110.3) [max]
	T1	26.0 (179.3) [min]	14.0 (96.5) [min]
	T6	38.0 (262.0) [min]	35.0 (241.3) [min]
	T6511	38.0 (262.0) [min]	35.0 (241.3) [min]
7075	O	40.0 (275.8) [max]	24.0 (165.5) [max]
	T6	81.0 (558.5) [min]	73.0 (503.3) [min]
	T6511	81.0 (585.5) [min]	73.0 (503.3) [min]

Table 4.2 lists the strength limits for alloys 6061 and 7075 in annealed and aged states. Pure Al has very low yield strength (~10 MPa), but alloying and tempering significantly strengthen the material. Annealed 6061 has a yield strength ~110 MPa while tempered T6 and T6511 have yield strength of ~240 MPa. Alloy 7075 shows the same trend, with annealed strength of ~170 MPa and tempered strength of ~500 MPa. Since these are not actual measurements but required minimum/maximum strengths, they only provide a baseline expectation for our samples.

The 1" diameter alloys Al rods were cut into thin disks using a band saw. The faces of the cut disks were then fly cut to ensure a planar face for lapping and polishing. The samples were successively lapped with silicon carbide abrasive disks with 600, 800, and 1200 grit. The Al samples were then fine polished with 1 μm and 0.05 μm alumina slurry on a low nap, soft, micro-cloth until a mirror finish was achieved. The final sample preparation step is the spin coating of pure water glass onto the back surface, creating a confining layer which allows the transmission of the laser pulse but confines the

lasers interaction with the sample. This confinement greatly enhances the stress generation, as discussed in Chapter 3.

4.2. Experimental Method

To achieve high strain-rate loading of the Al alloys high pressure, short duration stress waves were generated by short pulsed Nd:YAG lasers. 5 ns and 50 ps pulse durations were used. Both pulses have Gaussian temporal profiles and similar energies: up to 300 mJ with the 5ns pulse; up to 260 mJ with the 50 ps pulse. By use of a wave plate and thin film plate polarizer the energy can be finely controlled. The sample geometry is similar to that shown in Figure 3.2 for the bulk testing of silicon, but the substrate of interest was aluminum. Time resolved measurement of the free surface displacement was accomplished via a Michelson interferometer, as shown in Figure 3.1. From the free surface displacement the substrate stress was calculated using Equation 7.

4.3. Behavior from Nanosecond Pulsed Laser

Initial studies were conducted on 6061 Al using the 5ns Tempest pulsed Nd:YAG laser. Sample thickness was 1.696 mm. The energy was varied from 67-255 mJ to study the effect of the pulse energy. Figure 4.1 shows the effect of increasing the energy on the substrate stress. At low energies the response of the aluminum is an elastic wave with peak stress of <300 MPa and a Gaussian temporal profile. As the energy is increased there is a clear transition from the low amplitude elastic response to a very sharp shock front followed by a flat plateau. The transition from the low energy, low

amplitude elastic response indicates that other mechanisms beside elastic wave propagation have been activated.

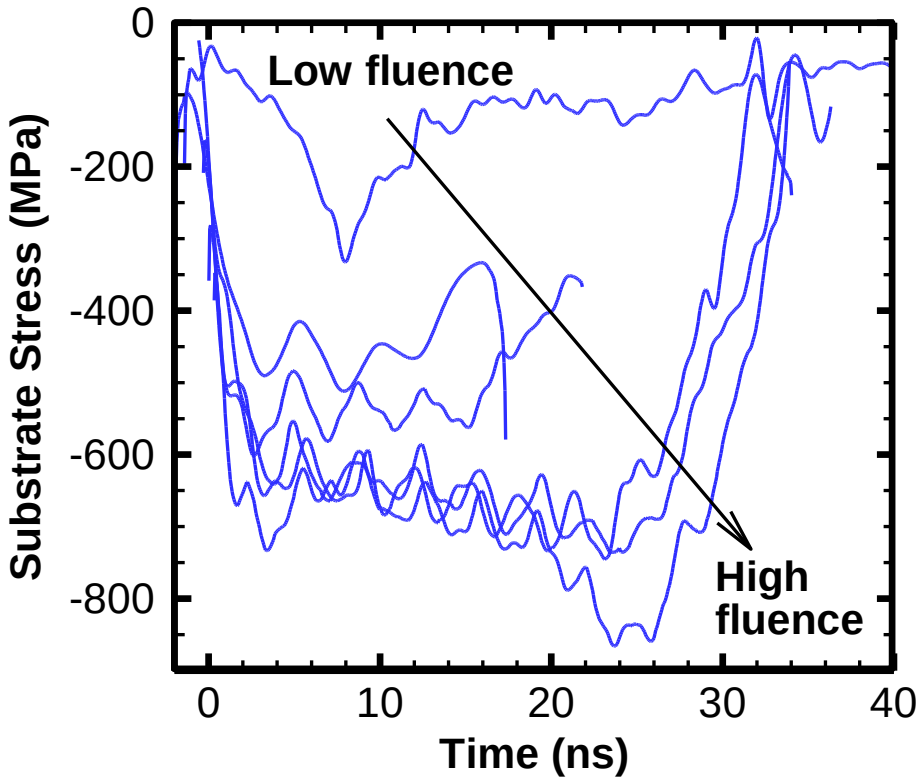

Figure 4.1: Substrate stress history trend as the laser energy is increased. At low laser energies the behavior is elastic with a Gaussian profile similar to the incident laser pulse. As the energy is increased plastic behavior is seen, with a very sharp shock front followed by a flat plateau. The transition is indicative of compressive failure.

The significant deviation from the nominal Gaussian profile of the 5 ns laser is a strong indication that the material yielded from the loading. The surface of the sample had visible blemishes corresponding to the testing site. Line scanning profiles across the testing site were performed with a profilometer to determine whether the blemishes were convex or concave and the extent of deformation (as a convex deformation could indicate failure from spallation). Figure 4.2 shows a scan on the 1 mm testing area, with an additional 1 mm scanned on both sides. The concave surface

deformation affects an area much larger than the testing site and is indicates compressive yielding behavior.

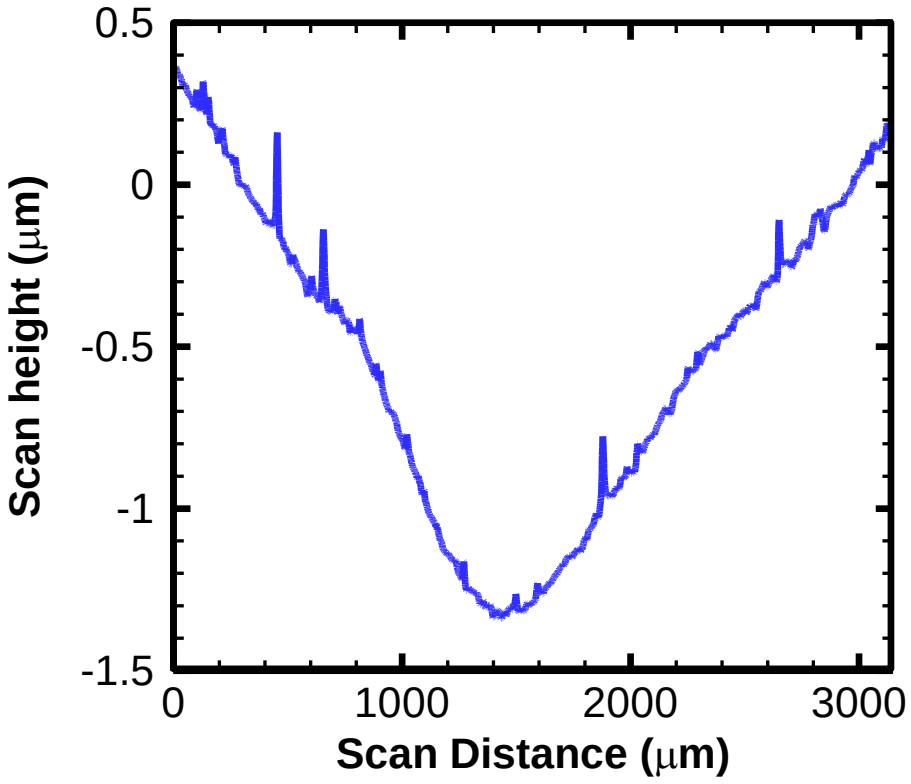

Figure 4.2: Profilometer measurement across front surface showing a gradual crater.

Compressive yielding is the result of resolved shear stresses exceeding the material strength. For laser-induced stress waves the affected volume is in a condition of uniaxial strain. Only the longitudinal stress is measured, and at yield this is referred to as the Hugoniot elastic limit (HEL). By use of a failure model, e.g. Tresca, the longitudinal stress can be related to the yield strength. Assuming isotropic linear elastic behavior the measured longitudinal stress is related to the lateral stress by:

$$\sigma_y = \frac{\nu}{1-\nu}\sigma_x \tag{14}$$

By the Tresca yield criterion

$$\sigma_x - \sigma_y = Y \tag{15}$$

Combining (14) & (15) gives the relation between the HEL (measured) and the yield strength:

$$\sigma_{HEL} = \frac{1-\nu}{1-2\nu} Y \tag{16}$$

Poisson's ratio for Al alloys are typically close to 1/3, so the HEL is twice the yield strength, i.e. for $\nu = 1/3, \quad \sigma_{HEL} = 2Y$. For the 1.696 mm 6061 Al sample tested with the Tempest laser we see a consistent transition to the plateau behavior around 500-600 MPa which corresponds to a yielding range of 250-300 MPa. This is reasonable and it should be noted that the ASTM standard only states minimum yield strength of ~241 MPa.

Another parameter that was investigated was the thickness of the sample. A 0.940 mm thick 6061 Al alloy sample was prepared and tested with the Tempest laser. Figure 4.3 shows a typical set of data, starting with the raw interferometric signal at the top of the figure, with the reduced free surface displacement and resulting substrate stress implied by that displacement on bottom.

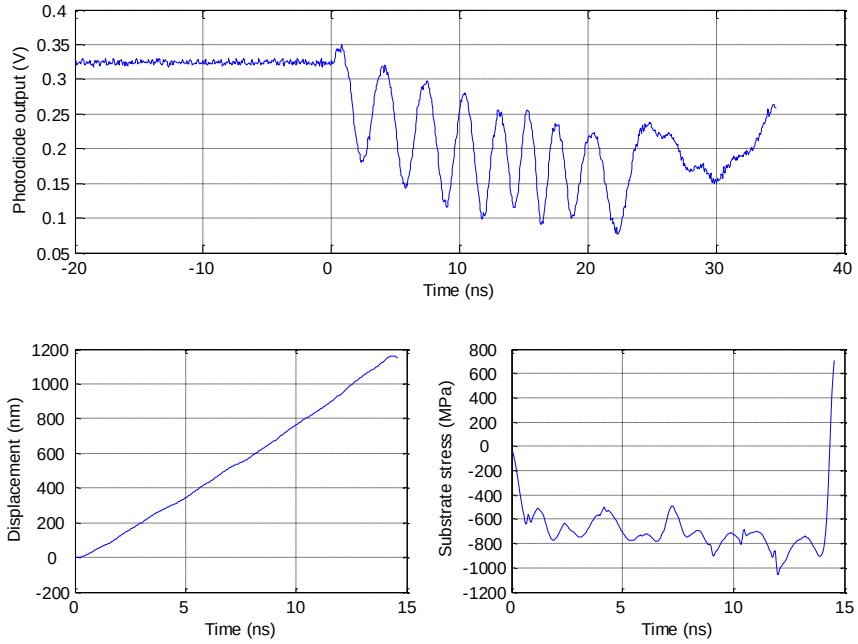

Figure 4.3: Typical data for 0.94 mm thick 6061 Al with Tempest, full energy.

The substrate stress quickly rises to ~600 MPa where the wave profile assumes a nearly linear profile with the substrate stress reaching ~1GPa in compression before reversing. The very sharp front of the stress wave could be shock induced or elastic-plastic induced behavior (shock from the loading, as opposed to shock from the material behavior transition due to plastic wave steepening). Figure 4.4 shows the compilation of full energy testing on the 0.94 mm 6061 Al sample. The trends for the transition stress, stress profile, and pulse width are consistent from shot to shot. As compared to Figure 4.1 we see that the 0.94 mm 6061 Al response has a shorter pulse width and appears to be compressed compared to the thicker 1.696 mm sample.

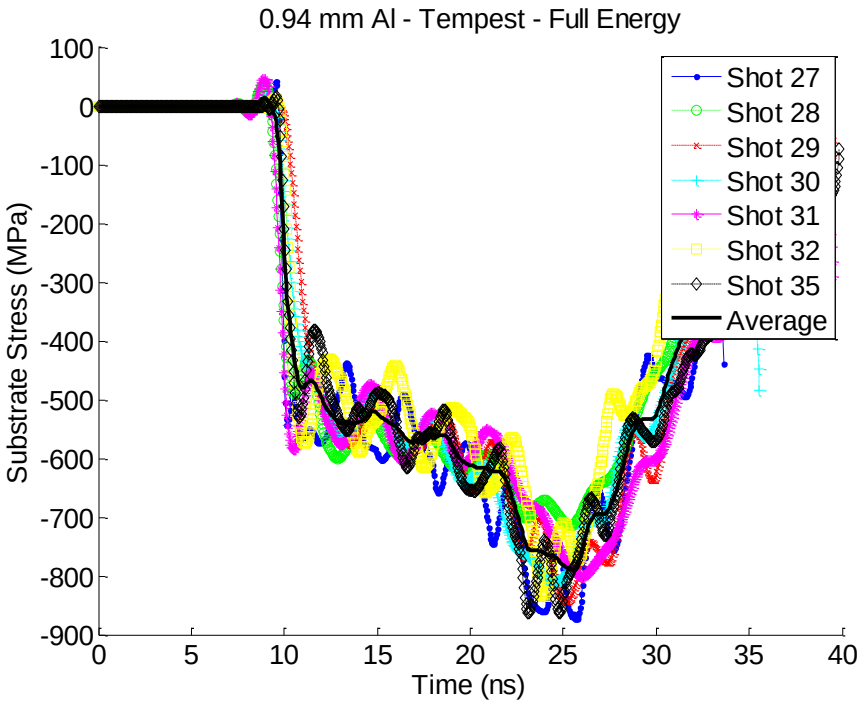

Figure 4.4: 0.94 mm 6061 Al sample tested with Tempest laser at full energy. Shots showed high repeatability with elastic-plastic transition in the 500-600 MPa range.

Conservation dictates that the area of the stress pulse at best remains constant. A typical process for pulse broadening is the attenuation of the peak stress with the area under the attenuating peak contributing to broadening the pulse width. This momentum diffusion is possible through nonlinear mechanisms such as nonlinear elastic or plastic response. Figure 4.5 shows two pulses which corroborate the attenuation and broadening of the stress pulse as it propagates farther into the sample. The peak stress of 1+ GPa at 0.94 mm has attenuated to ~850 MPa while the pulse broadened from 15 ns (at peak stress) to 27 ns. Due to the nature of the interferometric signal the transition from elastic to plastic behavior is best resolved when it happens in the middle of a fringe traversal, where the displacement intensity relationship is roughly proportional. If the transition coincides with a fringe peak or valley the resolution is reduced due to the sinusoidal nature of the signal.

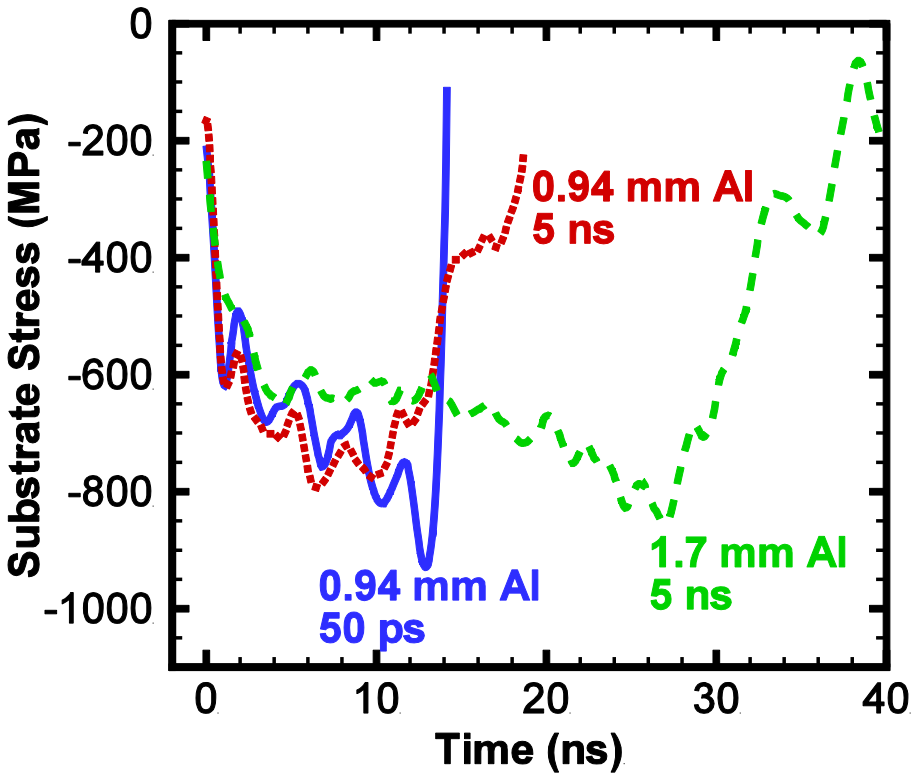

Figure 4.5: Comparison of 0.94 and 1.696 mm 6061 Al response to full energy loading by the Tempest laser.

4.4. Behavior from Picosecond Pulsed Laser

The pulse width of the Leopard laser is 50 ps, 1/100th the pulse width of the 5 ns Tempest laser. Such a rapid pulse could feasibly drive the 6061 Al sample to different material response. Since aluminum is largely rate insensitive at lower strain-rates, differences observed in material behavior from the Tempest to the Leopard laser may be attributable to the difference arising from the shorter pulse duration. Understanding any differences in the mechanisms is essential for proper application of the different duration pulses. The 0.94 mm 6061 Al sample was also tested with the Leopard laser. The samples showed a variety of material behavior, most similar to the Tempest.

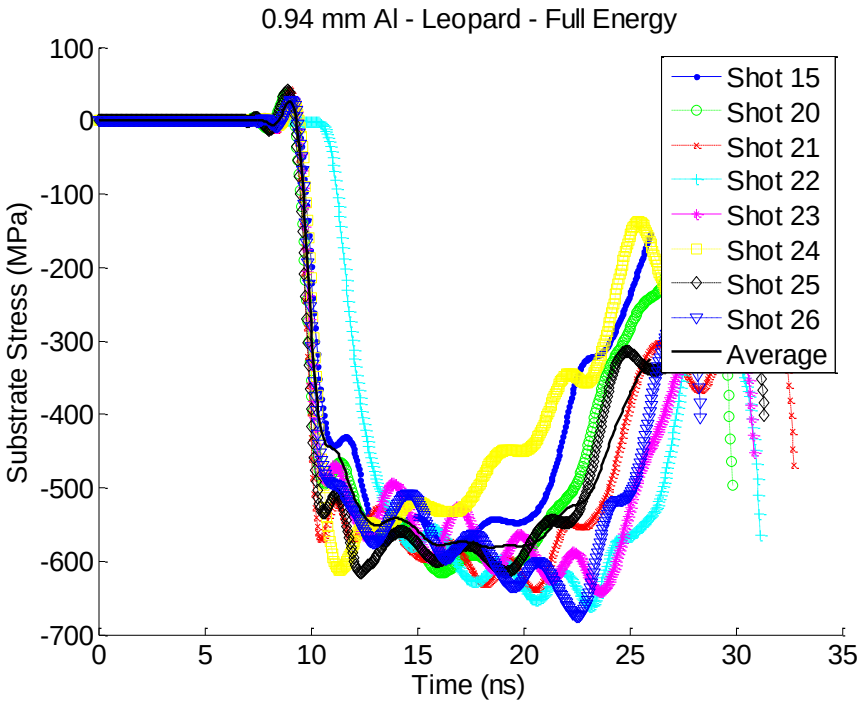

Figure 4.6: Substrate stress profile from full energy testing with Leopard laser – 0.94 mm 6061 Al.

Figure 4.6 shows a collection of reduced substrate stress profiles from the 0.94 mm 6061 Al sample tested with the Leopard laser. The data look very similar to the Tempest profiles. There is a very sharp shock front with a transition in the 400-600 MPa range and the pulse width is shorter by ~3 ns. While aluminum's rate insensitive response is desirable, the material yields too quickly and at too low of a stress for good comparison. The complicated elastic-plastic response also makes it difficult to discern whether the very sharp shock fronts are a result of the pulse deposition and stress generation, or if they are the result of complicated material response. At this propagation distance it is likely that the stress wave has evolved into a similar profile from both the 5 ns and 50 ps lasers.

Table 4.2 lists the tensile and yield strengths for 6061 and 7075 aluminum alloys with various tempers. Comparing the yield strengths indicates that 7075 Al alloy is a good candidate material to study with

the Leopard laser since the minimum strength specified for the T6511 temper is ~500 MPa. With Poisson's ratio ~ 1/3, Equation 16 gives a longitudinal stress at yield of ~1 GPa. The higher yield strength should allow us to study the elastic material response with both Tempest and Leopard lasers. The elastic response is ideal for comparison since it will indicate if the Leopard laser generates stress waves with the same temporal profile (i.e. Gaussian with 50 ps full-width-half-maximum) and if the stress amplitude is proportional to the input energy. The efficiency of the stress generation may be proportional to the laser intensity, which is much higher for the Leopard laser since it delivers the same energy in 1/100th the time.

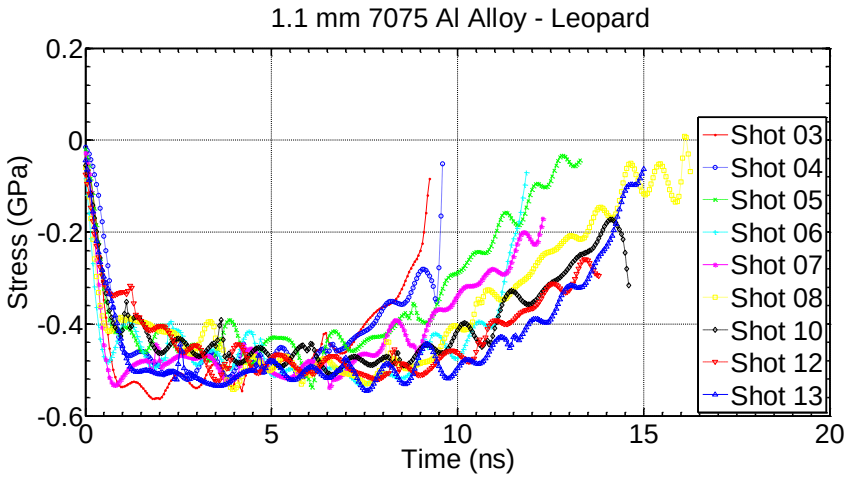

Figure 4.7: Representative data for the plateau waveform for 1.1 mm 7075 Al alloy tested with Leopard laser at full energy.

Figure 4.7 shows some of the data from the 1.1 mm 7075 Al alloy testing. The plateau waveform, as seen with previous testing, was the most prevalent. For the Leopard laser testing there does not seem to be as strong of correlation between energy and pulse width as was seen with the Tempest testing. The pulse widths are slightly shorter than the previous Leopard test, with the 1.1 mm 7075 pulse width ranging from 7-10 ns as compared to the 0.94 6061 Tempest pulse widths from 12-15 ns. The 7075 Al alloy pulse shape is a flatter plateau, without the rising stress tendency seen with 6061 sample. Most

notably, the transition from the sharp shock front to the plateau is at a similar stress level, 400-600 MPa. This transition level is several hundred MPa lower than expected.

A 7075 Al sample of 1.18 mm thickness was prepared without the confining layer and tested under the same circumstances, to enable comparison with the elastic-plastic transition observed with the 5 ns pulsed laser. Overall the data was poor, mostly due to the high noise and low displacement. Some samples did not displace enough for a full half fringe while for others too much of the displacement was near the maximum or minimum inflection, where sensitivity of the interferometer is lowest. Figure 4.8 shows the data from a successfully reduced and analyzed shot (the peak near 80 mV corresponds to the peak observed from the peak-to-peak signal during calibration). The stress profile and level are similar to the elastic response observed from the 5 ns laser, but the pulse width is now much shorter due the 50 ps laser.

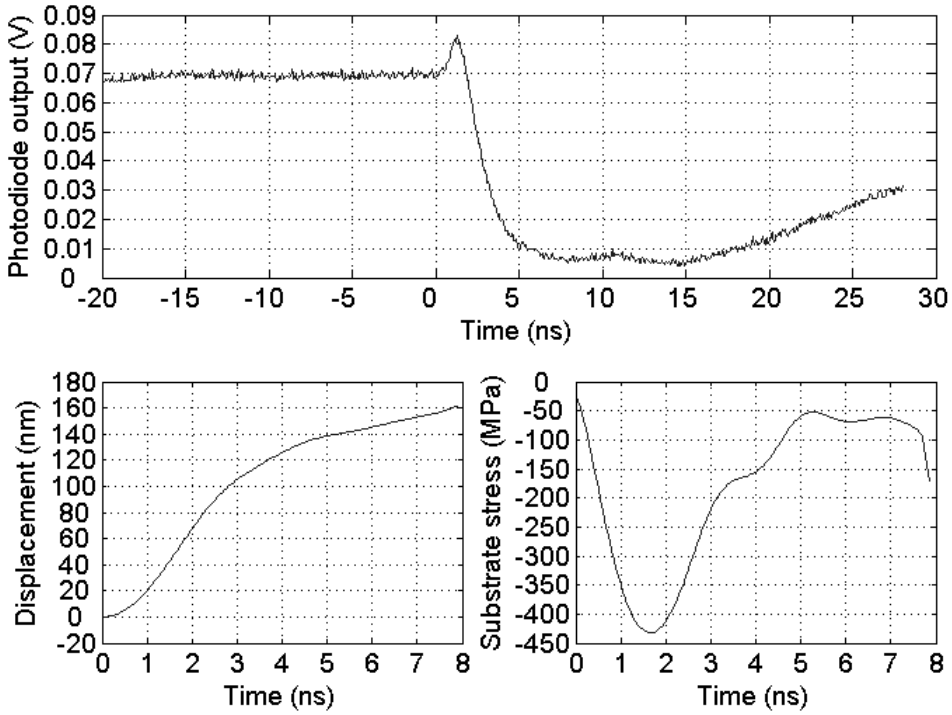

Figure 4.8: Raw interferometric signal, displacement and substrate stress for 1.18 mm 7075 Al alloy without a water glass confining layer.

Follow up testing was performed on thicker 7075 Al alloy samples to determine if the observed waveforms from the thinner samples would evolve with farther propagation distance. Changes with longer propagation can indicate attenuation, plastic dissipation, or non-linear processes. If no changes are observed then it is likely the wave is not a steadily propagating elastic wave. It will still be subjected to geometric attenuation, but at propagation distances less than 3x the spot size it should be minimal.

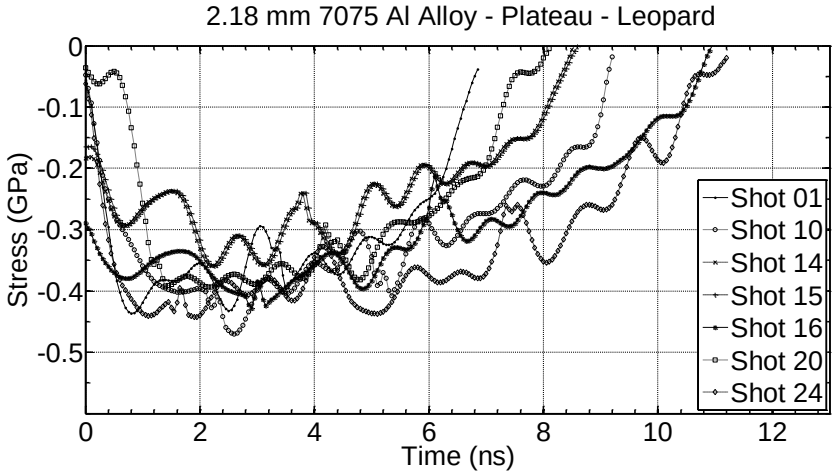

(a)

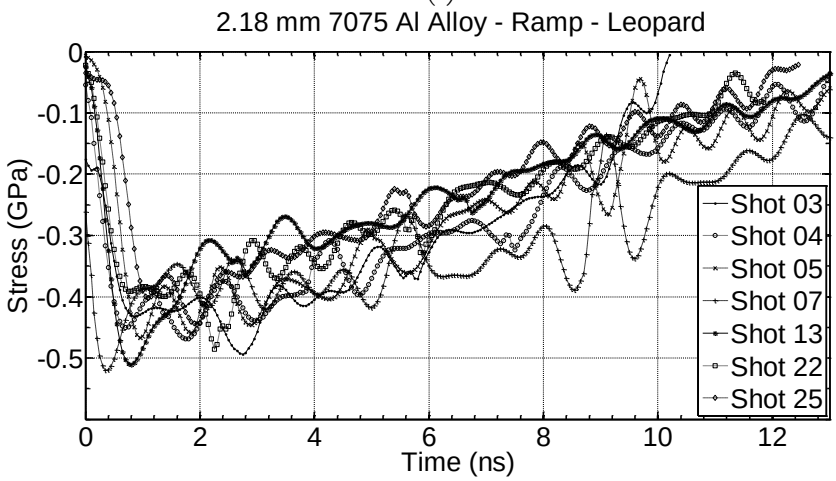

(b)

Figure 4.9: Typical waveforms observed for 2.18 mm 7075 Al alloy showing a plateau (a) or ramp (b) substrate stress profile.

Figure 4.9 shows two typical substrate stress profiles observed during testing of the thicker 2.18 mm 7075 Al alloy: a plateau profile (a) very similar to previous testing; and a ramp profile (b). The plateau profile shows a consistently lower transition stress level of ~300-400 MPa compared to the previous ~400-600 MPa trend. Pulse widths have varied with the Leopard laser, but the 2.18 mm sample pulse width appears shorter then that observed with the 5 ns laser. The initial elastic rise is not as sharp and stretches to nearly 1 ns for some shots. The bottom figure shows another consistent substrate stress profile with a very sharp initial stress rise followed by a gradual ramp-like decrease. All shots were conducted under similar conditions, therefore there does not seem to be a preferred profile for a given

test. A strong shock front with ramp decompression is an indicator of possible non-linear behavior. The ramp profiles consistently show a higher initial stress than the plateau response. This response is very similar to that observed from the bulk Si studies in term of the rise and fall time, but the aluminum response seems to be a consistent linear ramp rather than exponential decay.

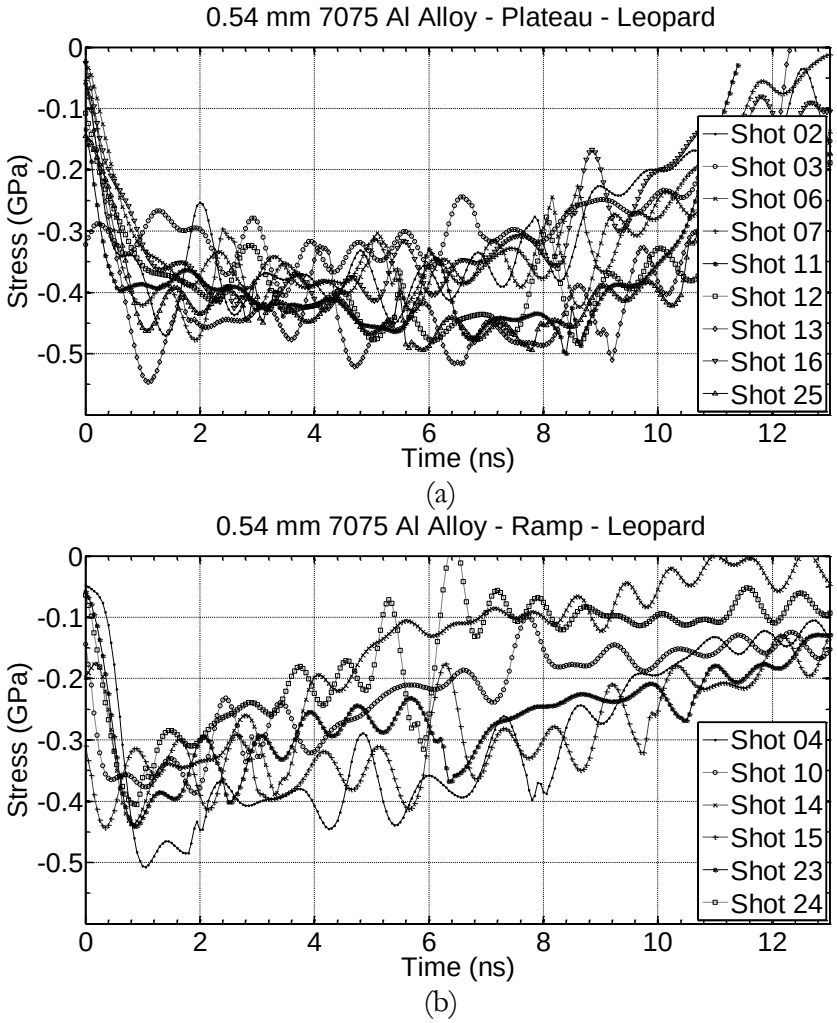

Figure 4.10: Plateau (a) and ramp (b) response of a 0.54 mm 7075 Al alloy sample tested with the Leopard laser.

For a complete picture of the stress propagation through the 7075 Al alloy samples loaded by the Leopard laser a thinner, 0.54 mm sample was prepared and tested. Figure 4.10 shows that the plateau (a) and ramp (b) profiles observed from the 2.18 mm 7075 Al sample are also present at shorter propagation distances. Stress amplitude is similar for both stress profiles and still consistently lower

than the expected ~1 GPa longitudinal stress at yield. The ramp profile is not nearly as defined as the 2.18 mm sample, but the deviation from the plateau is still evident. This may indicate that the decay unloading observed in Si and the 0.54 mm 7075 Al may evolve into the linear unloading ramp observed in Figure 4.9 (b) for longer propagation distances.

4.5. Discussion and Conclusion

Testing with laser pulse widths of 50 ps and 5 ns leads to a variety of material behavior. For 6061 Al alloy loaded with the Tempest laser very consistent substrate stress profiles with fast elastic shock followed by linearly increasing ramp were observed. The stress at which this transition occurred ranged from 500-600 MPa, indicating a yield strength of 250-300 MPa for rate-insensitive behavior. This value is consistent with the literature for similar loading conditions at lower strain-rates [129]. The same material tested with the Leopard laser showed similar behavior. For the Leopard laser the transition stress was also consistently between 500-600 MPa, but after the yielding the stress did not tend to increase as much. Loading by the Tempest laser led to a peak stress after yielding of ~800 MPa, while peak stress for the Leopard laser after yielding was ~700 MPa (0.94 mm sample). The pulse width from the Leopard laser was also shorter.

7075 Al alloy tested by the Leopard laser showed that yielding occurred nearly instantaneously even at very low energies. This indicates the Leopards enhanced stress generation due to its shorter pulse width. The 7075 alloy did not show any trend for increasing stress after yielding, and instead favored a flat plateau, which can be attributed to much quicker elastic-plastic transition behavior. Samples as thick as 2.18 mm were tested and indicated the stress profile was not evolving with distance, e.g. a

steady elastic wave was reaching the front surface. In addition to the flat plateau, ramp unloading was also observed, with an overall pulse width 2-4 ns longer than the plateau response. Yield was observed at stresses of 300-400 MPa, indicating yield strength of 150-200 MPa. This is much lower than the yield strength of 500 MPa specified by ASTM B221. This is likely due to the 7075 not being in the tempered state.

Chapter 5. Finite Element Simulation of Cell-Substrate Decohesion by Laser-induced Stress Waves

5.1. Introduction

Cell-substrate adhesion is a fundamental process that plays a critical role at bio-interfaces. For biomedical applications, such as tissue response to implanted devices, a quantitative understanding of cell-substrate adhesion is necessary for successful development and optimization of biomedical devices. Various techniques have been developed to investigate cell–substrate adhesion. Commonly used techniques are hydrodynamic flow, centrifugation, and micromanipulation methods. Hydrodynamic flow uses the shear stress of a fluid to detach adherent cells. The ratio of adherent cells before and after the test is considered indicative of the adhesion strength of the cells [130–132]. In the centrifugation method, by controlling the rotation speed of a standard lab centrifuge, a normal force can be used to detach adherent cells from a substrate [133]. Using micromanipulation techniques including atomic force microscopy (AFM) [134], nanoindentation [135], and optical tweezers [136–139], the adhesion of single cells can also be studied.

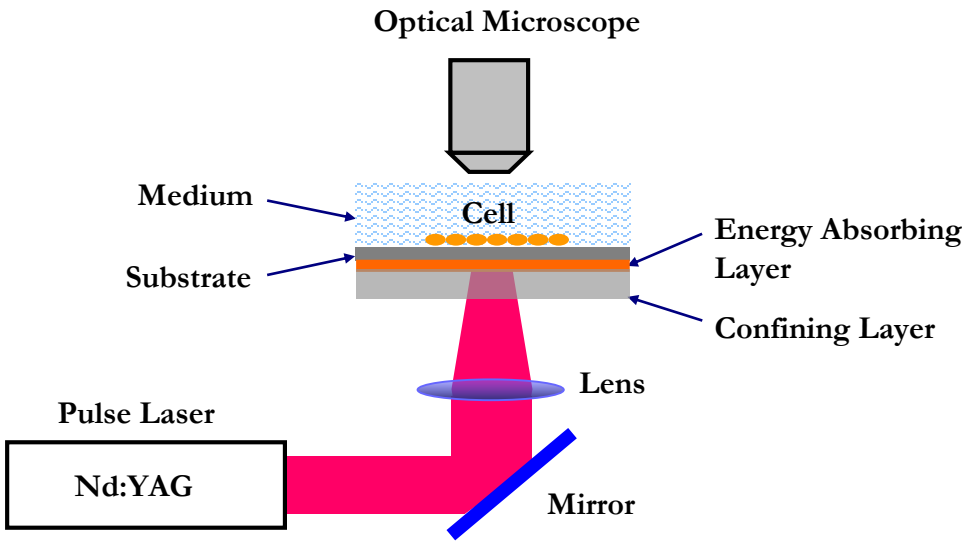

Figure 5.1: Schematic of the cell-substrate adhesion measurement using laser-induced stress waves[115].

Recently we introduced an experimental technique using laser-induced stress waves to study cell-substrate adhesion [115]. In the experiment, illustrated in Figure 5.1, the cells of interest are seeded on the top surface of a planar Si substrate. On the bottom surface of the Si substrate, an energy absorbing layer (aluminum) and a confining layer (waterglass) were deposited sequentially. A Gaussian laser pulse of nanoseconds duration with continuously adjustable energy from 0-300 mJ is incident from the bottom side of the substrate. A focal lens is used to focus the laser beam to a smaller size in order to increase the laser fluence. After passing through the transparent confining layer, most of the Nd:YAG laser pulse energy is deposited on the energy absorbing layer. Upon absorbing the laser energy, the sudden expansion and exfoliation of the absorbing layer generates a compressive stress wave which propagates towards the cells adhering to the top surface of the Si substrate. Due to the acoustic mismatch between the cells and the Si substrate, a significant amount of the compressive stress wave is expected to be reflected at the cell-substrate interface into a tensile wave while a smaller portion is transmitted into the cell which may be further reflected at the cell-medium interface. The

combined effect of the wave reflection and transmission results in a detachment force at the cell-substrate interface. The laser energy is increased until a large enough detachment force is generated to fail the cell-substrate interface. Comparing to the previous techniques such as micromanipulation method using AFM [134], the major advantage of the laser-induced stress wave technique is that it is a non-contact technique and the experiment lasts a very short time. Therefore, the cells do not have time to respond to the applied stress pulse and the true adhesion between the cell and substrate can be measured in an un-predisturbed manner. While the reported work has demonstrated the feasibility of the technique [115], due to the ultra-short time involved in the experiment it was not clear how this stress wave pulse led to the detachment of the cell from the substrate. In order to study the detachment mechanism, transient dynamic finite element analysis (FEA) is performed and reported here.

While numerical methods are convenient for studying dynamic problems at small spatial (μm) and temporal scales (ns), appropriate physical models and material properties must be chosen in order for the simulation to be relevant to the physical processes. Previous work on this topic includes the cell-substrate modeling by McGarry et al. who simulated adherent cell response to cyclic substrate deformation [140, 141] by utilizing a cohesive zone formulation for the cell-substrate interfacial behavior and cell properties obtained experimentally by Sato et al. [142]. McGarry et al. investigated the cell detachment based on the number of cycles of substrate deformation and observed that cell detachment occurs from the development of a tensile strain at the leading contact edge between the cell and the substrate.

For mechanical models of cells there are many possible choices. From the continuum mechanics approach to mechanical cell properties there are two classes of models: cortical shell-liquid core models and solid models. The cortical shell-liquid core models, also known as liquid drop models,

were first developed by Yeung and Evans [143] to account for the rheology of cells during micropipette aspiration. In these models there are different treatments for the liquid behavior such as a Newtonian liquid, compound Newtonian liquid, shear thinning liquid, and Maxwell liquid. The Newtonian liquid drop model was developed to simulate the flow of liquid like cells into the micropipette [144]. The interior of the cell is treated as a Newtonian fluid while the cortex is treated as a viscous fluid layer in static tension. The compound Newtonian liquid drop model was developed to account for different degrees of density found within the cytoplasm [145, 146]. It is similar to the Newtonian liquid drop model, but contains an additional layer that is also under static tension which separates the two interior fluids of the cytoplasm. The shear thinning liquid drop model was motivated by the observation that the apparent viscosity of the cytoplasm decreased with increasing aspiration pressure by a power law relationship [147]. This power law relationship was incorporated into the cortical shell-liquid core model, which consisted of the cytoplasm being modeled as a power-law fluid with a cortical layer under static tension. The Newtonian and Newtonian-like models are able to account for the large deformation seen during micropipette aspiration, but to account for the small deformations seen during the initial entry into the pipette the Maxwell liquid drop model was developed [148]. The Maxwell liquid drop model uses a Maxwell fluid to model the cytoplasm and similarly a cortical layer under static tension. The Maxwell fluid is able to account for the initial elastic behavior of the cell as it enters the micropipette. Solid models include linear elastic, linear viscoelastic, and power-law structural damping. The power-law structural dampening model was developed to describe the dynamic behavior of cells [149, 150]. Most of the models treat the cell as being a single phase with the exception of biphasic model which delineates the solid and fluid components of the cell cytoplasm into two phases and treats them separately [151].

While a complete review of cell modeling can be found in literature [152], the linear elastic and linear viscoelastic models are used for the cells in this study as the majority of cell properties reported in literature use these models. Different experimental techniques all report cell properties that fall into a narrow range. Details of the linear elastic and viscoelastic models are provided in next section.

5.2. Simulation Scheme

In order to simulate the cell detachment process under laser-induced stress wave loading, an axisymmetric model, as shown in Figure 5.2, is used in the current work. The model consists of a cell deposited on a substrate. The cell is composed of a cell membrane, cytoplasm, and nucleus. The adhesion is treated by means of an interfacial layer between the cell and the substrate. It is assumed that the interface thickness (typically ~25 nm) is small compared with the thickness of the cell (typically ~4 μm) such that the stress experienced by elements within the thin interfacial layer can be assumed as the stress directly applied on the lower surface of the cell, i.e., interfacial stress. A similar numerical scheme was used by Liang et al. for the simulation of laser-induced thin film delamination [153], where a small interfacial layer was used to model the failure process of a thin film-substrate interface. The results of Liang et al. correlate well with both analytical predictions and experimental observations. Due to the large mismatch in material properties between the cell and substrate, and that wave propagation in elastic solids is well understood, the elastic response of the substrate can be ignored in the current work. Instead the elastic substrate with an input Gaussian pressure wave is replaced by a rigid substrate with a prescribed displacement resulted from the equivalent Gaussian pressure along the z-axis. The analytical solution for the displacement in an elastic solid induced by a Gaussian stress wave is well studied by Wang [108, 123] and it is essentially a Gaussian error function. As such, the prescribed rigid body displacement of the substrate takes the form of :

$$u_{sub}(t;d,T) = d \cdot \left\{ 1 + erf\left(\frac{\sqrt{2}(t-2T)}{T} \right) \right\} \tag{17}$$

where u_{sub} is the displacement, d is half of the total substrate displacement, and T is the FWHM (full-width-half-maximum) of the laser pulse. The displacement is shifted such that the initial displacement is ~zero at time zero. T is around 5 ns as used in the previous experiments [115] and the displacement is of the order of several hundred nanometers.

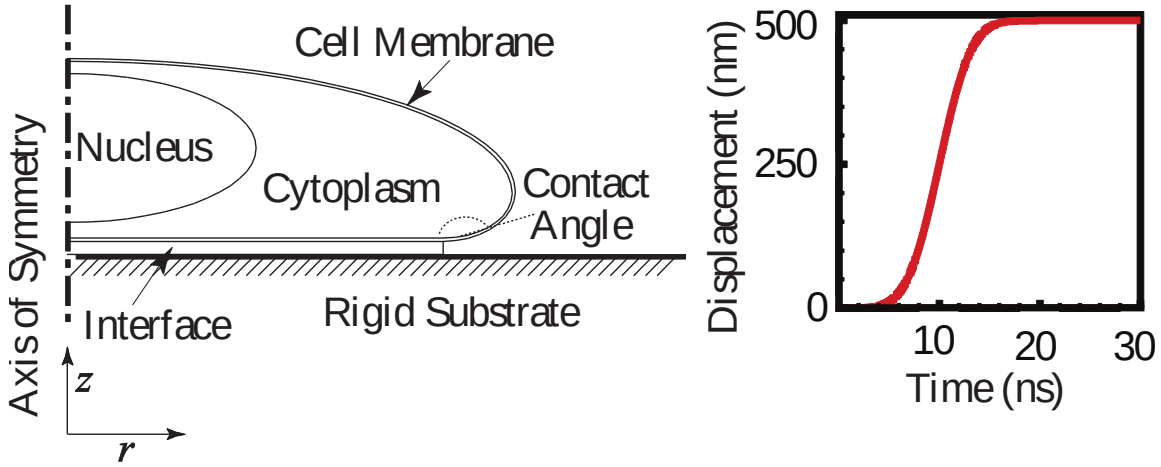

Figure 5.2: Schematic of the cell configuration used in the simulation and the rigid substrate prescribed displacement.

For this work two model geometries were considered. The first geometry represents the case when an adherent cell first comes into contact with a substrate similar to what is illustrated in Figure 5.2. This geometry typically results in a contact angle greater than 90° and is henceforth referred to as the hydrophobic cell model. Once adherent cells are able to attach themselves to an anchoring material they tend to stretch to maximize the adhesion area. This results in a contact angle of 90° or smaller and creates the hydrophilic cell model. For both the hydrophobic and hydrophilic cell models, ellipses are used to create the cell surface. The hydrophobic cell consists of two ellipses, one creating the top surface while the other creating the lower surface that connects to the interfacial layer. Only one ellipse is needed to create the cell surface for the hydrophilic cell. The interfacial layer dimensions are

representative of what has been reported in literature for ligand-receptor bond length [154, 155]. The rigid substrate has a small thickness and a radius twice the width of the cell to ensure there is adequate area for contact between the cell and substrate. For the case of the hydrophilic cell model both continuous and discrete adhesion were considered to capture possible affects resulting from focal adhesion. The discrete interface was modeled with 5 discrete adhesion sites of equal width representing 70% of the continuous interface width.

Different material models are adopted for different components in the test sample assembly. The cell cytoplasm is modeled as either linear elastic or linear viscoelastic, with viscoelastic properties coming from the work by Sato et al. [142]. The cell nucleus is modeled with the same constitutive equation as the cytoplasm but its material properties are scaled to be four times stiffer [156]. The interfacial layer is modeled as linear viscoelastic with the same material properties as the linear viscoelastic cell model. The cell membrane is 6 nm thick and modeled as elastic. The constitutive equation for a linear elastic material is

$$\sigma_{ij} = \frac{E}{1+\nu}\left(\varepsilon_{ij} + \frac{\nu}{1-2\nu}\varepsilon_{kk}\delta_{ij}\right) \tag{18}$$

where σ_{ij} is the stress tensor, ε_{ij} is the strain tensor, E is the modulus of elasticity, ν is the Poisson's ratio, and δ_{ij} is the Kronecker's delta. The linear elastic model is characterized by two independent material properties; in this case the modulus of elasticity, E, and the Poisson's ratio, ν. Linear elastic models can be insufficient when applied to cells since the physical properties of cells are time-dependent. In order to capture the time-dependent nature of the cell mechanical response, the linear viscoelastic model (shown in Figure 5.3) proposed by Schmid et al. [157] is also used for the cell and

the interfacial layer. The three parameter viscoelastic model is a combination of the fundamental Maxwell and Kelvin-Voigt models and its constitutive equation is given by [157]

$$\sigma'_{ij} + \frac{\mu}{k_2}\dot{\sigma}'_{ij} = k_1\varepsilon'_{ij} + \mu\left(1+\frac{k_1}{k_2}\right)\dot{\varepsilon}'_{ij} \tag{19}$$

where k_1 and k_2 are elastic constants, μ is a viscous constant. The prime indicates the deviatoric stress and strain, defined by

$$\sigma_{ij}{}' = \sigma_{ij} - \frac{1}{3}\sigma_{kk}\delta_{ij} \text{ and } \varepsilon_{ij}{}' = \varepsilon_{ij} - \frac{1}{3}\varepsilon_{kk}\delta_{ij} \tag{20}$$

and the dot indicates the first derivative with respect to time.

Table 5.1 lists the material properties that were used for the simulations. While the chosen material properties may not be representative of all cells, this study is primarily focused on the mechanism of cell detachment under the applied stress waves. Material properties that lay in the same general range as those chosen generally result in the same detachment mechanism.

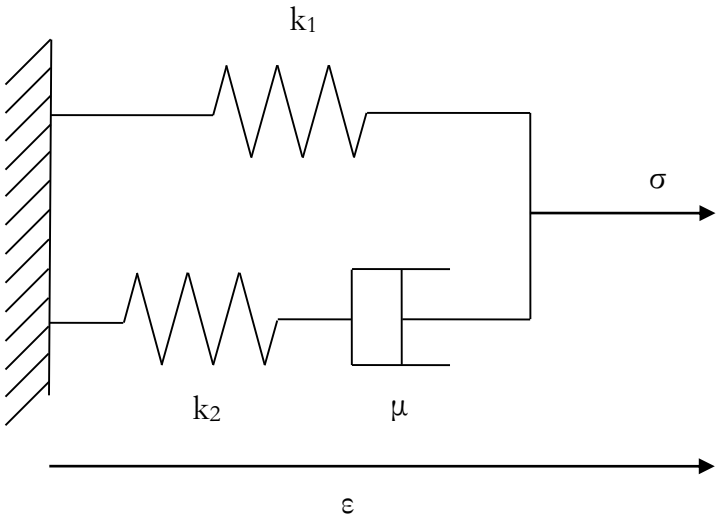

Figure 5.3: Model of 3-parameter viscoelastic solid.

Table 5.1: Material properties used in the simulation.

Component	Model	Parameter	Value		Source
Cell cytoplasm and Interface	Elastic	Modulus of elasticity E	100	KPa	[158]
		Poisson's ratio ν	0.49*		
		Density ρ	1000	kg/m^3	
	Viscoelastic	Elastic constant k_1	22.5	Pa	[142]
		Elastic constant k_2	37.5	Pa	
		Viscous constant μ	1.7x10^3	Pa s	
Cell Membrane	Elastic	Modulus of elasticity E	10	MPa	[158]
		Poisson's ratio ν	0.49*		
		Density ρ	1000	kg/m^3	

For this study the LS-DYNA transient dynamic finite element code was used. LS-DYNA has several failure criteria that can be used to simulate material failure. These include specifying a failure pressure, principal stress, equivalent stress, or threshold stress. Failure can also be specified by a principal strain or shear strain. For this study the failure specified by both principal stress and principal strain was chosen. Since the incoming stress is largely in the z-direction, the principal stress will be dominated by the planar input stress. The model is treated as axisymmetric with the substrate constrained from rotation and only allowed translation along the z-axis. For both the continuous and discrete interface geometries, the interfacial elements are specified with an adhesion strength ranging from 1-30 MPa, chosen to be sufficiently high to capture a broad range of mechanical response and possible adhesion strengths. If the stress exceeds this strength the element is specified to fail and erode away. In addition to failure by stress, failure by strain is also considered. The interfacial layer has a thickness of 25 nm. If an interfacial element experiences more than 80% of principal strain it is specified to fail and erode

away. The 80% was chosen because this amount of strain can result in an stretching of the adhesion protein bonding to 45 nm, which is longer than any proposed bonding mechanism [159]. Through the use of the failing interfacial elements, it is possible to investigate the mechanisms that lead to the detachment of the cell from the substrate.

In the numerical implementation of the linear elastic model the co-rotational rate of the deviatoric stress tensor is computed as [160]

$$\sigma_{ij}'^{\nabla^{n+1/2}} = 2G\dot{\varepsilon}_{ij}'^{n+1/2} \tag{21}$$

where $\sigma_{ij}'^{\nabla}$ is the co-rotational deviatoric stress rate and is defined by

$$\sigma_{ij}'^{\nabla} = \frac{d\sigma_{ij}'}{dt} a_i \otimes a_j \tag{22}$$

where a_i and a_j are principle directions that rotate with the elastic body, and G is the elastic shear modulus. The linear viscoelastic model implementation takes the form [160]

$$\sigma_{ij}' = 2\int_0^t \phi(t-\tau)\frac{\partial \varepsilon_{ij}'}{\partial \tau} d\tau \tag{23}$$

where ϕ is the shear relaxation modulus function and is given by

$$\phi(t) = G_\infty + (G_0 - G_\infty)e^{-\beta t} \tag{24}$$

where G_∞ is the long time shear modulus, also called the steady-state stiffness, which dominates the shear relaxation modulus as t grows, G_0 is the short time shear modulus whose contribution is only significant for small t, and β is the inverse of the characteristic creep time τ given by $\beta = 1/\tau$, where $\tau = \frac{\mu(k_1 + k_2)}{k_1 k_2}$ and is calculated to be 121 seconds based on the properties in Table 5.1. Equation (23) represents the heredity integral formulation of the constitutive equation with $\phi(t-\tau)$ being the kernel

function of the integral and describes the strain history. Here, for both the linear elastic and linear viscoelastic material models, elastic bulk material behavior is assumed; hence the mean hydrostatic stress is given by:

$$p = -K \ln \frac{V_i}{V_0}, \tag{25}$$

where p is the pressure, K is the bulk modulus, and V_i over V_0 is the ratio of the current to initial volume. Total stress is given by summing the deviatoric and hydrostatic stress.

To generate the mesh, a Planar Straight Line Graph (PSLG) representation of the model geometry consisting of points and segments for the substrate, interface, and cell components was first created which was subsequently input into a two-dimensional quality mesh generator and Delaunay triangulator developed by Jonathan Shewchuk – Triangle [161]. Triangle has many features that make it well suited for mesh generation in finite element applications. Most notable features are user designated minimum angle in any triangle and user designated maximum area. The specification of a minimum angle ensures the creation of triangles with aspect ratios close to unity, which is important for numerical integration over the element. The specification of a maximum area for a triangle ensures a high mesh density for solution convergence. The mesh generation is also unstructured, allowing for a high element density in the area of interest, the interface, and a low element density away from the interface.

5.3. Simulation Results

5.3.1. Interfacial Stress

Stress at the interface between the cell and substrate is generated by the acceleration of the substrate, which, in addition to compressing the interface, creates the tendency of the cell to flatten and spread. The effect of the spreading is not uniform across the interface and it is most pronounced at the radial edge of the cell. At the early stages of substrate acceleration the stress state in this region is mixed mode while the interface near the axisymmetric axis is largely in compression, as seen in Figure 5.4 (a) by the uniform height of the principal strain vectors along the interface until the edge, where the magnitude increases rapidly. In the uniform area the principal strain vectors are aligned with the z-axis, indicating the strain is in the z-direction. This is not the case at the radial edge where the principal strain vectors are rotated, indicating the strain response being dominated by shear.

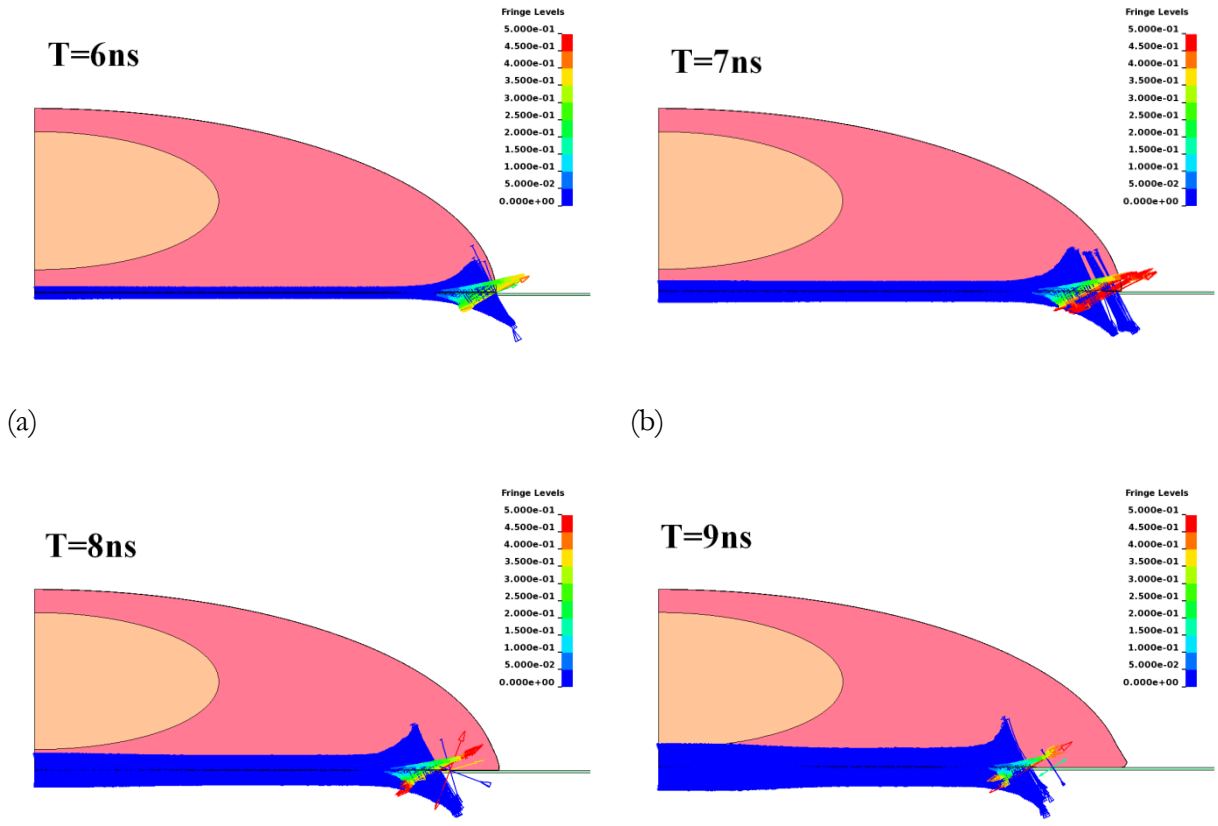

(a) (b)

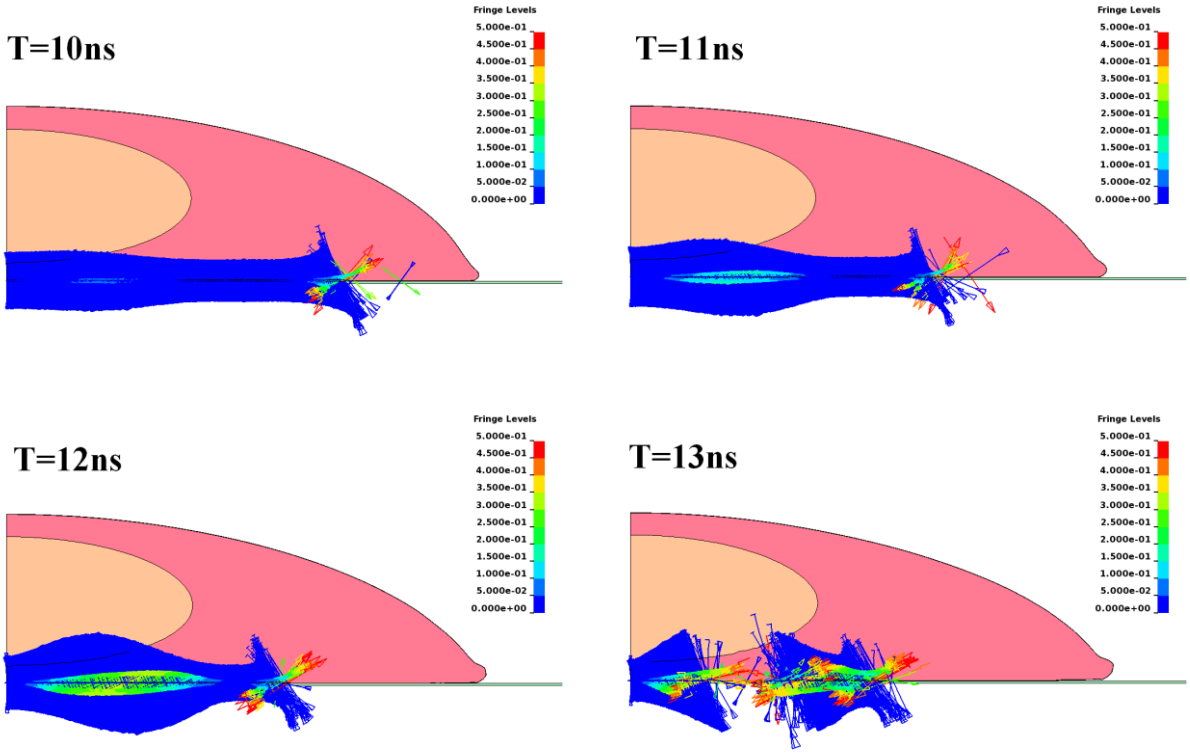

Figure 5.4: Principal strain vectors of the interface layer for hydrophilic cell with continuous interface at 6-13 ns (a-h) showing the interface failure progression. Snapshots (f-h) show the contribution of the cell nucleus to the interface loading, nucleating a new failure site before the failure propagating for the edge of the cell arrives.

Although all cell parts combined determine the overall mechanical behavior of a cell, it is possible to see specific effects that arise from individual components. The cell membrane, modeled as a moderately stiff elastic material, provides a small amount of rigidity to the cell periphery. The viscoelastic cytoplasm is extremely soft in its deviatoric response. The cell membrane ensures that there can be no severe deformations, without which slivered elements could form in the cytoplasm. Elements that become extremely distorted can be inaccurate and lead to severe errors such as complex wave speeds.

Possibly the most interesting effect is the interaction between the propagating stress wave and the interface of the cytoplasm and the nucleus. When the propagating stress reaches the cytoplasm-

nucleus interface there is both transmission and reflection due to the nucleus being about four times stiffer than the cytoplasm. Along the curved surface of the nucleus this results in mixed mode loading being reflected at the cytoplasm-nucleus interface and propagating back toward the adhesion layer. This reflected mixed mode stress reaches the interface before the interface failure propagating from the radial edge, as seen in Figure 5.4 (f-h). Effectively, a new interface failure site is nucleated from the mixed mode loading and propagates in both directions, leading to much faster interface failure. This is seen in Figure 5.5 around 11 ns, when the slope of the interface erosion suddenly increases, indicating faster interface failure.

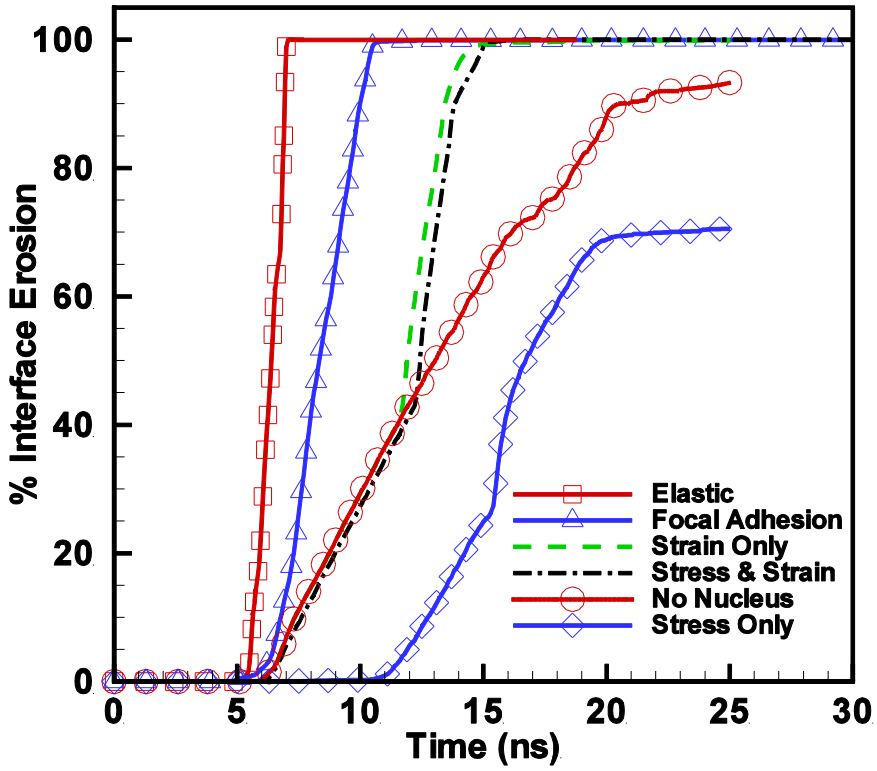

Figure 5.5: Interface erosion evolution for several different failure criteria for the spread cell model. The fastest failure happens during the focal adhesion (stress and strain failure criteria) model (red line with square is elastic model with focal adhesion, otherwise model is viscoelastic), followed by models with stress and strain criteria, strain only criterion, and a model with no nucleus. The slowest failure was from stress only criterion and also failed to completely erode all interface elements.

5.3.2. Cell-Substrate Decohesion Behavior

Figure 5.5 shows the interface failure evolution from various modeling scenarios. From left to right, the quickest failure is from the focal adhesion model (elastic then viscoelastic), followed by a model in which only strain is considered for the adhesion layer failure. Next is a simulation where stress and strain of the interfacial layer are considered. In order to elucidate the role the nucleus plays during interfacial failure the strain only failure model was run without the nucleus. The slowest failure simulation, and the only model with incomplete interface failure, was when only stress in the adhesion layer was considered for failure. Figure 5.5 shows that there is a broad range of possible interface erosion evolutions, but there are several common trends. In all cases interface failure is initiated at the radial edge of the cell and propagates toward the center.

Several snapshots showing the progression of interface failure are shown in Figure 5.4. The acceleration of the cell from the prescribed substrate displacement leads to the cell's tendency to elongate and stretch in the radial direction in addition to compressing the interface. The substrate will only move in the z-direction with no motion in the radial direction. As a result there is a relative motion between the cell and the substrate in the radial direction. This relative motion creates large shear strains in the interface and is most exaggerated at the edge of the cell. As seen in Figure 5.4 (a) the strain builds up at the far radial edge of the cell while the rest of the interface is in nearly uniform strain from compression. When the strain reaches the strain failure criterion it begins propagating across the interface toward the center of the cell (b-f). The propagation is steady for most of the interface, until the effects from the nucleus are seen and described above on interfacial stress above. This behavior is seen for all the models except in the stress only failure criterion model, where there

is slow and incomplete interfacial failure. This discrepancy arises from the interface being very soft in its deviatoric response. The propagation of stress/strain along the interface is mixed mode, but with small deviatoric stresses compared to the bulk elastic response (orders of magnitude difference). Large shear strains are realized before large principal stresses since the shear strain is from the deviatoric response and the principal stress is largely from the bulk elastic response. Without interfacial failure from strain, large stresses must develop in the interface, but only stresses from the bulk elastic response are able to generate sufficient loading. This ends up being a slower and less efficient process and also borders on being physically unreasonable since shear strains in the 1000's of percent are realized before stress failure.

5.3.2.1. Elastic vs. Viscoelastic

For our simulations both elastic and viscoelastic material models were considered for the cell and interface. This helped to determine whether or not the proposed detachment mechanism was sensitive to the choice of material model. The cell's inherent time-dependent behavior could feasibly affect the detachment mechanism observed, making it different from the elastic material response. However, the viscoelastic material properties used in this study make this unlikely since the characteristic creep time τ is of the order of 100's of seconds, which is too long in comparison to the nanosecond characteristic time of the pressure pulse. Indeed, overall simulated material behavior was similar for the elastic and viscoelastic models. For both material models the interfacial failure is dominated by strain of the interfacial elements with the largest strain component for both models being shear. Looking at the curves for elastic versus viscoelastic in Figure 5.5, the elastic model has a steeper slope and fails before the viscoelastic model. This is attributed to the elastic model being more compressible than the viscoelastic model since elastic bulk behavior is used for both models and the bulk modulus

is calculated based on the elastic modulus and Poisson's ratio for the elastic material model while it is a specified material parameter for the viscoelastic model. Even with a Poisson's ratio of 0.49 the bulk modulus for the elastic model is much smaller than that specified for the viscoelastic model (the bulk modulus of water). This difference is small since the behavior is very similar and is characterized by a nearly constant rate of interface failure from initiation to completion.

5.3.2.2. Effect of Hydrophobicity

In addition to investigating the effect of material models on the detachment mechanism, the evolution of cell geometry for a contact angle representing a hydrophobic cell to a contact angle representing a hydrophilic cell was also investigated.

Most adherent cells change morphology when they are in contact with a substrate. Initially adherent cells display a contact angle appearing to be hydrophobic, as seen in Figure 5.2. Then they tend to extend and flatten out on the substrate. The change in morphology affects the initiation of failure of the interfacial elements and its time evolution, but all the same mechanisms appear. Figure 5.6 compares the interface erosion evolution between the hydrophobic and hydrophilic cell models. For the hydrophobic cell initiation of interface failure is inhibited by the overhung area of the cell coming into contact with the substrate, preventing strain buildup at the edge of the interface. While strain is building up to its failure level at the edge stress is being transmitted into the cell and, consequently, being reflected at the cell-nucleus interface. Since upon arrival of the nucleus-cytoplasm reflected stress less of the interface has failed compared to the hydrophilic model, a larger area is affected. The larger area achieves a more uniform strain state, as seen in the 12 and 13 ns insets in Figure 5.6 for the

hydrophobic cell (right), compared to the hydrophilic cell at 12 ns (left). Nearly uniform strain in the interface leads to nearly simultaneous failure at a rate slightly quicker than for the hydrophilic cell.

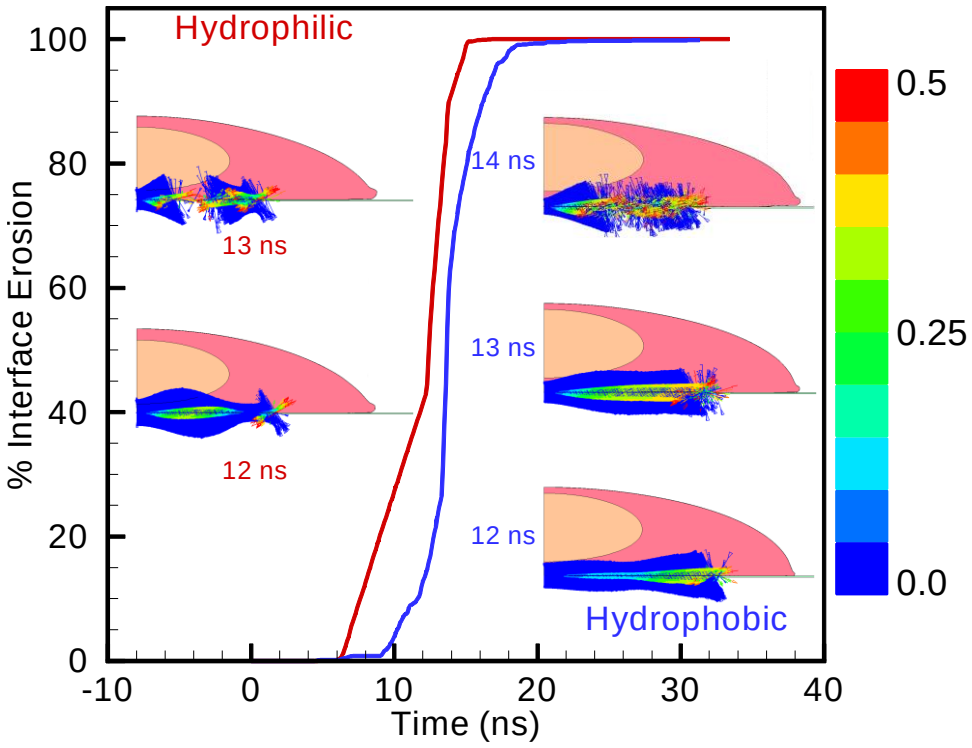

Figure 5.6: Comparison of the interface evolution for the hydrophilic (left) and hydrophobic (right) cell geometries. Insets show principal strain vectors for their respective models.

5.3.2.3. Effect of Focal Adhesion

Spread cells tend to form focal adhesions. Here we simplify the biological case to 5 focal adhesion sites of uniform width which occupies 70% of the total interface length. Figure 5.7 (a-f) shows the interface failure of a focal adhesion site at the edge of the cell. The effect of focal adhesion is a quicker interface failure. Comparison of the continuous and discrete interfaces shows that the discrete interface begins failing faster and progresses at a nearly constant rate. Earlier failure of the focal adhesion simulation is due to stress concentration on the inside edge of the focal adhesion sites, leading to failure before the far radial edge seen in Figure 5.7 (c). The rate is very similar to that

exhibited in the second stage of interface failure in the continuous model and understood by the same mechanism, except for the case of the focal adhesion interface there is no delay for the nucleation of new failure sites; they are inherent in the discrete interface model geometry. This can be seen in Figure 5.7 (d-f) where interface failure has now been initiated at both side of the focal adhesion and propagate in both directions simultaneously. This process of failure propagating in both directions happens at all the focal adhesion sites and explains the rate difference of the continuous versus discrete interface models.

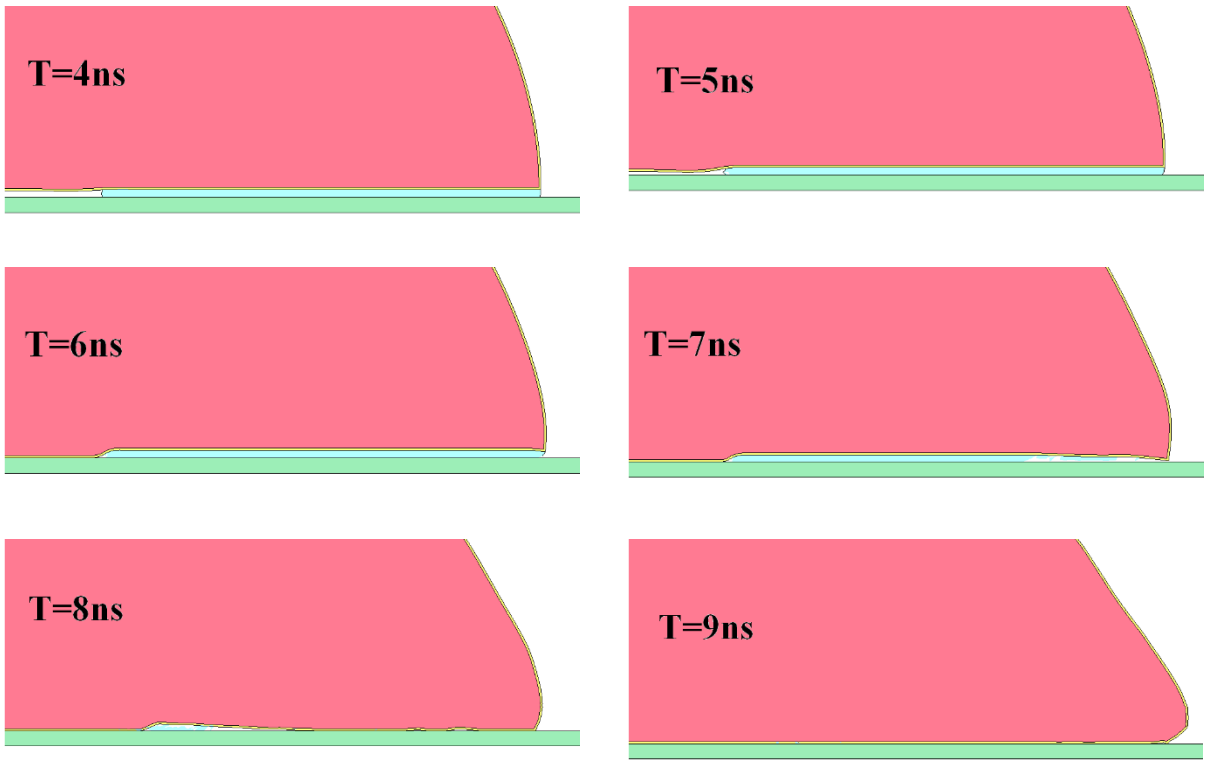

Figure 5.7: Snapshots at 4-9 ns of the leading edge focal adhesion site during interface failure. From (a-d) we see the cell come into contact with the substrate. This creates a stress concentration on the inside edge of this focal adhesion site, leading to failure before the far radial edge. This explains why the focal adhesion simulation begins failure before the continuous interface. (e-f) show that after failure initiation the focal adhesion site is quickly eroded from the simultaneous failure propagation in both directions.

5.4. Discussion

The validity of any model depends greatly on its assumptions, which dictates what behavior is possible. The linear elastic and viscoelastic models used for these simulations result in very similar cell detachment process due to the characteristic time of the viscoelastic model being many orders of magnitude greater than the applied loading and the assumption of bulk elastic behavior for both models. The cell is also treated as nearly incompressible by using a Poisson's ratio close to 0.5 for the elastic model and using the bulk modulus of water for the viscoelastic model. Thus both models simulate nearly incompressible elastic pressure, and both models have very similar interface failure. Another assumption made for simplifying the model was treating the substrate as rigid with a prescribed displacement resulting from the solution to an elastic wave with a Gaussian profile. This is justified by the large mismatch in material properties between the silicon substrate and the cell. While this is computationally more convenient and efficient, it precludes interaction between the cell and substrate. However, the interface stress profile with no failure criteria is similar to the analytically derived interface stress for the case of an elastic thin film on a substrate, so the interfacial behavior is accurate.

A notable exclusion from this model is the contribution of the cytoskeleton. The cytoskeleton is a key mechanical component of the cell. Recently McGarry et al. [162] used the cell contractility model developed by Deshpande et al. [163] to simulate the force cells exert onto an array of micro-posts. Deshpande et al.'s model couples the polymerization of actin to stress fiber formation and the stress fiber tension. McGarry et al. are able to accurately predict the contractility response for several cell types, including the observed distribution of actin within the cell and the observed scaling of force with the number of posts. When considered an active material, the cytoskeleton is largely responsible for mechanical changes observed during cell growth, division, and movement. The ability to react and interact with the cell environment depends largely on the polymerization rates for the cytoskeletal

substructures formed from actin filaments, microtubules, and intermediate filaments. The polymerization rate for each of these filaments is much slower than the applied displacement. Thus on the time scale of our experiment and simulation the cell is passive. A consequence of this modeling approach is that the strains predicted may be larger than those experienced by the cell in areas with a high concentration of filaments.

It is worth noting that the continuous and discrete interfaces are investigated for the same range of interfacial strengths, despite having different contact areas. This approach is taken since we do not know exactly what the interfacial strength is and we are interested in any changes in the mechanism of cell detachment that might result at different strengths. Experimentally, adhesion strength is observed to increase until it reaches a steady state level. This can be understood in terms of the amount of integrin binding, which matures over time and correlates well with adhesion strength [164]. So while the amount of contact area is decreasing from the continuous interface to the discrete interface, the strength per unit length increases. In our simulations we observed that the prescribed interfacial strength did not materially affect the detachment mechanism or time evolution. This is reasonable since strain in the interface dominates the failure, and where stress from failure contributes, the time difference between stress levels is very short.

As was seen experimentally by Hu et al. [115] cells are effectively detached by laser-induced stress waves. Our model explains that the cell detachment is from the large strains experienced in the interface from the cell's tendency to spread out during the rapid movement of the substrate. The interface is modeled as a solid which may differ in some respects from the actual behavior of the proteins in the interface. The mechanics of the bonding and debonding of the proteins are complicated

and follow different kinetic pathways under different conditions [159], which result from slip bonds or catch bonds. Slip bond failure is characterized by the failure rate being proportional to the applied force, whereas catch bonds can strengthen with increasing force. Slip bond failure is analogous to constant adhesion strength, but catch bond failure would make the adhesion strength a function of the loading history. Consequently, if interface detachment was dominated by catch bond failure, it would take longer for the shear strains in the interface to develop to the failure level. Since our interface is modeled as a continuum, the failure of the protein bonding is only being captured on a much larger scale. Nevertheless, the interface strains predicted by the model are sufficiently large that bond failure would likely occur for a variety of adhesion proteins and bonding mechanisms (interface strain failure exceeds 100% without a strain failure criterion applied). Variation from the experiment to the simulation is certain, but we are confident in the overall interface failure mechanism and evolution predicted by the simulation.

5.5. Conclusions

The detachment process of an adherent cell from a substrate under laser-induced stress wave loading was simulated using a transient finite element method and an axisymmetric cell-substrate configuration. An interfacial layer of 25 nm thickness was added between the cell and substrate to capture the stress state at the cell-substrate interface. The cell and the interfacial layer were modeled as both linear elastic and viscoelastic using the properties obtained from literature. An error function profile rigid body displacement with a 5 ns period was used to simulate the laser-induced stress wave pulse in the experiment. Both hydrophobic and hydrophilic cell geometries were used to simulate the cells in an early and fully developed stage, respectively. The major conclusions are:

1) The cell detachment under laser-induced stress wave loading is due to a complex stress/strain state resulted from the cell geometry and the applied loading.
2) The principal detachment mechanism is the strain driven failure resulting from the cell's tendency to flatten and elongate along the substrate.
3) The detachment behavior is similar for both elastic and viscoelastic material models for the cell. This is due to the characteristic creep time of the viscoelastic material model being many orders of magnitude longer than the nanosecond characteristic time of the applied stress wave pulse, leading to non time-dependent behavior of the viscoelastic material model.
4) The evolution of cell geometry from hydrophobic to hydrophilic results in the same detachment process.

Together with the previously reported experimental development, this work confirmed that laser-induced stress wave technique is a feasible method for measuring the adhesion between biological cells and inorganic substrates. Due to the non-contact loading and the orders of magnitude difference between the duration of the laser-induced stress wave pulse and the characteristic response time of the cell, the cells being tested would have no time to react to the applied loading thus a time independent, intrinsic adhesion between the cell and substrate can be measured.

Chapter 6. Response of Nanoporous Zeolite to Laser-induced Loading

6.1. Zeolite Background

Zeolites form a class of nanoporous and crystalline aluminosilicates. They are naturally occurring minerals, but synthetic zeolites are also highly desired. This is due to their nanoscale porosity allowing unique applications as molecular sieves and ion-exchangers. The crystalline pore structure allows simultaneous high porosity and mechanical stability. Synthesizing zeolites allows fine control of the aluminum to silicon ratio, which dictates the materials ion-exchange capability, influencing the materials performance and allowing tuning for a desired application. Low silica zeolites, whose aluminum to silicon ratio is ~1 find widespread application as ion-exchangers. It is also possible to synthesize zeolites without aluminum, known as pure silica zeolites. These have found recent interest as a next generation low dielectric constant material for the semiconductor industry due to the high porosity. Zeolites have also been investigated for applications as environmentally friendly wear and corrosion resistant coatings [165]. Wear resistance is provided by their high mechanical strength and resilience, which is comparable to that of chromium. Corrosion resistance is provided by high and pure silica zeolites, which are only attacked by hydrofluoric acid [166].

In general, porous materials provide several responses which make them good candidate materials for impact and shock. Due to the presence of voids and pores in the material they undergo compaction and densification during compression. While the strength of the porous material may be lower than that of its bulk counterpart, energy must be used for the initial collapsing of the pores. This process of reducing the material from its large specific volume to its standard volume involves not only

overcoming elastic and plastic response, but also friction and other dissipative mechanisms. Additionally, the porous nature of the material allows wave interactions, such as transverse relief, to operate at a small scale and dissipate additional energy. Thus compaction of porous materials is highly dissipative and even modest porosity can achieve significant stress attenuation. Dynamic compaction may also be localized to the area of applied loading, with little effect on the surrounding material. Counterintuitively, the compression of a porous material to a given volume requires more energy than compressing the bulk material to the same volume. This is due to the compression of the porous material being accompanied by larger thermal energy, and hence thermal stress, than experienced by the bulk material [167]. The spallation behavior of porous materials is sensitive to the compressive plastic strain experienced during the initial loading as well as ductile or brittle response.

6.2. Sample Preparation, Zeolite Growth, and Structure Confirmation

Substrates were chosen for this study based on their response to laser loading and their applicability as materials whose performance would be improved by being coated with zeolite. 4130 chromoly steel and 6061 aluminum alloy find wide use as structural materials, but require surface coating in many applications to overcome a specific deficiency. 4130 steel has poor corrosion resistance, while 6061 aluminum alloy has poor hardness and wear resistance. The substrates were cut into thin disks from bulk bar stock. Grinding, lapping, and polishing were performed on both surfaces to provide an ideal surface for both the zeolite film growth, as well as to accommodate our optical interferometer, which relies on an optically flat, specular reflective surface.

The zeolite studied is ZSM-5, an MFI framework zeolite first reported by Kokotailo et al. [168]. The ZSM-5 framework consists of two interpenetrating porous networks. A straight, nearly circular channel running parallel to [010] with dimensions of 5.4 X 5.6 Å, and an elliptical zigzag channel along [100] with dimensions of 5.1 X 5.4 Å. ZSM-5 are orthorhombic crystals and belong to space group No. 62, Pnma, with cell parameters of $a = 20.07$, $b = 19.92$, and $c = 13.42$ Å [169]. Zeolite film growth is achieved by hydrothermal deposition and follows the procedure of Lew et al. [170]. A solution was prepared with aluminum powder, tetrapropylammonium hydroxide (TPAOH), tetraethylorthosilicate (TEOS), and sodium hydroxide (NaOH) in de-ionized water with a molar composition of 0.16TPAOH:0.64NAOH:TEOS:92H_2O:0.0018Al. The initial step in the solution synthesis procedure is mixing 0.0104 g Al power, 100 g de-ionized water, and 5.36 g NaOH pellets for 30 minutes at 400 RPM. 17.03 g TPAOH is then added and stirred for an additional 15 minutes. Subsequently 236 g of de-ionized water is added and stirred for 15 minutes. Final solution synthesis step is the dropwise addition of 43.6 g TEOS while stirring. Solution is aged for 24 hours while stirred at 800 RPM. After ageing the solution is placed in a Teflon lined autoclave, in which the 4130 steel of 6061 aluminum alloy thin disk substrates have been suspended by copper wire. After ensuring the substrates are fully immersed with adequate separation from one another, the autoclave is sealed and placed in an oven at 175 °C for 24 hours, after which film growth rates drops. In order to achieve the thickness of films needed for this study, the hydrothermal synthesis process is repeated as needed, using a fresh solution for each 24 hour growth stage.

SEM imaging of the surface of the as synthesized zeolite film was performed to examine the surface and crystal morphology. Figure 6.1 (a) is a low magnification micrograph showing island-like surface features which are dominant above 10 μm length scale. Surface profiling of the as synthesized surface

is shown in Figure 6.1 (b), with a measured RMS surface roughness of 4.5 μm. Figure 6.1 (c) shows the high degree of intergrowth and twinning with no preferred orientation, a trademark morphology for this specific zeolite and synthesis procedure, which was optimized to be a thin film membrane coating. Figure 6.1 (d) shows individual crystals ranging in size from 5-20 μm, which were used to measure the length-to-width ratio of 3.5. This ratio is consistent with our growth temperature of 175 °C. For ZSM-5 the individual crystal size is limited by the Al atom concentration, since the nucleation rate is proportional to the Al^{3+} concentration [171].

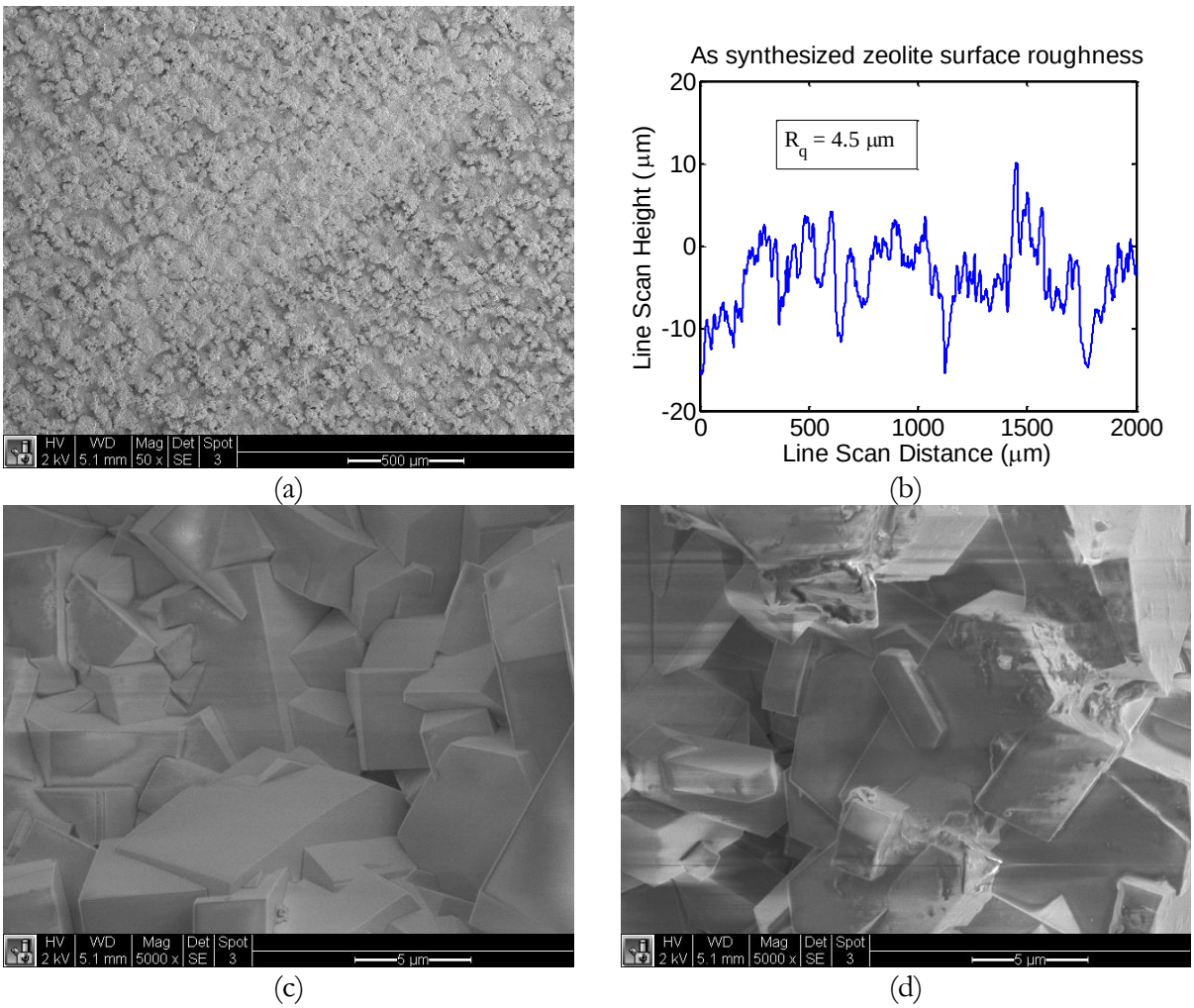

Figure 6.1: SEM images of the as synthesized zeolite surface morphology (a), (c-d), and profile of surface roughness (b).

X-ray diffraction (XRD) was used to confirm the crystal structure by comparing measured XRD data with that of the known zeolite ZSM-5 structure [172]. Quantitative XRD was obtained by Rietveld refinement [173, 174] using the MAUD [175, 176] software. Reference data comes from the Database of Zeolite Structures [177], with the ZSM-5 XRD data originating from van Koningsveld et al. [172]. Overall good agreement between the measured XRD data and the Rietveld refinement is observed, with corresponding refined cell parameters of $a = 20.03$, $b = 19.92$, and $c = 13.40$ Å.

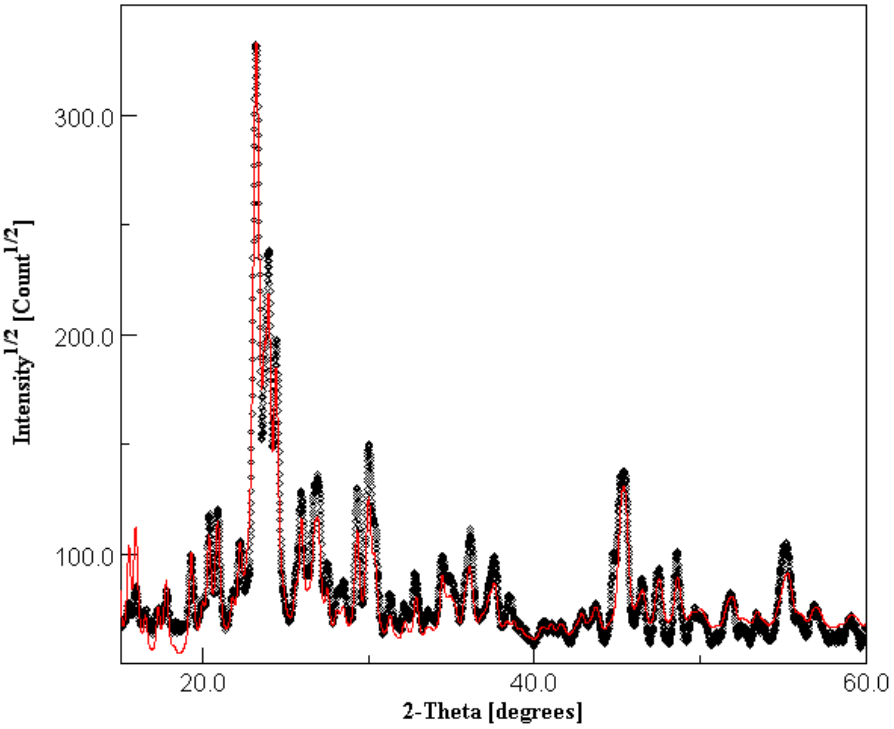

Figure 6.2: XRD measurements (black) and Rietveld refinement results (red), with corresponding cell parameters of *a*=20.03, *b*=19.92, and *c*=13.40 Å.

6.3. Experimental Setup

The experimental setup is that of the standard laser spallation experiment. Thin (several hundred microns) 4130 steel or 6061 aluminum alloy substrates were coated with 10's μm thick MFI zeolite

using the synthesis process described in section 6.2. For compression experiments the substrate is 4130 steel. The motivation for using a steel substrate is that the stress profile has a smooth Gaussian profile, with a width comparable to that of the 5 ns loading laser. In order to elicit only the compressive behavior of the ZSM-5, a fused silica window was used to minimize tensile stress which would normally develop from reflection at the free surface. The sample geometry is shown in Figure 6.3 (top). Fused silica is closely acoustically matched to ZSM-5, allowing the compressive stress to be efficiently transmitted into the substrate. The inner surface of the 1.5 mm fused silica window was coated with a thin 40 nm sputter deposited aluminum film, thus forming a back surface mirror needed for the interferometer. The back surface of the substrate, which faces the loading laser, has an energy absorbing layer (400 nm Al) as well as a spin coated waterglass confining layer. Spallation experiments were also conducted, with 6061 aluminum alloy as the substrate material. The sample geometry is shown in Figure 6.3 (bottom). 6061 aluminum alloy for the substrate was chosen due to its close acoustic match to the zeolite substrate, allowing both high stress generation and efficient coupling to the zeolite. A downside of the 6061 aluminum alloy substrate is the large distortion of the stress profile due to plasticity. This does not hinder the measurement of the spallation strength, though, since spallation creates unique signal features, allowing property extraction even in the presence of wave distortion from plasticity. Since the aim of these experiments is spallation, the laser-induced stress wave is allowed to reflect at the zeolite free surface into a tensile wave. Actual tension in the substrate is only achieved once the reflected tensile wave meets the unloading portion of the incoming compressive stress. If the tensile stress generated from the superposition of the free surface reflected wave and the compressive unloading wave exceeds the dynamic tensile strength of the zeolite, the spallation strength will be measured. The side of the sample facing the 5 ns Nd:YAG loading laser is coated with the typical 400 nm energy absorbing layer and 10 μm spin coated waterglass. For the spallation experiment it is important that the confining layer is thin enough to ensure that the

unloading wave intersects with the free surface reflected tensile wave within the zeolite thickness and away from the 6061 aluminum alloy-zeolite interface, thus ensuring the measured spallation strength is that of the bulk zeolite, and not influenced by the interface.

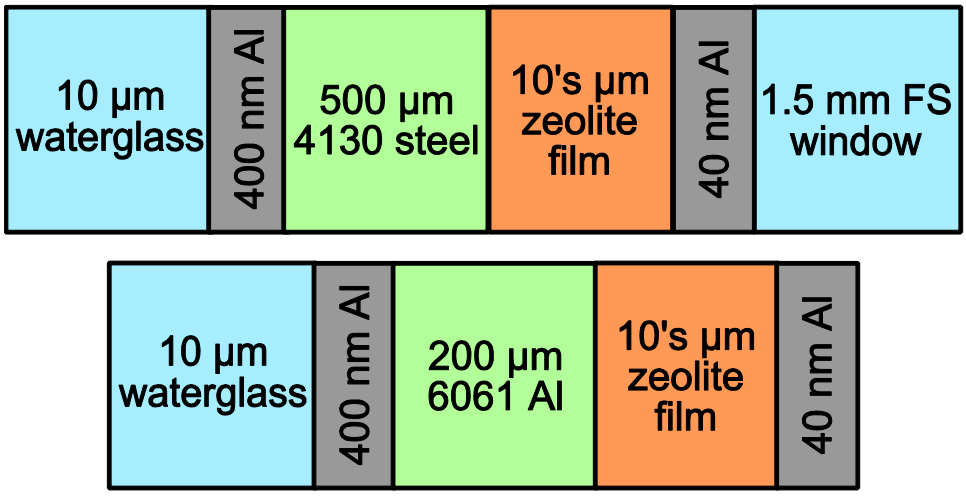

Figure 6.3: Zeolite sample geometry for compression (top) and spallation (bottom) experiments. Compression: 4130 steel substrate was coated with MFI zeolite films of 10's µm thickness. Standard Al energy absorbing layer and spin coated waterglass confining layer was used to augment and control stress generation. 1.5 mm fused silica was used as a windowing material, with the inner surface coated with a thin aluminum reflective film. Tension: thick zeolite films was grown on thin 6061 aluminum alloy substrate. The zeolite will be coated with a thin aluminum reflective film.

6.4. Compression Experiment with Thick Zeolite Films

Compression experiments were carried out for several 4130 steel substrate samples, with and without zeolite coatings. The principal goal was to measure the wave profile for coated and uncoated samples to determine if there was any distortion to the stress wave. Figure 6.4 shows typical interferometer signal (top) and stress history (bottom) for a 560 µm thick 4130 steel bare substrate (left) and a substrate with the same thickness and a 20 µm zeolite coating (right). Both profiles are Gaussian with time constants of 6.1 ns for the 4130 and 6.3 ns for zeolite. Peak stress achieved in the uncoated substrate is 1.5 GPa, while that of the coating is 400 MPa.

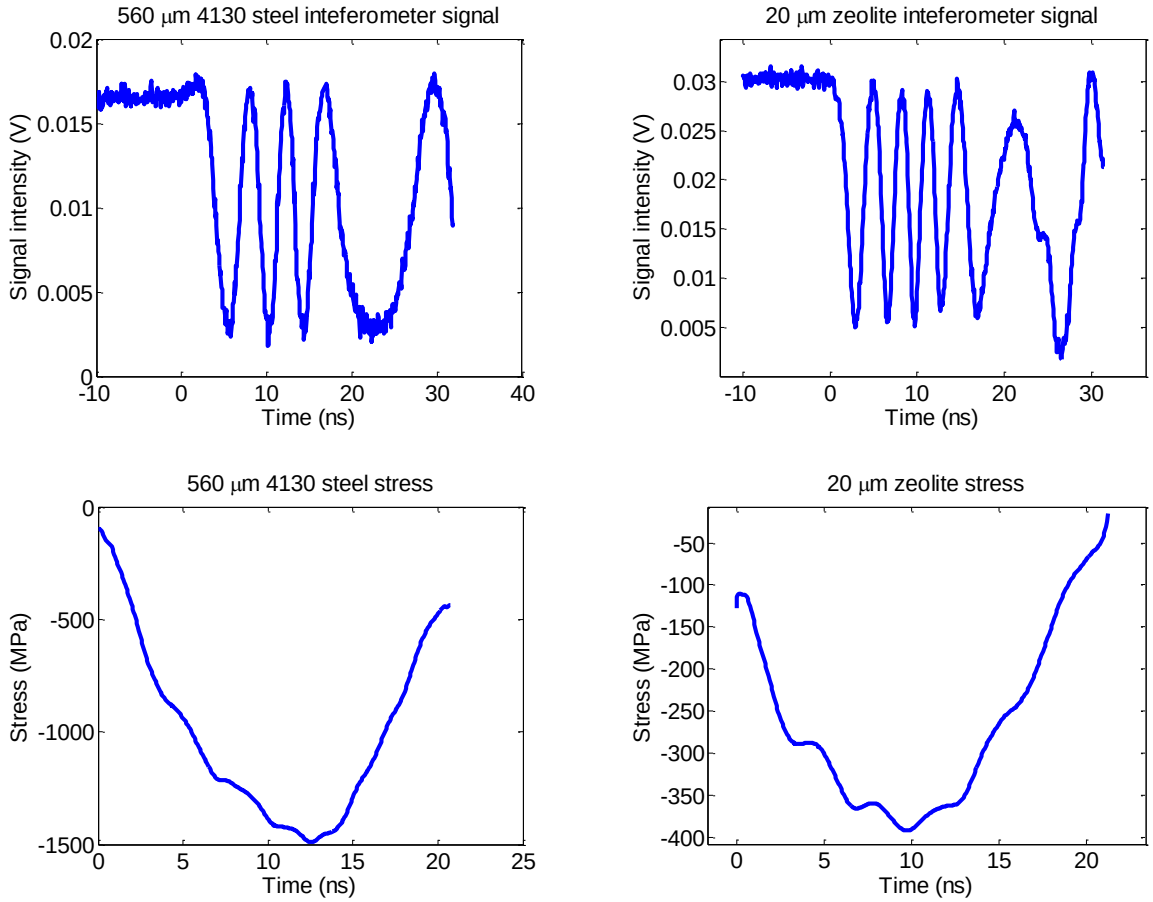

Figure 6.4: Interferometer signal (top) and stress history (bottom) for 560 μm thick 4130 bare substrate (left) and the same substrate coated with 20 μm thick ZSM-5 (right). Peak stress in the bare steel substrate was 1.5 GPa, while for the sample coated with the zeolite coating the peak stress is 400 MPa.

To increase the amount of interaction of the stress wave with the zeolite coating, a much thicker coating was grown via sequential hydrothermal synthesis. The resulting film was 63 μm thick, grown on a 290 μm thick 4130 substrate. Compression experiment with a 1.5 mm fused silica window were conducted, which simulates measurement of the in situ particle velocity. For fused silica windowing with moderate stress amplitude, no corrections are needed other than the stress calculations no longer having a one-half prefactor, which was previously required for free surface reflection since the incoming compressive wave and reflected tensile wave both displace the surface in the same direction.

Figure 6.5 (top-left) shows the recorded interferometer signal and (top-right) the stress history for the 63 μm thick zeolite on 330 μm 4130 substrate. For the thicker coating the stress profile is now asymmetric, with some features similar to that observed from the silicon testing. Peak stress ranges from 300-400 MPa, with an average near 330 MPa. SEM imaging, shown in Figure 6.5 (bottom), of the front surface revealed two distinct features: 1) some areas show spallation-like deformation; 2) surface cracking. The asymmetry of the stress profile can be attributed to the thinner substrate, which shows more elastic-plastic behavior than longer propagation distances in the thicker substrate.

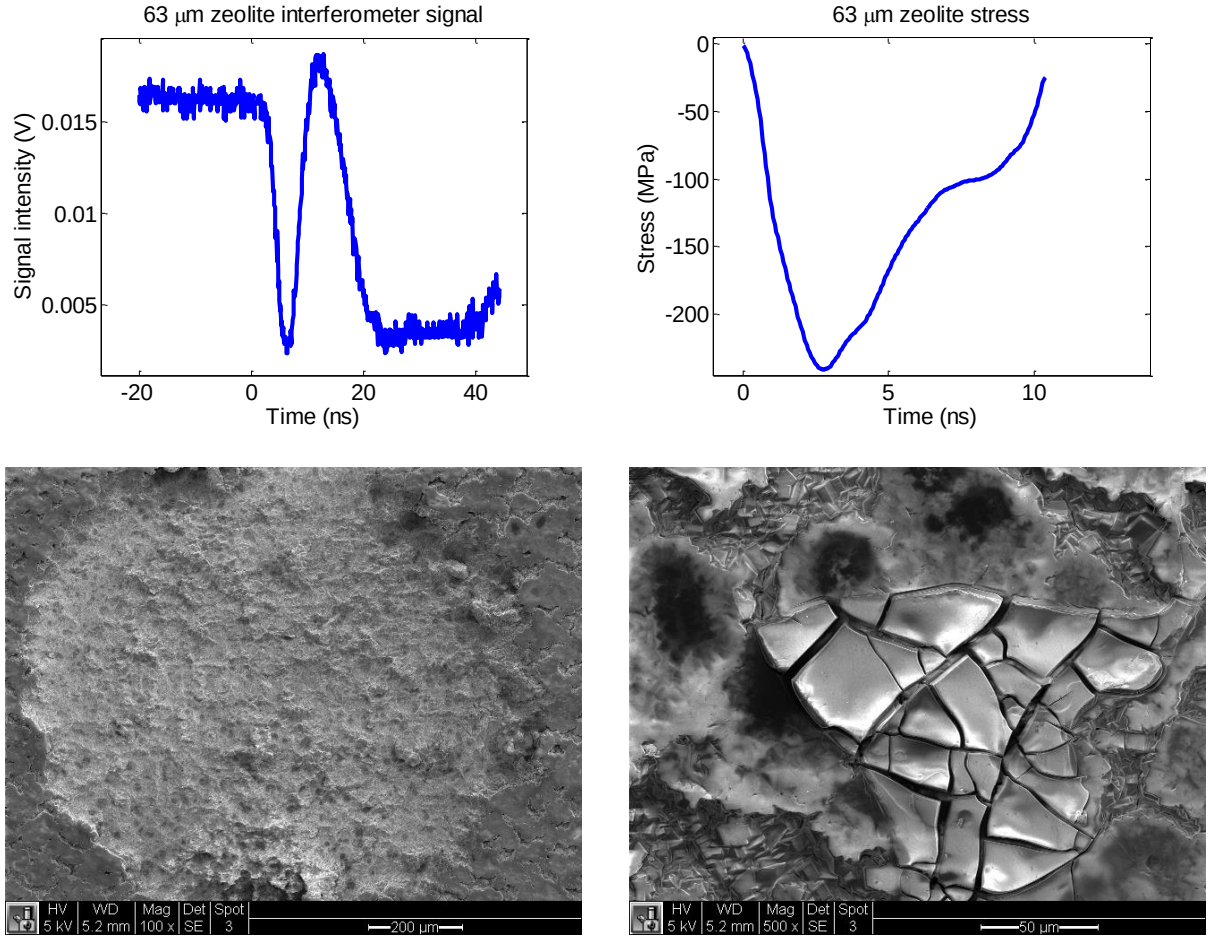

Figure 6.5: Top: Interferometer signal (left) and substrate stress history (right) for 63 μm zeolite. The thicker zeolite coating displays an asymmetric stress profile, with a peak stress of 300 MPa. Bottom: SEM images of resulting spallation and surface cracking.

6.5. Spallation Experiment with Bulk Zeolite

Due to the onset of brittle fracture observed during the compression experiments, and the observation of spallation for areas in which there was poor contact with the fused silica window, it was determined that more information on the dynamic response of zeolite could be extracted from spallation experiments. For this testing the substrate chosen was 6061 aluminum alloy, which has a higher stress transmission coefficient ($\beta_t = 0.72$). While 6061 aluminum alloy will plastically deform even at moderate stress levels and alter the stress profile, this will not inhibit spallation measurement as long as the zeolite experiences sufficient stress. Initial testing of an uncoated 6061 aluminum alloy substrate measured peak stresses of 3.5^{+} GPa. For the stress transmission coefficient from aluminum to zeolite we can expect stress levels of ~2.5 GPa.

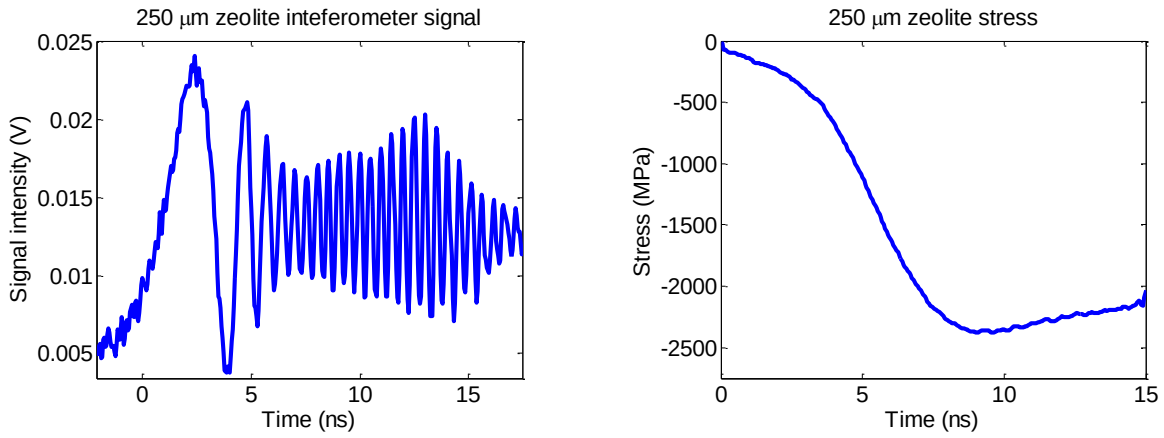

Figure 6.6: Interferometer signal (left) and substrate stress history (right) for 250 μm thick zeolite on 150 μm thick 6061 Al substrate. Usable fringe data only lasts for ~20 ns, before complete unloading. Peak stress measured is ~2.5 GPa.

Figure 6.6 shows the measured interferometer signal and derived stress history for the zeolite loaded at fluence of ~33 J/cm^2. Peak stress of 2.5 GPa was measured, consistent with peak stress measurement for the uncoated aluminum combined with the stress transmission efficiency. The elastic precursor and elastic-plastic transition from the 6061 is substrate clearly visible in the loading signal.

Due to degraded interferometry signal for some of the data collected, a new analysis technique was required which does not depend on data reduction at the individual half-fringe level. Instead, a specular technique was used, following the technique of Strand et al. [178], in which the frequency response as a function of time was interpreted by a shifting Fourier analysis. Fourier analysis was performed on 10 ns intervals, using a Blackman windowing function on each interval to ensure periodicity. A continuous spectrum is generated by advancing a single data point, 50 ps, for each spectrum analysis. The fringe frequency can be converted to surface velocity by multiplying by the fringe constant, $\lambda/2$. Figure 6.7 shows the spectrograph of the surface velocity in comparison with the velocity derived from fringe analysis, resulting from loading of 3.7 J/cm^2. Very good agreement is observed for the two profiles. While the fringe interpreted surface velocity shows sharper features, noise is more detrimental. The velocity spectrum is naturally smoothed by both the frequency resolution, as well as analyzing 10 ns at a time.

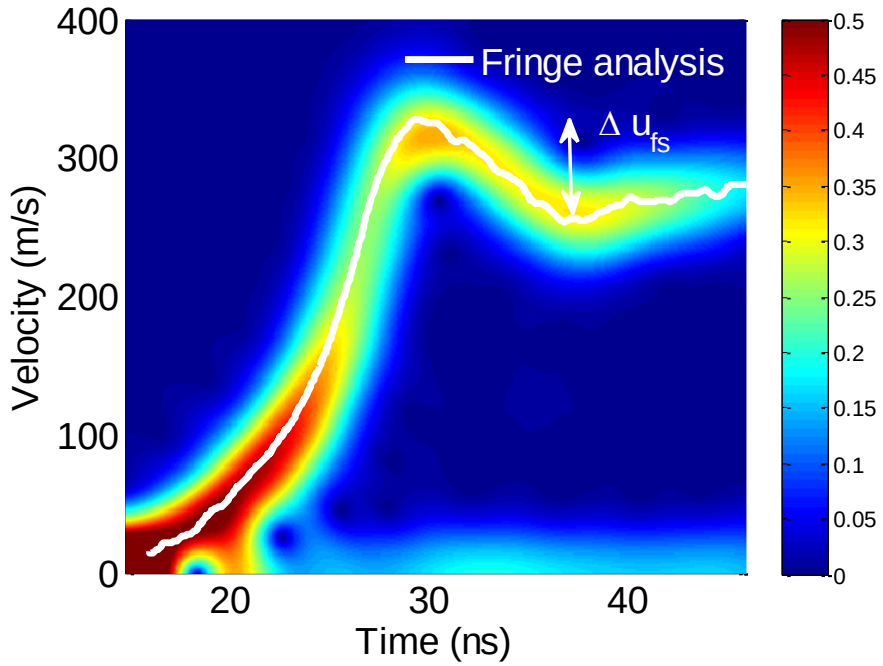

Figure 6.7: Velocity spectrograph compared with the fringe based data reduction. Δu_{fs} , the velocity pullback, is also indicated.

Also shown in Figure 6.7 is the signature of spallation, the pullback signal. The velocity pullback, Δu_{fs} , is labeled for convenience. The pullback signal is the result of the free surface reflected wave interacting with the unloading wave, creating a spall pulse. Within the "acoustic approach" the spallation strength can be extracted from the pullback signal by [179]:

$$\sigma_{\text{spall}} = \frac{1}{2}\rho c_L \Delta u_{\text{fs}} \tag{26}$$

where ρ is the density, c_L is the longitudinal wave speed, and Δu_{fs} is the aforementioned velocity pullback. Another spallation analysis technique depends on the spallation depth. If the stress history is known, then the stress at any depth, h, can be computed by:

$$\sigma(t;h) = \sigma(t - h/c_L) - \sigma(t + h/c_L) \tag{27}$$

Figure 6.8 shows measurement of the spallation depth by scanning, contact profilometry. The spallation depth was measured to be 110 μm, with a width of ~1.5 mm. This corresponds to a stress transit time of 20 ns. Spallation strength analysis using the spallation depth requires interferometry data for a time of at least $2h/c_L$, or 40 ns for this data. Interferometry data is not reliable for this duration, so spallation strength based on the velocity pullback must be used.

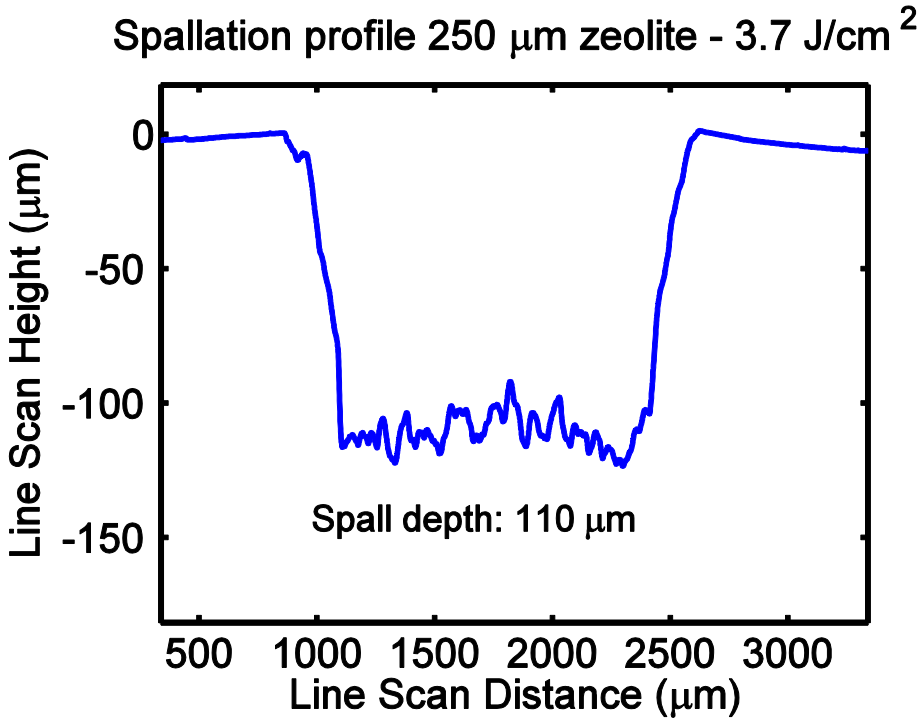

Figure 6.8: Profilometer measurement of spallation depth. Mean spallation depth was measured as 110 μm, while the spallation width is ~1.5 mm.

Figure 6.9 shows SEM images of the spallation surface at magnifications of 50x and 2000x, respectively. While image resolution is limited due to the charge buildup of the insulating zeolite, it is clear that dominant fracture feature is intergranular failure. Some large planar faces are also visible, which may be from transgranular failure.

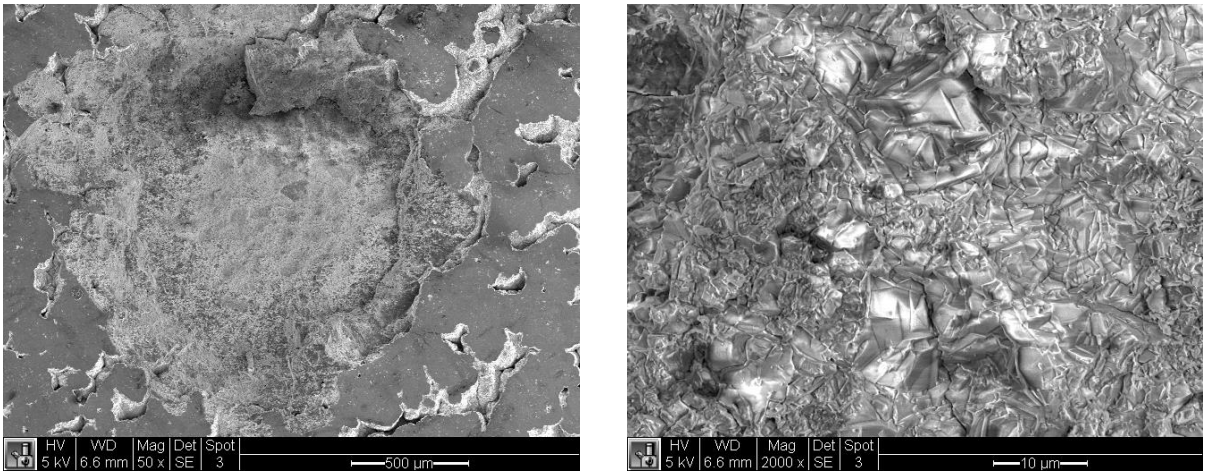

Figure 6.9: SEM images of spallation surface. Left image at 50x shows the large scale fracture structure, with noticeable steps away from the center of the spallation plane. Right image, zoomed to 2000x, shows the dominance of transgranular fracture, with some fracture facets of individual grain typical of intergranular fracture.

Due to the depth of the measured spallation, it was important to determine if the spallation was due to the bulk material failure, or being influenced by the substrate/zeolite interface. Energy-dispersive x-ray spectroscopy (EDS) generates characteristic x-rays which can originate from 5-10 μm deep within the sample. EDS was performed on the spall plane to determine if the composition matches that expected for the ZSM-5 zeolite, and the results are shown in Figure 6.10. The stoichiometry of uncalcinated ZSM-5 is $\left|\left(\left(C_3H_7\right)_4 NOH_4\right)\right|\left[Si_{95.7}Al_{0.3}O_{192}\right]$, with an expected Si-Al-O weight percentage of ~46.5-0.5-53%. The actual EDS measurements are ~45.1-0.4-54.5%. This indicates the spallation happened far enough away from the substrate such that no additional Al signal is measured.

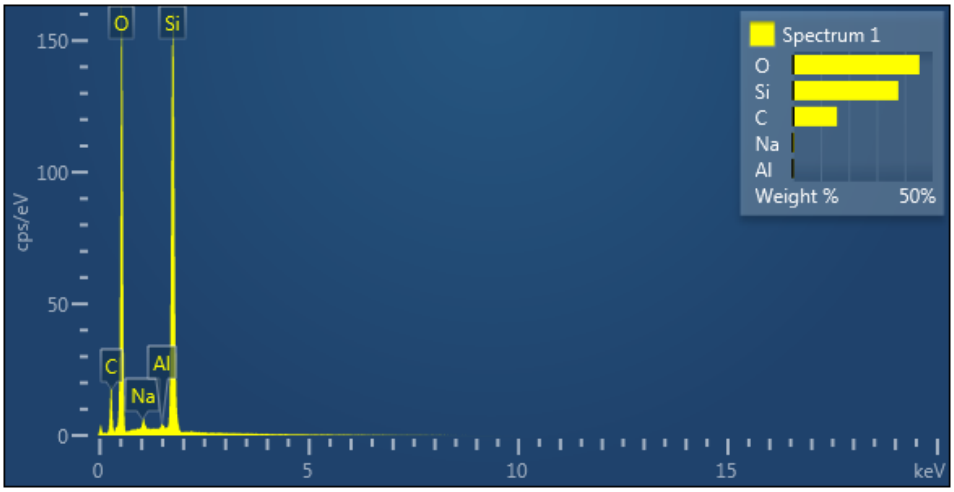

Figure 6.10: EDS analysis of the spallation area shown in Figure 6.9. Highest elemental percentages correspond to silicon and oxygen, as expected. Si-Al-O weight ratio agrees with that of the zeolite stoichiometry.

Correlation analysis was performed with the measurement values for laser energy, peak stress, spallation strength, and spallation depth, shown in Figure 6.11. Correlation coefficient for each variable pair is on the graph of the intersection of the row and column variable. Significant correlations are highlighted in red. Strongly correlated variable pairs are laser energy, peak stress, and spall depth. The spallation strength was measured with a mean of 215 MPa and standard deviation of 70 MPa. The intersection of a variable with itself shows the histogram of the measurements. Laser pulse energy, thus peak stress, was varied to determine if the zeolite spallation strength exhibits any trend. There is a small, positive correlation between peak stress and spallation strength, but the trend is far smaller than the data scatter.

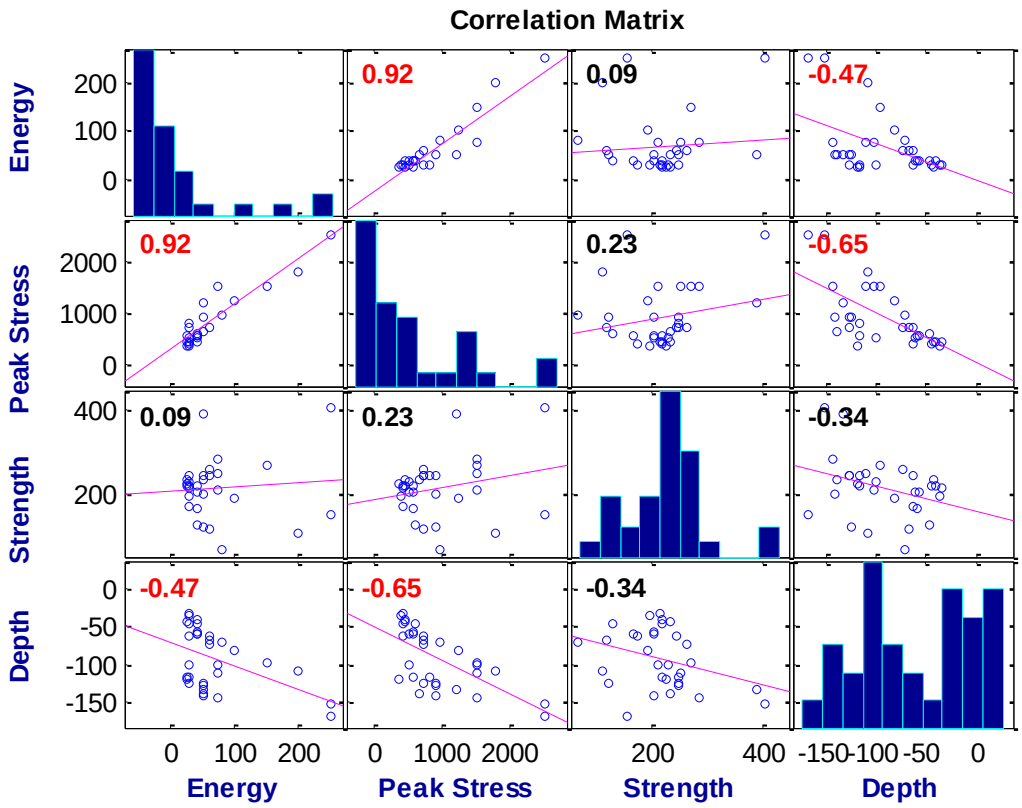

Figure 6.11: Correlation matrix for laser pulse energy, peak stress, spallation strength, and spallation depth. The numbers in each plot shows the correlation coefficient between the intersection of the row and column variable, with those in red showing significant correlation. Correlated variables are energy, peak stress, spall strength, and depth.

6.6. Discussion

Compression experiments using the 5 ns Tempest laser at fluences ~33 J/cm^2 on the zeolite coated and uncoated 4130 steel substrates showed several interesting behaviors. For both thin and thick coatings the stress history is an accurate temporal copy of the uncoated stress history. The 560 μm thick 4130 steel showed a Gaussian stress profile, with time constants for the uncoated and coated close to that of the loading laser. This is the expected elastic and long term propagation behavior for the stress wave away from the stress generation region. While at first inspection it would appear that the zeolite coating is quite remarkable in its attenuation capability, reducing the incident stress

amplitude of 1.5 GPa from the 4130 substrate to only 400 MPa, this response can be explained with purely elastic behavior. Upon arrival of the stress wave at the interface of the 4130 substrate and zeolite coating, stress and acceleration continuity are required. The result is that there is transmission and reflection at the interface. The transmission coefficient from steel to zeolite is given by:

$$\beta_t = \frac{2\left(\rho c_L\right)^{\text{ZSM-5}}}{\left(\rho c_L\right)^{\text{ZSM-5}} + \left(\rho c_L\right)^{4130}} = 0.32 \tag{28}$$

where ρ is the density, c_L is the longitudinal wave speed, and the superscript indicates the density and wave speed specified for either the zeolite (ZSM-5) or the steel (4130). A transmission coefficient of 0.32 is very close to the observed ratio of 0.27 and well within the error level associated with data reduction.

The observation of spallation of the zeolite coating is unexpected. Zeolite is very closely acoustically matched to the fused silica window material, allowing nearly all of the incident compressive stress to be efficiently transmitted from the zeolite to the window. Fused silica has a slightly higher acoustic impedance than zeolite, which results in the reflected wave at the zeolite-fused-silica interface to have the same sign as the incoming wave, i.e. a compressive wave is reflected at the surface, not a tensile wave. It may be possible that the tensile stress needed for spallation was generated from the free surface reflection at the fused silica window. While this wave will eventually interact with the film, fused silica is a highly nonlinear elastic solid. For stresses under 3.5 GPa it is dominated by negative nonlinear stress-strain behavior. The result of the negative nonlinear behavior is that low amplitude stress propagates faster than high amplitude stress [106, 180]. While the wave propagates through the window it will attenuate and stretch, leading to much lower stress. Additionally, the interface between the window and zeolite is unlikely capable of supporting significant tensile stress. Investigation of the

fringe record reveals that the areas with spallation had abnormally high stresses, twice as high as any other data. Stress and displacement twice that of the norm corresponds exactly to the expected behavior from a free surface reflection. A set of data were taken without the windowing material, which matched that of the anomalously high stress data where spallation was observed. In these areas the contact between the zeolite and the window was poor, resulting in a free surface for the zeolite coating.

The final SEM observation, shown at bottom right in Figure 6.5, is surface cracking of the zeolite. Surface cracking was observed with good interferometry data that indicated uniform contact with the fused silica window. Surface fracturing at moderate stress levels of 300-400 MPa is in sharp contrast with the mechanical response of zeolite under nanoindentation [165, 181], where no fracture features are observed even under maximum loading conditions, which represent contract stresses in excess of 3 GPa. There are two contributions to the observation of surface cracking at much lower stresses than observed for nanoindentation. The first contribution is the zeolite coatings used for this study are of a thickness where they behave as bulk materials. Nanoindentation is a local probe of the material property, unless done specifically near existing defect, e.g. grain boundaries [182]. For thin films defect concentration and flaw size generally grow with film thickness, as principal sites of defect concentration like grain boundaries become significant. As the typical zeolite crystal size ranges from 5-20 μm, any film thicker than this will begin to behave more as a bulk material. The second contribution to the observed zeolite behavior may be attributed to the very high strain-rate associated with laser loading. At very high strain-rates materials may undergo a ductile to brittle transition. Such a transition is possible when the stress rate, related to the elastic strain-rate, far exceeds the plastic strain-rate, which is responsible for crack tip blunting [183]. Nanoindentation results show that zeolite

has simultaneous high hardness (6.3 GPa) and low elastic modulus (51 GPa), resulting in high resilience [165]. For such materials under high strain-rate loading energy can be supplied to the crack tip faster than can be dissipated from blunting and crack advance. The appearance of multiple intersecting fractures also corroborates the possibility of a strain-rate driven ductile to brittle transition, as lower rate crack growth tends to initiate at a single area that has reached a critical stress level leading to catastrophic growth and branching before other flaws are activated [183].

Spallation experiments on 6061 aluminum alloy substrates with peak compressive stresses ranging from 250-3000 GPa were conducted to determine the dynamic tensile failure behavior of bulk zeolite. The brittle nature of zeolite under high strain-rate conditions was confirmed by the spallation study. SEM images of the spallation morphology show that the spallation is dominated by brittle transgranular fracture, but accompanied by some degree of intergranular fracture. Profile measurement and SEM images indicate the spallation area is larger than the loading area, indicating long term failure development after the initial onset of spallation, a typical response for brittle materials. Due to reduced signal quality at time scales relevant to the first wave interaction with the surface, a specular analysis technique was adopted to extract the relevant spallation feature from the interferometer data, the velocity pullback signal. EDS analysis performed within the spallation area indicates a close stoichiometric match to the bulk zeolite material, indicating the spallation happened far enough away from the interface that the true bulk spallation strength was measured. The bulk spallation strength of 215 MPa is substantially lower than that of the interfacial strength, measured to be 326 MPa [111]. Brittle material spallation strength can be sensitive to the initial compressive loading, as the compressive wave can act on preexisting flaws, microcracks, and grain boundaries to initiate the fracture process before arrival of the release wave. Correlation analysis shows there is no

significant dependence of the spallation strength on the loading parameters, e.g. laser pulse energy or peak stress, as is observed with some brittle materials such as alumina [184]. Strong correlation is observed between laser energy and peak stress, as expected, and also between energy/peak stress and spallation depth. This is further indication that the final spallation depth is determined by long term (post initial stress wave) fracture and fragmentation.

6.7. Conclusions

Under high strain-rate dynamic loading by short pulse laser-generated stress waves the behavior of bulk zeolite is that of a brittle solid. The only significant stress attenuation can be attributed to the acoustic mismatch between the substrate material and the bulk zeolite coating. Under moderate compressive loading of only several hundred MPa peak stress, surface fracturing is observed. The surface fracture morphology indicates simultaneous nucleation and propagation of cracks, a predominately high strain-rate brittle behavior. Spallation experiments with peak stress range from 250-3000 MPa were conducted. Spectral analysis of the interferometry data was used to extract the velocity pullback signal. The spallation strength was measured from the velocity pullback, with mean value of 215 MPa. This value is lower than that of the interfacial strength of zeolite. EDS analysis on the spallation area indicated no excess of aluminum, indicating spallation occurred away from the interface and the true bulk spallation strength was measured. SEM imaging showed the predominance of brittle transgranular fracture. No correlation was observed between the peak compressive stress and spallation strength.

Chapter 7. Concluding Remarks and Future Suggestions

7.1. Concluding Remarks

The objective of this dissertation was to study the dynamic, high strain-rate behavior of materials as elicited by loading from short pulse lasers. In order to understand the applicability of the technique, a parametric study was first carried out to understand the effect of various parameters on the stress wave generation. The technique was then applied to several material systems ranging from conventional solids such as Si and aluminum, to biological cells and further to nanoporous oxides, to understand their unique response under high strain-rate loading.

In the parametric study, the effect of laser pulse duration and confinement were studied in monolithic single crystal silicon at low and high fluences. For unconfined low fluence loading, it was observed that the measured stress profile was comparable to the laser duration with both laser pulse widths. Under high fluence and confined conditions, the stress profile is that of a strong shock with exponential decay release. For the 5 ns loading laser there is a dramatic transition is the stress profile, while for the 50 ps laser both low fluence/unconfined and high fluence/confined the principal difference is the peak stress generated. Both 5 ns and 50 ps laser at high fluence produced peak stresses of 7^{+} GPa with confinement. Under unconfined conditions only the 50 ps laser is capable of producing significant stress, which is due to the higher intensity. The 50 ps laser under unconfined conditions produces a stress wave which is still highly symmetric. Albeit lower peak stress is generated, an order of magnitude increase in the strain-rate is observed due to the symmetric rise and fall of the stress wave.

The high strain-rate compressive yielding behavior of two aluminum alloys, 6061 and 7075, was measured with 50 ps and 5 ns loading laser pulse durations. An elastic-plastic wave was observed, with transition stress occurring at a stress level consistent in the literature from several different dynamic loading techniques. Post Hugoniot elastic limit behavior shows propagation distance dependent wave evolution consistent with plasticity. At large propagation distances a steady elastic wave was observed, without an elastic-plastic transition. No rate dependency is observed between the 5 ns and 50 ps loading durations.

Transient finite element simulations were conducted of an experiment to measure the adhesion strength of cells to an inorganic substrate using the laser-induced stress wave technique. The simulation elucidated the cell detachment process, which was not observable during the experiment due to the short nanosecond time scale. A thin interfacial layer, with dimensions corresponding to the integrin-receptor bonding length, was explicitly modeled to extract the state of the interface during the stress wave interaction with the cell and cell-substrate interface. Both elastic and viscoelastic models were simulated for the cell and interface properties. The stress, strain, and failure evolution of the interface indicates there is no sensitivity to the time dependent properties of the cell material. This is due to the applied loading from the 5 ns laser is many orders of magnitudes shorter than the characteristic response time of the cell's viscous and active responses. Hydrophobic and hydrophilic cell geometries were considered, which describe the evolution of cell geometry from initial contact to fully spread. For both cell geometries the same failure process was observed. The principal detachment mechanism was found to be strain driven failure of the interface from the rapid acceleration of the substrate into the cell, whose tendency to flatten and elongate generate interfacial strains larger than can be accommodated by the protein bonding responsible for adhesion.

Nanoporous zeolite ZSM-5 was synthesized as a bulk coating of 4130 steel and 6061 aluminum alloy for compression and spallation measurements. Under the high strain-rate loading from laser-generated stress waves bulk zeolite behaves as a brittle material. Stress attenuation in compression experiments can be attributed to the acoustic mismatch between the substrate and zeolite coating. Surface fracturing during compressive loading, even under moderate loading, indicates brittle high strain-rate response. This is corroborated by SEM imaging of the crack morphology showing multiple intersecting fractures, a feature of high strain-rate brittle failure. Measurement of the spallation strength of bulk zeolite coatings on a closely acoustically matched 6061 aluminum alloy substrate indicate a dynamic tensile strength typical of brittle solids. The low spallation strength of zeolite compared to the interfacial strength of thin zeolite films indicates that when significant stress wave interaction happens within the coating thickness, brittle fracture will occur before the onset of delamination.

7.2. Future Suggestions

The effects of pulse duration and confinement from laser-generated stress waves allows variation of the peak stress, stress profile, as well as the strain-rate. With the fluences available from tabletop pulsed lasers, peak stresses in the 10's GPa range are feasible for moderate thickness samples. Stress profile alteration, as the result of varying the pulse duration or confinement conditions, allow investigation of material response overall several decades of strain-rate within the ultra-high-strain-rate regime. Laser pulse shaping, by methods such as injection, could also be pursued to study specific

thermodynamic loading paths, such as the quasi-isentropic compression response when materials are subjected to ramp loading.

The modeling of cell behavior considered in this dissertation determined that the cell detachment process proceeds by creating large interfacial strains from the rapid acceleration of the substrate into the cell. The details of the process depend critically on the behavior of the interfacial proteins during loading. Multiscale modeling, such as atomic-to-continuum, may provide a method for treating the complex protein behavior at the atomic level via molecular dynamics, while continuum methods like finite element analysis are used to model the large scale stress interactions.

A remaining fundamental question about the high strain-rate fracture of zeolite is whether the inherent nanoporous structure behaves as preexisting flaws for nucleation and coalescence, as well as the degree of pore collapse and compaction prior to the initiation of fracture. Low angle, time resolved x-ray diffraction could be used to infer whether the pore structure undergoes significant deformation, as well as whether the scattering centers remain periodic and a coherent diffraction signal is observed throughout the stress interaction.

References

1. Edgeworth R, Dalton BJ, Parnell T (1984) The pitch drop experiment. Eur J Phys 5:198–200.

2. Meyers M (1994) Dynamic Behavior of Materials, 1st ed. John Wiley & Sons, Inc., New York

3. Ramesh K (2008) High rates and impact experiments. In: Sharpe WNJ (ed) Handb. Exp. Solid Mechancs. Springer Science+Business Media, LLC, pp 929–959

4. Field JE, Walley SM, Proud WG, et al. (2004) Review of experimental techniques for high rate deformation and shock studies. Int J Impact Eng 30:725–775. doi: 10.1016/j.ijimpeng.2004.03.005

5. Campbell JD, Ferguson WG (1970) The temperature and strain-rate dependence of the shear strength of mild steel. Philos Mag 21:63–82. doi: 10.1080/14786437008238397

6. Johnson G, Cook W (1983) A constitutive model and data for metals subjected to large strains, high strain rates and high temperatures. Proceedsing 7th Int. Symp. Ballist. p 541

7. Johnson GR, Hoegfeldt JM, Lindholm US, Nagy A (1983) Response of Various Metals to Large Torsional Strains Over a Large Range of Strain Rates—Part 1: Ductile Metals. J Eng Mater Technol 105:42. doi: 10.1115/1.3225617

8. Johnson GR, Hoegfeldt JM, Lindholm US, Nagy A (1983) Response of Various Metals to Large Torsional Strains Over a Large Range of Strain Rates—Part 2: Less Ductile Metals. J Eng Mater Technol 105:48. doi: 10.1115/1.3225618

9. Andrade U, Meyers MA, Vecchio KS, Chokshi AH (1994) Dynamic recrystallization in high-strain, high-strain-rate plastic deformation of copper. Acta Metall Mater 42:3183–3195. doi: 10.1016/0956-7151(94)90417-0

10. Regazzoni G, Kocks UF, Follansbee PS (1987) Dislocation kinetics at high strain rates. Acta Metall 35:2865–2875. doi: 10.1016/0001-6160(87)90285-9

11. Zerilli FJ, Armstrong RW (1987) Dislocation-mechanics-based constitutive relations for material dynamics calculations. J Appl Phys 61:1816. doi: 10.1063/1.338024

12. Meyers M, Chawla K (1984) Mechanical metallurgy: principles and applications. Prentice-Hall, Inc., Englewood Cliffs

13. Parameswaran VR, Urabe N, Weertman J (1972) Dislocation Mobility in Aluminum. J Appl Phys 43:2982. doi: 10.1063/1.1661644

14. Mason WP (1960) Phonon Viscosity and Its Effect on Acoustic Wave Attenuation and Dislocation Motion. J Acoust Soc Am 32:458. doi: 10.1121/1.1908099

15. Gilman J (1968) Dislocation Motion in a Viscous Medium. Phys Rev Lett 20:157–158. doi: 10.1103/PhysRevLett.20.157

16. Steinberg DJ, Cochran SG, Guinan MW (1980) A constitutive model for metals applicable at high-strain rate. J Appl Phys 51:1498. doi: 10.1063/1.327799

17. Preston DL, Tonks DL, Wallace DC (2003) Model of plastic deformation for extreme loading conditions. J Appl Phys 93:211. doi: 10.1063/1.1524706

18. Hanson KM (2004) Introduciton to PTW. LA–UR–04–0305.

19. ASTM-Standard-D2763: Standard Test Method for High Speed Puncture Properties of Plastics Using Load and Displacement Sensors (2010) ASTM-Standard-D2763: Standard Test Method for High Speed Puncture Properties of Plastics Using Load and Displacement Sensors.

20. Hockett JE, Lindsay NA (1971) Cam plastometer data acquisition system. J Phys E 4:520–522. doi: 10.1088/0022-3735/4/7/009

21. Kuhn H, Medlin D (2000) High Strain Rate Tension and Compression Tests. ASM Handb. Vol. 8. ASM International, pp 429–446

22. ASTM-Standard-E680-79e1: Standard Test Method for Drop Weight Impact Sensitivity of Solid-Phase Hazardous Materials (2011) ASTM-Standard-E680-79e1:Standard Test Method for Drop Weight Impact Sensitivity of Solid-Phase Hazardous Materials.

23. Taylor G (1946) JAMES FORREST LECTURE 1946. THE TESTING OF MATERIALS AT HIGH RATES OF LOADING. J ICE 26:486–519. doi: 10.1680/ijoti.1946.13699

24. Taylor G (1948) The Use of Flat-Ended Projectiles for Determining Dynamic Yield Stress. I. Theoretical Considerations. Proc R Soc A Math Phys Eng Sci 194:289–299. doi: 10.1098/rspa.1948.0081

25. Whiffin AC (1948) The Use of Flat-Ended Projectiles for Determining Dynamic Yield Stress. II. Tests on Various Metallic Materials. Proc R Soc A Math Phys Eng Sci 194:300–322. doi: 10.1098/rspa.1948.0082

26. Carrington WE, Gayler ML V. (1948) The Use of Flat-Ended Projectiles for Determining Dynamic Yield Stress. III. Changes in Microstructure Caused by Deformation under Impact at High-Striking Velocities. Proc R Soc A Math Phys Eng Sci 194:323–331. doi: 10.1098/rspa.1948.0083

27. Wilkins ML (1973) Impact of cylinders on a rigid boundary. J Appl Phys 44:1200. doi: 10.1063/1.1662328

28. Erlich DC, Shockey DA, Seaman L (1982) Symmetric rod impact technique for dynamic yield determination. AIP Conf. Proceeding Vol. 78. AIP, pp 402–406

29. Johnson PC, Stein BA, Davis RS (1963) Measurement of Dynamic Plastic Flow Properties under Uniform Stress. ASTM Spec. Tech. Publ. No. 336 Symp. Dyn. Behav. Mater.

30. Hopkinson B (1904) The effects of momentary stresses in metals. Proc R Soc London 74:498–506.

31. Hopkinson B (1914) A Method of Measuring the Pressure Produced in the Detonation of High Explosives or by the Impact of Bullets. Philos Trans R Soc London Ser A, Contain Pap a Math or Phys Character 213 :437–456. doi: 10.1098/rsta.1914.0010

32. Davies RM (1948) A Critical Study of the Hopkinson Pressure Bar. Philos Trans R Soc A Math Phys Eng Sci 240:375–457. doi: 10.1098/rsta.1948.0001

33. Kolsky H (1949) An Investigation of the Mechanical Properties of Materials at very High Rates of Loading. Proc Phys Soc Sect B 62:676–700. doi: 10.1088/0370-1301/62/11/302

34. Gray GTI (2000) Classic Split-Hopkinson Pressure Bar Testing. In: Kuhn H, Medlin D (eds) ASM Handb. Vol. 8. ASM International, pp 462–476

35. Curran D (1987) Dynamic failure of solids. Phys Rep 147:253–388. doi: 10.1016/0370-1573(87)90049-4

36. Graham R (1993) Solids Under High Pressure Shock Compression: Mechanics, Physics, and Chemistry. Springer-Verlag, New York

37. Davison L, Shahinpoor M (1996) High-Pressure Shock Compression of Solids II. Springer-Verlag

38. Antoun T, Seaman L, Curran D (2003) Spall fracture. Springer-Verlag, New York

39. Espinosa H, Nemat-Nasser S (2002) Low-Velocity Impact Testing. In: Kuhn H, Medlin D (eds) ASM Handb. Vol. 8. ASM International, pp 539–559

40. Gray GTI (2002) Shock Wave Testing of Ductile Materials. In: Kuhn H, Medlin D (eds) ASM Handb. Vol. 8. ASM International, pp 530–538

41. Asay JR, Trucano TG, Hawke RS (1990) The use of hypervelocity launchers to explore previously inaccessible states of matter. Int J Impact Eng 10:51–66. doi: 10.1016/0734-743X(90)90048-Z

42. Ragan III CE, Silbert MG, Diven BC (1977) Shock compression of molybdenum to 2.0 TPa by means of a nuclear explosion. J Appl Phys 48:2860. doi: 10.1063/1.324094

43. Altshuller L, Moiseev B, Popov L, et al. (1968) RELATIVE COMPRESSIBILITY OF IRON AND LEAD AT PRESSURES OF 31 TO 34 MBAR. Sov Phys - JETP 27:420–422.

44. Ragan C (1980) Ultrahigh-pressure shock-wave experiments. Phys Rev A 21:458–463. doi: 10.1103/PhysRevA.21.458

45. Ragan C (1982) Shock compression measurements at 1 to 7 TPa. Phys Rev A 25:3360–3375. doi: 10.1103/PhysRevA.25.3360

46. Ragan C (1984) Shock-wave experiments at threefold compression. Phys Rev A 29:1391–1402. doi: 10.1103/PhysRevA.29.1391

47. Trunin RF (1994) Shock compressibility of condensed materials in strong shock waves generated by underground nuclear explosions. Physics-Uspekhi 37:1123–1145. doi: 10.1070/PU1994v037n11ABEH000055

48. Trunin R (1998) Shock compression of condensed materials. Cambridge University Press, Cambridge

49. Einstein A (1917) On the quantum theory of radiation. Phys Z 18:121–128.

50. Pedrotti FL, Pedrotti LS (1993) Introduction to Optics, 2nd ed. 426–454.

51. Gordon J, Zeiger H, Townes C (1954) Molecular Microwave Oscillator and New Hyperfine Structure in the Microwave Spectrum of NH3. Phys Rev 95:282–284. doi: 10.1103/PhysRev.95.282

52. Gordon J, Zeiger H, Townes C (1955) The Maser—New Type of Microwave Amplifier, Frequency Standard, and Spectrometer. Phys Rev 99:1264–1274. doi: 10.1103/PhysRev.99.1264

53. Schawlow A, Townes C (1958) Infrared and Optical Masers. Phys Rev 112:1940–1949. doi: 10.1103/PhysRev.112.1940

54. Maiman TH (1960) Stimulated Optical Radiation in Ruby. Nature 187:493–494. doi: 10.1038/187493a0

55. Ready J (1997) Industrial Applications of Lasers, 2nd ed. Academic Press, INC., San Deigo

56. McClung FJ, Hellwarth RW (1962) Giant Optical Pulsations from Ruby. J Appl Phys 33:828. doi: 10.1063/1.1777174

57. White RM (1963) Generation of Elastic Waves by Transient Surface Heating. J Appl Phys 34:3559–3567.

58. Ready J (1965) Mechanism of Electron Emission Produced by a Giant-Pulse Laser. Phys Rev 137:A620–A623. doi: 10.1103/PhysRev.137.A620

59. Ready JF (1965) Effects Due to Absorption of Laser Radiation. J Appl Phys 36:462. doi: 10.1063/1.1714012

60. Knecht WL (1965) Initial Energies of Laser-Induced Electron Emission From W. Appl Phys Lett 6:99. doi: 10.1063/1.1754195

61. Fenner NC (1966) Laser Used for Mass Analysis. Rev Sci Instrum 37:1068. doi: 10.1063/1.1720410

62. Penner SS (1966) Interaction of Laser Radiation with an Absorbing Semi-Infinite Solid Bar. J Appl Phys 37:2304. doi: 10.1063/1.1708808

63. Ehler AW (1966) Plasma Formed by a Laser Pulse on a Tungsten Target. J Appl Phys 37:4962. doi: 10.1063/1.1708173

64. Weichel H (1966) Expansion Rates of the Luminous Front of a Laser-Produced Plasma. Appl Phys Lett 9:334. doi: 10.1063/1.1754774

65. Bell CE (1967) LASER-INDUCED HIGH-PRESSURE SHOCK WAVES IN WATER. Appl Phys Lett 10:46. doi: 10.1063/1.1754840

66. Carome EF (1967) PHOTOGRAPHIC STUDIES OF LASER-INDUCED PRESSURE IMPULSES IN LIQUIDS. Appl Phys Lett 11:64. doi: 10.1063/1.1755031

67. Percival CM (1967) Laser-Generated Stress Waves in a Dispersive Elastic Rod. J Appl Phys 38:5313. doi: 10.1063/1.1709320

68. Anderholm N (1968) Laser generated pressure waves. Bull Am Phys Soc 13:388.

69. Skeen CH (1968) LASER-INDUCED ``BLOW-OFF'' PHENOMENA. Appl Phys Lett 12:369. doi: 10.1063/1.1651859

70. Büchl K, Hohla K, Wienecke R, Witkowski S (1968) Investigation of the blast wave from a laser produced gas breakdown. Phys Lett A 26:248–249. doi: 10.1016/0375-9601(68)90629-4

71. Anderholm NC (1970) LASER-GENERATED STRESS WAVES. Appl Phys Lett 16:113–115. doi: 10.1063/1.1653116

72. O'Keefe JD (1972) Laser-induced stress-wave and impulse augmentation. Appl Phys Lett 21:464. doi: 10.1063/1.1654220

73. Fox JA (1974) Effect of water and paint coatings on laser-irradiated targets. Appl Phys Lett 24:461. doi: 10.1063/1.1655012

74. Veeser L, Solem J (1978) Studies of Laser-Driven Shock Waves in Aluminum. Phys Rev Lett 40:1391–1394. doi: 10.1103/PhysRevLett.40.1391

75. Trainor R, Shaner J, Auerbach J, Holmes N (1979) Ultrahigh-Pressure Laser-Driven Shock-Wave Experiments in Aluminum. Phys Rev Lett 42:1154–1157. doi: 10.1103/PhysRevLett.42.1154

76. Eliezer S, Henis Z (2009) Equations of State. In: Eliezer S, Mima K (eds) Appl. Laser-Plasma Interact. CRC Press, Boca Raton, pp 181–242

77. Fairand BP (1972) Laser shock-induced microstructural and mechanical property changes in 7075 aluminum. J Appl Phys 43:3893. doi: 10.1063/1.1661837

78. Fox JA (1973) Laser-induced shock effects in Plexiglas and 6061-T6 aluminum. Appl Phys Lett 22:594. doi: 10.1063/1.1654520

79. Eliezer S, Gilath I, Bar-Noy T (1990) Laser-induced spall in metals: Experiment and simulation. J Appl Phys 67:715. doi: 10.1063/1.345777

80. Larson A (1974) Calculations of laser induced spall in aluminum targets. Los Alamos Laboratory Report No. LA-5619-MS.

81. Hoffman C (1975) Some effects of laser irradiation on aluminum. Los Alamos Laboratory Report No. LA-6189-MS. Los Alamos

82. Gilath I, Salzmann D, Givon M, et al. (1988) Spallation as an effect of laser-induced shock waves. J Mater Sci 23:1825–1828. doi: 10.1007/BF01115727

83. Gilath I, Eliezer S, Dariel MP, Kornblit L (1988) Brittle-to-ductile transition in laser-induced spall at ultrahigh strain rate in 6061-T6 aluminum alloy. Appl Phys Lett 52:1207. doi: 10.1063/1.99159

84. Cottet F, Boustie M (1989) Spallation studies in aluminum targets using shock waves induced by laser irradiation at various pulse durations. J Appl Phys 66:4067. doi: 10.1063/1.343991

85. Boustie M, Cottet F (1991) Experimental and numerical study of laser induced spallation into aluminum and copper targets. J Appl Phys 69:7533. doi: 10.1063/1.347570

86. De Resśguier T, Cottet F (1995) Experimental and numerical study of laser induced spallation in glass. J Appl Phys 77:3756. doi: 10.1063/1.358548

87. Boustie M, Rességuier T De, Hallouin M, et al. (1996) Some applications of laser-induced shocks on the dynamic behavior of materials. Laser Part Beams 14:225–235.

88. Dekel E, Eliezer S, Henis Z, et al. (1998) Spallation model for the high strain rates range. J Appl Phys 84:4851. doi: 10.1063/1.368727

89. Bullock AB, Bolton PR (1999) Laser-induced back ablation of aluminum thin films using picosecond laser pulses. J Appl Phys 85:460. doi: 10.1063/1.369393

90. Moshe E, Eliezer S, Henis Z, et al. (2000) Experimental measurements of the strength of metals approaching the theoretical limit predicted by the equation of state. Appl Phys Lett 76:1555. doi: 10.1063/1.126094

91. Heavens OS (1950) Some factors influencing the adhesion of films produced by vacuum evaporation. J Phys le Radium 11:355–360. doi: 10.1051/jphysrad:01950001107035500

92. Weaver C (1975) Adhesion of thin films. J Vac Sci Technol 12:18. doi: 10.1116/1.568754

93. Strong J (1935) On the Cleaning of Surfaces. Rev Sci Instrum 6:97. doi: 10.1063/1.1751951

94. Baglin JEE, Clark GJ (1985) Ion beam bonding of thin films. Nucl Instruments Methods Phys Res Sect B Beam Interact with Mater Atoms 7-8:881–885. doi: 10.1016/0168-583X(85)90488-4

95. Jacobsson R, Kruse B (1973) Measurement of adhesion of thin evaporated films on glass substrates by means of the direct pull method. Thin Solid Films 15:71–77. doi: 10.1016/0040-6090(73)90205-8

96. Jacobsson R (1976) Measurement of the adhesion of thin films. Thin Solid Films 34:191–199. doi: 10.1016/0040-6090(76)90454-5

97. Hull T, Colligon J, Hill A (1987) Measurement of thin film adhesion. Vacuum 37:327–330. doi: 10.1016/0042-207X(87)90018-2

98. Gent AN, Lewandowski LH (1987) Blow-off pressures for adhering layers. J Appl Polym Sci 33:1567–1577. doi: 10.1002/app.1987.070330512

99. Chu Y, Jeong HS, White RC, Durning CJ (1992) Characterization of adhesion in thin-film materials by the blister test. MRS Symp. Proc. pp 209–220

100. Thouless MD (1994) Fracture mechanics for thin-film adhesion. IBM J Reseach Dev Adhes Sci Technol 38:367.

101. Stephens AW, Vossen JL (1976) Abstract: Measurement of interfacial bond strength by laser spallation. J Vac Sci Technol 13:38. doi: 10.1116/1.568925

102. Vossen JL (1978) Measurements of film–substrate bond strength by laser spallation. Adhes Meas Thin Film Thick Film Bulk Coat 640:122–123.

103. Gupta V, Argon AS, Cornie JA, Parks DM (1990) Measurement of interface strength by laser-pulse-induced spallation. Mater Sci Eng A 126:105–117. doi: 10.1016/0921-5093(90)90116-K

104. Gupta V, Pronin A (1994) Recent developments in the laser spallation technique to measure the interface strength and its relationship to interface toughness with applications to metal/ceramic, ceramic/ceramic and ceramic/polymer interfaces. J Adhes Sci Technol 8:713–747. doi: 10.1163/156856194X00447

105. Wang J, Weaver RL, Sottos NR (2002) A parametric study of laser induced thin film spallation. Exp Mech 42:74–83.

106. Wang J, Weaver R, Sottos N (2003) Laser-induced decompression shock development in fused silica. J. Appl. Phys.

107. Wang J, Sottos NRN, Weaver RL (2003) Mixed-mode failure of thin films using laser-generated shear waves. Exp Mech 43:323–330. doi: 10.1007/BF02410531

108. Wang J, Sottos N, Weaver R (2004) Tensile and mixed-mode strength of a thin film-substrate interface under laser induced pulse loading. J Mech Phys Solids 52:999–1022.

109. Hu L, Wang J (2006) Pure-shear Failure of Thin Films by Laser-induced Shear Waves. Exp Mech 46:637–645. doi: 10.1007/s11340-006-9345-5

110. Gupta V, Argon AS, Cornie JA, Parks DM (1990) Measurement of interface strength by laser-pulse-induced spallation. Mater Sci Eng A 126:105–117.

111. Hu L, Wang J, Li Z, et al. (2006) Interfacial adhesion of nanoporous zeolite thin films. J Mater Res 21:505–511.

112. Hu L, Miller P, Wang J (2009) High strain-rate spallation and fracture of tungsten by laser-induced stress waves. Mater Sci Eng A 504:73–80.

113. Tran P, Kandula SS V., Geubelle PH, Sottos NR (2008) Hybrid spectral/finite element analysis of dynamic delamination of patterned thin films. Eng Fract Mech 75:4217–4233. doi: 10.1016/j.engfracmech.2008.03.006

114. Kandula SS V., Tran P, Geubelle PH, Sottos NR (2008) Dynamic delamination of patterned thin films. Appl Phys Lett 93:261902. doi: 10.1063/1.3056639

115. Hu L, Zhang X, Miller P, et al. (2006) Cell adhesion measurement by laser-induced stress waves. J Appl Phys 100:084701. doi: 10.1063/1.2356107

116. Miller P, Hu L, Wang J (2010) Finite element simulation of cell–substrate decohesion by laser-induced stress waves. J Mech Behav Biomed Mater 3:268–277.

117. Fabbro R, Fournier J, Ballard P, et al. (1990) Physical study of laser-produced plasma in confined geometry. J Appl Phys 68:775–784.

118. Phipps JCR, Turner TP, Harrison RF, et al. (1988) Impulse coupling to targets in vacuum by KrF, HF, and CO[sub 2] single-pulse lasers. J Appl Phys 64:1083–1096.

119. Ivanov D, Zhigilei L (2003) Combined atomistic-continuum modeling of short-pulse laser melting and disintegration of metal films. Phys Rev B 68:064114. doi: 10.1103/PhysRevB.68.064114

120. Timm R, Willmott PR, Huber JR (1996) Ablation and blow-off characteristics at 248 nm of Al, Sn and Ti targets used for thin film pulsed laser deposition. J Appl Phys 80:1794. doi: 10.1063/1.362990

121. Willmott P, Huber J (2000) Pulsed laser vaporization and deposition. Rev Mod Phys 72:315–328. doi: 10.1103/RevModPhys.72.315

122. Bridges WB, Chester AN (1965) Visible and uv Laser Oscillation at 118 Wavelengths in Ionized Neon, Argon, Krypton, Xenon, Oxygen, and Other Gases. Appl Opt 4:573. doi: 10.1364/AO.4.000573

123. Wang J (2002) Thin-Film Adhesion Measurement by Laser-Induced Stress Waves. University of Illinois at Urbana-Champaign

124. Hoffman C (1976) Some Effects of Laser Irradiation on Aluminum. LA–6189–MS.

125. Eliezer S, Gilath I, Bar-Noy T (1990) Laser-induced spall in metals: Experiment and simulation. J Appl Phys 67:715. doi: 10.1063/1.345777

126. Russo RE (1995) Laser Ablation. Appl Spectrosc 49:14A–28A.

127. Loveridge-Smith A, Allen A, Belak J, et al. (2001) Anomalous Elastic Response of Silicon to Uniaxial Shock Compression on Nanosecond Time Scales. Phys Rev Lett 86:2349–2352.

128. Yang LC (1974) Stress waves generated in thin metallic films by a Q -switched ruby laser. J Appl Phys 45:2601. doi: 10.1063/1.1663636

129. Huang H, Asay JR (2005) Compressive strength measurements in aluminum for shock compression over the stress range of 4–22 GPa. J Appl Phys 98:033524. doi: 10.1063/1.2001729

130. Cozens-Roberts C, Quinn JA, Lauffenburger DA (1990) Receptor-mediated cell attachment and detachment kinetics. II. Experimental model studies with the radial-flow detachment assay. Biophys J 58:857–872.

131. Van Kooten TG, Schakenraad JM, Vandermei HC, Busscher HJ (1992) Development and Use of a Parallel-Plate Flow Chamber for Studying Cellular Adhesion to Solid-Surfaces. J Biomed Mater Res 26:725–738.

132. Garcia AJ, Huber F, Boettiger D (1998) Force required to break alpha(5)beta(1) integrin-fibronectin bonds in intact adherent cells is sensitive to integrin activation state. J Biol Chem 273:10988–10993.

133. Giacomello E, Neumayer J, Colombatti A, Perris R (1999) Centrifugal assay for fluorescence-based cell adhesion adapted to the analysis of ex vivo cells and capable of determining relative binding strengths. Biotechniques 26:758–762.

134. Kidoaki S, Matsuda T (1999) Adhesion forces of the blood plasma proteins on self-assembled monolayer surfaces of alkanethiolates with different functional groups measured by an atomic force microscope. Langmuir 15:7639–7646.

135. Shin D, Athanasiou K (1999) Cytoindentation for obtaining cell biomechanical properties. J Orthop Res 17:880–890.

136. Ashkin A (1970) Acceleration and trapping of particles by radiation pressure. Phys Rev Lett 24:156–159.

137. Ashkin A, Dziedzic JM (1987) Optical Trapping and Manipulation of Viruses and Bacteria. Science (80-) 235:1517–1520.

138. Ashkin A, Dziedzic JM, Yamane T (1987) Optical Trapping and Manipulation of Single Cells Using Infrared-Laser Beams. Nature 330:769–771.

139. Ashkin A, Dziedzic JM (1989) Optical Trapping and Manipulation of Single Living Cells Using Infrared-Laser Beams. Berichte Der Bunsen-Gesellschaft-Physical Chem Chem Phys 93:254–260.

140. McGarry JG, Prendergast PJ (2004) A three-dimensional finite element model of an adherent eukaryotic cell. Eur Cell Mater 7:27.

141. McGarry JP, Murphy BP, McHugh PE (2005) Computational mechanics modelling of cell-substrate contact during cyclic substrate deformation. J Mech Phys Solids 53:2597–2637.

142. Sato M, Ohshima N, Nerem RM (1996) Viscoelastic properties of cultured porcine aortic endothelial cells exposed to shear stress. J Biomech 29:461–467.

143. Yeung A, Evans E (1989) Cortical shell-liquid core model for passive flow of liquid-like spherical cells into micropipets. Biophys J 56:139–149.

144. Evans E, Yeung A (1989) Apparent viscosity of cortical tension of blood granulocytes determined by micropipet aspiration. Biophys J 56:151–169.

145. Dong C, Skalak R, Sung KL (1991) Cytoplasmic rheology of passive neutrophils. Biorheology 28:557–567.

146. Hochmuth RM, Ting-Beall HP, Beaty BB, et al. (1993) Viscosity of passive human neutrophils undergoing small deformations. Biophys J 64:1596–1601.

147. Tsai MA, Frank RS, Waugh RE (1993) Passive mechanical behavior of human neutrophils: power-law fluid. Biophys J 65:2078–2088.

148. Dong C, Skalak R, Sung KL, et al. (1998) Passive deformation analysis of human leukocytes. J Biomech Eng 110:27–36.

149. Alcaraz J, Buscemi L, Grabulosa M, et al. (2003) Microrheology of human lung epithelial cells measured by atomic force microscopy. Biophys J 84:2071–9. doi: 10.1016/S0006-3495(03)75014-0

150. Fabry B, Maksym GN, Butler JP, et al. (2003) Time scale and other invariants of integrative mechanical behavior in living cells. Phys Rev E 68:41914.

151. Leterrier JF (2001) Water and the cytoskeleton. Cell Mol Biol 47:901–923.

152. Lim CT, Zhou EH, Quek ST (2006) Mechanical models for living cells--a review. J Biomech 39:195–216.

153. Liang Y, Bi X, Wang J (2008) Numerical simulation of laser-induced thin film delamination. Thin Solid Films 516:971–981.

154. Chan BP, Bhat VD, Yegnasubramanian S, et al. (1999) An equilibrium model of endothelial cell adhesion via integrin-dependent and integrin-independent ligands. Biomaterials 20:2395–2403.

155. Dong C, Lei XX (2000) Biomechanics of cell rolling: shear flow, cell-surface adhesion, and cell deformability. J Biomech 33:35–43.

156. Guilak F, Mow VC (2000) The mechanical environment of the chondrocyte: a biphasic finite element model of cell–matrix interactions in articular cartilage. J Biomech 33:1663–1673.

157. Schmid-Schonbein GW, Sung K-LPL, Tozeren H, et al. (1981) Passive mechanical properties of human leukocytes. Biophys J 36:243–256.

158. Kamm RD, McVittie AK, Bathe M, et al. (2000) On the role of continuum models in mechanobiology. ASME Appl Mech Div 242:1–12.

159. Leckband D (2004) Nanomechanics of adhesion proteins. Curr Opin Struct Biol 14:524–530.

160. Hallquist JO (1998) LS-DYNA Theoretical Manual. 498.

161. Shewchuk JR (2002) Delaunay Refinement Algorithms for Triangular Mesh Generation. Comput Geom Theory Appl 22:21–74.

162. McGarry JP, Fu J, Yang MT, et al. (2009) Simulation of the contractile response of cells on an array of micro-posts. Philos Trans R Soc A Math Phys Eng Sci 367:3477.

163. Deshpande VS, McMeeking RM, Evans AG (2006) A bio-chemo-mechanical model for cell contractility. Proc Natl Acad Sci 103:14015.

164. Michael KE, Dumbauld DW, Burns KL, et al. (2009) Focal Adhesion Kinase Modulates Cell Adhesion Strengthening via Integrin Activation. Mol Biol Cell 20:2508–2519. doi: 10.1091/mbc.E08-01-0076

165. Chow G, Bedi RS, Yan Y, Wang J (2012) Zeolite as a wear-resistant coating. Microporous Mesoporous Mater 151:346–351. doi: 10.1016/j.micromeso.2011.10.013

166. Flanigen EM, Bennett JM, Grose RW, et al. (1978) Silicalite, a new hydrophobic crystalline silica molecular sieve. Nature 271:512–516. doi: 10.1038/271512a0

167. Zel'dovich Y, Raizer YP (1967) Physics of shock waves and high-temperature hydrodynamic phenomena Volume II, 2nd ed. Academic Press, INC., New York

168. Kokotailo G, Lawton S, Olson D (1978) Structure of synthetic zeolite ZSM-5. Nature

169. Olson DH, Kokotailo GT, Lawton SL, Meier WM (1981) Crystal structure and structure-related properties of ZSM-5. J Phys Chem 85:2238–2243. doi: 10.1021/j150615a020

170. Lew CM, Cai R, Yan Y (2010) Zeolite thin films: from computer chips to space stations. Acc Chem Res 43:210–9. doi: 10.1021/ar900146w

171. Yokomori Y, Idaka S (1999) The structure of TPA-ZSM-5 with Si/Al=23. Microporous Mesoporous Mater 28:405–413. doi: 10.1016/S1387-1811(98)00311-4

172. Van Koningsveld H, van Bekkum H, Jansen JC (1987) On the location and disorder of the tetrapropylammonium (TPA) ion in zeolite ZSM-5 with improved framework accuracy. Acta Crystallogr Sect B Struct Sci 43:127–132. doi: 10.1107/S0108768187098173

173. Rietveld H (1967) Line profiles of neutron powder-diffraction peaks for structure refinement. Acta Crystallogr.

174. Rietveld H (1969) A profile refinement method for nuclear and magnetic structures. J. Appl. Crystallogr.

175. Lutterotti L (1999) MAUD (material analysis using diffraction): a user friendly Java program for Rietveld texture analysis and more. Proceeding Twelfth Int. Conf. Textures Mater. 1:

176. Lutterotti L, Matthies S, Wenk H (1999) MAUD: a friendly Java program for material analysis using diffraction. IUCr Newsl CPD 21:14–15.

177. Baerlocher C, McCusker LB Database of Zeolite Structure. http://www.iza-structure.org/databases/.

178. Strand OT, Goosman DR, Martinez C, et al. (2006) Compact system for high-speed velocimetry using heterodyne techniques. Rev Sci Instrum 77:083108. doi: 10.1063/1.2336749

179. Novikov S, Divnov I, Ivanov A (1966) The study of fracture of steel, aluminium and copper under explosive loading. Fiz Met i Metalloved 21:608–615.

180. Barker LM (1970) Shock-Wave Studies of PMMA, Fused Silica, and Sapphire. J Appl Phys 41:4208. doi: 10.1063/1.1658439

181. Johnson M, Li Z, Wang J, Yan Y (2007) Mechanical characterization of zeolite low dielectric constant thin films by nanoindentation. Thin Solid Films 515:3164–3170. doi: 10.1016/j.tsf.2006.01.048

182. Lian J, Garay JE, Wang J (2007) Grain size and grain boundary effects on the mechanical behavior of fully stabilized zirconia investigated by nanoindentation. Scr Mater 56:1095–1098. doi: 10.1016/j.scriptamat.2007.02.027

183. Freund LB (1998) Dynamic Fracture Mechanics. 469–470,509.

184. Rozenberg Z (1991) The Response of Ceramic Materials to Shock Loading. In: Schmidt RD, Forbes JW, Tasker DG (eds) Shock Compression Condens. Matter. pp 439–444

Appendix A Derivation of Stress-Velocity Relation

The rate of change of momentum for a body is equal to the external forces acting upon it. For a 1D scenario this can be stated as:

$$F = \frac{d}{dt}(mv) \tag{A1}$$

$$\sigma A = \frac{d}{dt}(\rho \cdot A \cdot dx \cdot v) \tag{A2}$$

$$\sigma = \rho \frac{dx}{dt} v + \rho \cdot dx \cdot \frac{dv}{dt} \tag{A3}$$

where the force has been decomposed to a stress σ acting on a surface A, and the mass is given as: $\rho \cdot A \cdot dx$. Disregarding the product of differentials $dx \cdot \frac{dv}{dt}$ as being much small than the first term, i.e. $dx \cdot \frac{dv}{dt} \ll \frac{dx}{dt} v$, and realizing that $\frac{dx}{dt}$ is the characteristic c_L, we arrive at the conservation of momentum which relates stress to the particle velocity

$$\sigma = \rho \cdot c_L \cdot v \tag{A4}$$

Since our measurements are conducted at the sample free surface, the measured displacement is twice that within the bulk of the material, $v = \frac{1}{2} \cdot \frac{\partial u_{fs}}{\partial t}$. This is due to the incoming compressive wave and reflected tensile wave displacing the free surface in the same direction, following $u(x,t) = \frac{1}{\rho \cdot c_L} \left\{ \int_0^{t - x/c_L} \sigma(\tau) d\tau + \int_0^{t - h/c_L + (x-h)/c_L} \sigma(\tau) d\tau \right\}$, where h is an arbitrary distance within the sample to the free surface. Substituting $x = h$ we see that integrals are equal, resulting in doubling the displacement.

The conservation relationship between stress and particle velocity can also be derived by first considering the balance of linear momentum:

$$\sigma_{ij,j} = \rho \cdot \ddot{u}_i \tag{A5}$$

which for 1D reduces to:

$$\frac{\partial \sigma_{xx}}{\partial x} = \rho \cdot \frac{\partial^2 u_x}{\partial t^2} \tag{A6}$$

Under uniaxial strain conditions the stress and strain are related by:

$$\sigma_{xx} = (\lambda + 2\mu) \cdot \varepsilon_{xx} = (\lambda + 2\mu) \cdot \frac{\partial u_x}{\partial x} \tag{A7}$$

where λ, and μ are Lame's constants. Combining with the balance of linear momentum:

$$\frac{\partial}{\partial x}\left\{(\lambda + 2\mu) \cdot \frac{\partial u_x}{\partial x}\right\} = \rho \cdot \frac{\partial^2 u_x}{\partial t^2} \tag{A8}$$

we arrive at the 1D elastodynamic wave equation:

$$\frac{\partial^2 u_x}{\partial t^2} = c_L^2 \frac{\partial^2 u_x}{\partial x^2} \tag{A9}$$

where $c_L^2 = \dfrac{\lambda + 2\mu}{\rho}$ is the characteristic of the wave equation (for uniaxial strain). From D'Alembert, the wave equation admits solutions of the form: $u = f(x + c \cdot t)$, where $f(\cdot)$ is an arbitrary function. The spatial derivative of the D'Alembert's solution is:

$\frac{\partial u_x}{\partial x} = \frac{\partial f\left(x + c \cdot t\right)}{\partial\left(x + c \cdot t\right)} \cdot \frac{\partial\left(x + c \cdot t\right)}{\partial x} = f'\left(x + c \cdot t\right) \cdot \left(1\right) = f'\left(x + c \cdot t\right)$, while the temporal derivative is given by: $\frac{\partial u_x}{\partial t} = \frac{\partial f\left(x + c \cdot t\right)}{\partial\left(x + c \cdot t\right)} \cdot \frac{\partial\left(x + c \cdot t\right)}{\partial t} = f'\left(x + c \cdot t\right) \cdot \left(c\right) = c \cdot f'\left(x + c \cdot t\right)$. The derivative of the arbitrary function must be continuous, single valued, and equal, thus: $\frac{1}{c} \cdot \frac{\partial u_x}{\partial t} = \frac{\partial u_x}{\partial x}$. $\frac{\partial u_x}{\partial x}$ is related to the stress by the constitutive relationship, i.e. $\frac{\partial u_x}{\partial x} = \frac{\sigma_{xx}}{\lambda + 2\mu}$, while the elastic constants are related to the wave speed by the 1D characteristic: $\left(\lambda + 2\mu\right) = c_L^2 \cdot \rho$. Combining, we arrive at the conservation of momentum relating stress to the particle velocity:

$\frac{1}{c_L} \cdot \frac{\partial u_x}{\partial t} = \frac{\partial u_x}{\partial x} = \frac{\sigma_{xx}}{\left(\lambda + 2\mu\right)} = \frac{\sigma_{xx}}{c_L^2 \cdot \rho}$ with the final result being:

$$\sigma_{xx} = \rho \cdot c_L \cdot \frac{\partial u_x}{\partial t} \tag{A10}$$

Appendix B Fringe Data Analysis

```
% fringe analysis
% open files from Lecroy oscilloscope
% assumes folders AllData and AllFigures exist in data parent
folder
% clear workspace and any open figures

close all;clear;clc;format long;format compact;

% Load input data
%
% this function presents the user with a dialog box
% to pick the input file

[handles.fname,...
    handles.pname,...
    handles.findex] = uigetfile( ...
    {'*.dat','LeCroy MATLAB Output File (*.dat)';
    '*.m;*.fig;*.mat;*.mdl', 'All MATLAB Files (*.m, *.fig,
*.mat, *.mdl)';
    '*.*',  'All Files (*.*)'}, ...
    'Pick a file');

% fname is the complete path/file name and is formed by
% concatenating the pathname and filename string variables

handles.datafile = strcat(handles.pname,handles.fname);

% checks to see which filterindex was used to decide the input
option
% filterindex 1 is for the default output the LeCroy
oscilloscope uses
% when a MATLAB file is specified

if handles.findex == 1
    % loads the data from fname (*.dat)
    handles.data = load(handles.datafile);
else
    % uses uiimport to import data, may work for some data
formats
    uiimport(handles.datafile);
end

% Convert to nanoseconds for convenience
handles.data(:,1) = handles.data(:,1) * 1e9;
```

```
% Set first data point to 0 seconds in time
handles.data(:,1) = handles.data(:,1) - handles.data(1,1);

% New data arrays to be used for manipulation
handles.current_data = handles.data;
handles.mod_data = handles.data;

% smoothing based on smooth function (moving average)
% for very fast shocks width of ~3 works well, for slower
signals up to 20
% pts works
% 4 pts & 2 iterations works for many signals (2 iterations is
recommended
% for a rectangular smoothing filter used with taking 1st
derivative)

handles.Swidth=4;
handles.Sits=2;
for ii=1:handles.Sits;

handles.current_data(:,2)=smooth(handles.current_data(:,2),...
        handles.Swidth);
end

% variables assosicated with material constants
% e.g. these are for 4130 Steel without film

handles.FilmThickness = 0.0;            % micron
handles.FilmDesntiy = 0.0;              % gram per cubic
centimeter
handles.SubstrateDensity = 7.85;        % gram per cubic
centimeter
handles.WaveSpeedInSubstrate = 5850;    % meter per second
handles.TimeStep = 0.05;                % oscilloscope time
step, nano-seconds
handles.Lambda = 514.5;                 % wavelength of Argon-
ion laser, nm
handles.ThickFilm=0;                    % 1 means the film is
thick and
% interface stress will be calculated from sigma(t+2h/c)-
sigma(t)
handles.FilmSpeed=5000;                 % needed for h/c calc
handles.HOverC=int64(handles.FilmThickness/...
    handles.FilmSpeed/handles.TimeStep*1000);   % h/c needed for
shifting substrate stress
```

```
% interactive plot of the data
% user uses the left mouse button to define the new range and
zoom
% into the data of interest. Left mouse click on left range and
right mouse
% click on right range defines final range used in analysis

handles.fh = figure;
handles.FullScreenPosition=[1 49 1920 952];
handles.axes1 = axes('Parent',handles.fh);
plot(handles.axes1,...
    handles.current_data(:,1),...
    handles.current_data(:,2));
xlabel(handles.axes1 , 'Time (ns)');
ylabel(handles.axes1 , 'Photodetector Signal (V)');
% set(gcf,'Position',handles.FullScreenPosition);
set(handles.fh,'units','normalized','outerposition',[0 0 1 1]);
but = 1;
index = 1;
while but == 1
    [a, b, but] = ginput(2);
    [tmpvar,LB(index)]=min(abs(handles.current_data(:,1)-a(1)));
    [tmpvar,UB(index)]=min(abs(handles.current_data(:,1)-a(2)));
    handles.current_data =
handles.current_data(LB(index):UB(index),:);
    handles.current_data(:,1) = ...
        handles.current_data(:,1) - handles.current_data(1,1);
    plot(handles.axes1, ...
        handles.current_data(:,1), ...
        handles.current_data(:,2), ...
        '-o','MarkerSize',2);
    xlabel(handles.axes1, 'Time (ns)');
    ylabel(handles.axes1, 'Photodetector Signal (V)');
    index=index+1;
end
handles.mod_data = handles.current_data;
% Set the current data values & plot
plot(handles.axes1,...
    handles.mod_data(:,1),...
    handles.mod_data(:,2));
xlabel(handles.axes1,'Time (ns)');
ylabel(handles.axes1,'Photodetector Signal (V)');

% check timestep
handles.TimeStep=mean(diff(handles.data(:,1)));
```

```
% Find the maximums and the minimums by finding any data points
which are
% the maximum/minimum within the specified span for the search
width

handles.SearchWidth = 6;
handles.MaxMin=[];
for i = handles.SearchWidth+1:length(handles.mod_data)-
handles.SearchWidth
    if sum(handles.mod_data(i,2)>handles.mod_data(i-
handles.SearchWidth ...
            :i+handles.SearchWidth,2)) == 2*handles.SearchWidth
        handles.MaxMin = [handles.MaxMin i];
    end
    if sum(handles.mod_data(i,2)<handles.mod_data(i-
handles.SearchWidth ...
            :i+handles.SearchWidth,2)) == 2*handles.SearchWidth
        handles.MaxMin = [handles.MaxMin i];
    end
    if handles.mod_data(i,2)==handles.mod_data(i+1,2)
        if sum(handles.mod_data(i,2)>handles.mod_data(i-
handles.SearchWidth ...
                :i+handles.SearchWidth,2)) >=
2*handles.SearchWidth-2
            handles.MaxMin = [handles.MaxMin i+1];
        end
        if sum(handles.mod_data(i,2)<handles.mod_data(i-
handles.SearchWidth ...
                :i+handles.SearchWidth,2)) >=
2*handles.SearchWidth-2
            handles.MaxMin = [handles.MaxMin i+1];
        end
    end
end

% first and last data point assumed to be max or min (if partial
fringe
% this is taken care of in the displacement analysis). 1st
column is the
% data index, 2nd column if the data value at that index

handles.MaxMin = [1 handles.MaxMin];
handles.MaxMin = [handles.MaxMin length(handles.mod_data)];
handles.MaxMin = handles.MaxMin(:);
handles.MaxMin = sort(handles.MaxMin);
handles.MaxMin(:,2)=handles.mod_data(handles.MaxMin,2);
```

```
if isempty(a)
    % displacement
    handles.flag=0;
    if handles.MaxMin(1,2)<handles.MaxMin(2,2)
        handles.flag=1;
    end

    % check 1st max/min pair for partial fringe, adjust to
adjacted whole
    % half-fringe

    if length(handles.MaxMin)>2 && ...
            abs(handles.MaxMin(1,2)-handles.MaxMin(2,2))<...
            abs(handles.MaxMin(2,2)-handles.MaxMin(3,2))
        handles.MaxMin(1,2)=handles.MaxMin(3,2);
    end

    % check last max/min pair for partial fringe, adjust to
previous whole
    % half-fringe

    if length(handles.MaxMin)>2 && ...
            abs(handles.MaxMin(end,2)-handles.MaxMin(end-
1,2))<...
            abs(handles.MaxMin(end-1,2)-handles.MaxMin(end-2,2))
        handles.MaxMin(end,2)=handles.MaxMin(end-2,2);
    end

    % displacement analysis, for each half fringe the intensity
displacement
    % is determined from eq. (6), incrementing the phase factor
by pi with
    % each new max/min pair

    for i=1:length(handles.MaxMin)-1
        for j=handles.MaxMin(i,1):handles.MaxMin(i+1,1)

handles.Displacement(j)=(asin((handles.MaxMin(i,2)+...
                handles.MaxMin(i+1,2)-...

2*handles.mod_data(j,2))/(abs(handles.MaxMin(i,2)-...
                handles.MaxMin(i+1,2))))*(-1)^...

handles.flag+handles.flag*pi)*handles.Lambda/4/pi;

handles.Displacement(j)=real(handles.Displacement(j));
```

```
        end;
        handles.flag=handles.flag+1;
    end
else
    handles.flag1=0;
    handles.flag2=0;
    if handles.MaxMin(1,2)<handles.MaxMin(2,2)
        handles.flag1=1;
        handles.flag2=1;
    end
    if abs(handles.MaxMin(1,2)-handles.MaxMin(2,2))<...
            abs(handles.MaxMin(2,2)-handles.MaxMin(3,2))
        handles.MaxMin(1,2)=handles.MaxMin(3,2);
    end
    if abs(handles.MaxMin(end,2)-handles.MaxMin(end-1,2))<...
            abs(handles.MaxMin(end-1,2)-handles.MaxMin(end-2,2))
        handles.MaxMin(end,2)=handles.MaxMin(end-2,2);
    end
    %
    for i=1:length(handles.MaxMin)-1
        for j=handles.MaxMin(i,1):handles.MaxMin(i+1,1)

handles.Displacement(j)=(asin((handles.MaxMin(i,2)+...
                handles.MaxMin(i+1,2)-
2*handles.mod_data(j,2))/...
                (abs(handles.MaxMin(i,2)-
handles.MaxMin(i+1,2))))*(-1)^...

handles.flag1+handles.flag2*pi)*handles.Lambda/4/pi;

handles.Displacement(j)=real(handles.Displacement(j));
        end;
        if j==handles.reversal
            handles.flag1=handles.flag1+1;
        end
        handles.flag1=handles.flag1+1;
        handles.flag2=handles.flag2+1;
    end
end

% if only 2 pts for max min, want to scale displacement based on
max and
% min of total data signal (since two points may not represent
true fringe
% peaks or valleys
%
% if length(handles.MaxMin)==2
```

```
%     handles.Displacement=handles.Displacement*...
%          (max(handles.MaxMin(:,2))-
min(handles.MaxMin(:,2)))/...
%          (max(handles.data(:,2))-min(handles.data(:,2)));
% end


% Set initial data point to zero
handles.Displacement=handles.Displacement-
handles.Displacement(1);

% Smooth displacement data
handles.mod_Displacement=handles.Displacement;
for i=1:handles.Sits

handles.mod_Displacement=smooth(handles.mod_Displacement,handles
.Swidth);
end

%
%%%%%%%%%%%%%%%%%%%%%%%%%%%%%%%%%%%%%%%%%%%%%%%%%%%%%%%%%%%%%%%%
% % fit displacement to 8th order fourer
%
handles.FourFit=fit(handles.TimeStep*(0:length(handles.Displacem
ent)-1)',...
%     handles.Displacement','fourier8');
%
handles.mod_Displacement=feval(handles.FourFit,handles.TimeStep*
...
% (0:length(handles.Displacement)-1));
%
%%%%%%%%%%%%%%%%%%%%%%%%%%%%%%%%%%%%%%%%%%%%%%%%%%%%%%%%%%%%%%%%


% Take numerical derivative of the mod_Displacement
% use central difference:

handles.Velocity=(handles.mod_Displacement(3:end)-...
    handles.mod_Displacement(1:end-2))/2/handles.TimeStep;

% Smooth velocity data
for i=1:handles.Sits

handles.mod_Velocity=smooth(handles.mod_Velocity,handles.Swidth)
;
end
```

```
%%%%%%%%%%%%%%%%%%%%%%%%%%%%%%%%%%%%%%%%%%%%%%%%%%%%%%%%%%%%%%%%%%%%%%%%
%%%%%%%%%%
%%%%%%%%%%%%%%%%%%%%%%%%%%%%%%%%%%%%%%%%%%%%%%%%%%%%%%%%%%%%%%%%%%%%%%%%
%%%%%%%%%%
% CHECK HERE ALWAYS TO MAKE SURE THE RIGHT CALCUALTION IS BEING
MADE!     %
%%%%%%%%%%%%%%%%%%%%%%%%%%%%%%%%%%%%%%%%%%%%%%%%%%%%%%%%%%%%%%%%%%%%%%%%
%%%%%%%%%%
%%%%%%%%%%%%%%%%%%%%%%%%%%%%%%%%%%%%%%%%%%%%%%%%%%%%%%%%%%%%%%%%%%%%%%%%
%%%%%%%%%%
% % Calculate substrate stress from velocity - From free surface

handles.SubStress=-
handles.mod_Velocity*handles.SubstrateDensity*...
    handles.WaveSpeedInSubstrate/2/1e3;

% % % Calculate substrate stress from velocity - Windowed
% handles.SubStress=-
handles.mod_Velocity*handles.SubstrateDensity*...
%     handles.WaveSpeedInSubstrate/1e3;

% Take numerical derivative of the mod_Velocity

handles.Acceleration=(handles.mod_Velocity(3:end)-...
    handles.mod_Velocity(1:end-2))/2/handles.TimeStep;

% Smooth acceleration data

handles.mod_Acceleration=smooth(handles.Acceleration,handles.Swi
dth);
for i=1:handles.Sits

handles.mod_Acceleration=smooth(handles.mod_Acceleration,handles
.Swidth);
end

% Calculate interface stress from acceleration

handles.IntStress=-
handles.mod_Acceleration*handles.FilmDesntiy*...
    handles.FilmThickness;

% for thick films calculate based on substress

if (handles.ThickFilm==1 || exist('handles.ThickFilm','var'))
    handles.IntStress=[];
```

```
    handles.IntStress(1:length(handles.SubStress)-
2*handles.HOverC)=...

handles.SubStress(1+2*handles.HOverC:length(handles.SubStress))-
...
        handles.SubStress(1:length(handles.SubStress)-
2*handles.HOverC);
end

close all;

% Output plots using exportfig to make nice figures
% Some useful data

handles.ShotNumber=handles.pname(strfind(handles.pname,'shot'):e
nd-1);
handles.ShotNumber=strrep(handles.ShotNumber,'s','S');
handles.ShotNumber=strrep(handles.ShotNumber,'_',' ');
TmpC=strfind(handles.pname,'\');
handles.AllFigs=[handles.pname(1:TmpC(end-1)) 'AllFigures\'];
handles.FigOpts = struct('Format','png',...
    'Preview','tiff',...
    'Width',8,...
    'Height',6,...
    'Bounds','tight',...
    'Color','bw',...
    'FontMode','fixed',...
    'FontSize',16,...
    'linestylemap','bw');

% Interferometric Signal Plot

figure;
handles.Extra = 200;
handles.Interferometric = handles.data(sum(LB) -
handles.Extra:...
    sum(LB)+length(handles.mod_data) + handles.Extra,2);
plot(-
handles.TimeStep*handles.Extra:handles.TimeStep:handles.TimeStep
*...
    (length(handles.Interferometric)-1-handles.Extra)...
    ,handles.Interferometric);
grid on;
title({'Interferometric
Signal',handles.fname,handles.ShotNumber},...
    'interpreter','none');
xlabel('Time (ns)');
```

```
ylabel('Voltage (V)');
handles.SigXLim=get(gca,'XLim');
handles.SigYLim=get(gca,'YLim');
handles.SigXTick=get(gca,'XTick');
handles.SigYTick=get(gca,'YTick');
handles.SigXTickLabel=get(gca,'XTickLabel');
handles.SigYTickLabel=get(gca,'YtickLabel');
exportfig(gcf,[handles.pname handles.pname(end-2:end-1) ' ' ...
    int2str(gcf) ' Interferometric Signal'],handles.FigOpts);
exportfig(gcf,[handles.AllFigs handles.pname(end-2:end-1) ' '
...
    int2str(gcf) ' Interferometric Signal'],handles.FigOpts);

% Displacement History Plot

figure;
plot(0:handles.TimeStep:handles.TimeStep*...
    (length(handles.mod_Displacement)-
1),handles.mod_Displacement);
grid on;
title({'Displacement',handles.fname,handles.ShotNumber},'interpr
eter','none');
xlabel('Time (ns)');
ylabel('Displacement (nm)');
handles.DisXLim=get(gca,'XLim');
handles.DisYLim=get(gca,'YLim');
handles.DisXTick=get(gca,'XTick');
handles.DisYTick=get(gca,'YTick');
handles.DisXTickLabel=get(gca,'XTickLabel');
handles.DisYTickLabel=get(gca,'YtickLabel');
exportfig(gcf,[handles.pname handles.pname(end-2:end-1) ' ' ...
    int2str(gcf) ' Displacement'],handles.FigOpts);
exportfig(gcf,[handles.AllFigs handles.pname(end-2:end-1) ' '
...
    int2str(gcf) ' Displacement'],handles.FigOpts);

% Substrate Stress History Plot

figure;
plot(0:handles.TimeStep:handles.TimeStep*...
    (length(handles.SubStress)-1),handles.SubStress);
grid on;
title({'Substrate Stress
History',handles.fname,handles.ShotNumber},'interpreter','none')
;
xlabel('Time (ns)');
ylabel('Stress (MPa)');
```

```
handles.SubXLim=get(gca,'XLim');
handles.SubYLim=get(gca,'YLim');
handles.SubXTick=get(gca,'XTick');
handles.SubYTick=get(gca,'YTick');
handles.SubXTickLabel=get(gca,'XTickLabel');
handles.SubYTickLabel=get(gca,'YtickLabel');
exportfig(gcf,[handles.pname handles.pname(end-2:end-1) ' ' ...
    int2str(gcf) ' Substrate Stress History'],handles.FigOpts);
exportfig(gcf,[handles.AllFigs handles.pname(end-2:end-1) ' '
...
    int2str(gcf) ' Substrate Stress History'],handles.FigOpts);

% Interface Stress History Plot

if (handles.FilmThickness~=0)
    figure;
    plot(0:handles.TimeStep:handles.TimeStep*...
        (length(handles.IntStress)-1),handles.IntStress);
    grid on;
    title({'Interface Stress
History',handles.fname,handles.ShotNumber},'interpreter','none')
;
    xlabel('Time (ns)');
    ylabel('Stress (MPa)');
    handles.IntXLim=get(gca,'XLim');
    handles.IntYLim=get(gca,'YLim');
    handles.IntXTick=get(gca,'XTick');
    handles.IntYTick=get(gca,'YTick');
    handles.IntXTickLabel=get(gca,'XTickLabel');
    handles.IntYTickLabel=get(gca,'YtickLabel');
    exportfig(gcf,[handles.pname handles.pname(end-2:end-1) ' '
...
        int2str(gcf) ' Interface Stress
History'],handles.FigOpts);
    exportfig(gcf,[handles.AllFigs handles.pname(end-2:end-1) '
' ...
        int2str(gcf) ' Interface Stress
History'],handles.FigOpts);
end

% Subplot

handles.SubOpts = struct('Format','png',...
    'Preview','tiff',...
    'Width',8,...
    'Height',6,...
    'Bounds','tight',...
```

```
    'Color','bw',...
    'FontMode','fixed',...
    'FontSize',14,...
    'linestylemap','bw');
if (handles.FilmThickness==0)
    figure;
    subplot(2,2,1:2);
    plot(-handles.TimeStep*handles.Extra:...
        handles.TimeStep:handles.TimeStep*...
        (length(handles.Interferometric)-1-handles.Extra)...
        ,handles.Interferometric);
    grid on;
    %    title({'Interferometric Signal'},'interpreter','none');
    xlabel('Time (ns)');
    ylabel('Photodiode output (V)');
    set(gca,'XLim',handles.SigXLim);
    set(gca,'YLim',handles.SigYLim);
    set(gca,'XTick',handles.SigXTick);
    set(gca,'YTick',handles.SigYTick);
    set(gca,'XTickLabel',handles.SigXTickLabel);
    set(gca,'YTickLabel',handles.SigYTickLabel);
    subplot(2,2,3);
    plot(0:handles.TimeStep:handles.TimeStep*...
        (length(handles.mod_Displacement)-
1),handles.mod_Displacement);
    grid on;
    %    title({'Displacement'},'interpreter','none');
    xlabel('Time (ns)');
    ylabel('Displacement (nm)');
    set(gca,'XLim',handles.DisXLim);
    set(gca,'YLim',handles.DisYLim);
    set(gca,'XTick',handles.DisXTick);
    set(gca,'YTick',handles.DisYTick);
    set(gca,'XTickLabel',handles.DisXTickLabel);
    set(gca,'YTickLabel',handles.DisYTickLabel);
    subplot(2,2,4);

plot(0:handles.TimeStep:handles.TimeStep*(length(handles.SubStre
ss)-1),handles.SubStress);
    grid on;
    %    title({'Substrate Stress
History'},'interpreter','none');
    xlabel('Time (ns)');
    ylabel('Substrate stress (MPa)');
    set(gca,'XLim',handles.SubXLim);
    set(gca,'YLim',handles.SubYLim);
    set(gca,'XTick',handles.SubXTick);
```

```
    set(gca,'YTick',handles.SubYTick);
    set(gca,'XTickLabel',handles.SubXTickLabel);
    set(gca,'YTickLabel',handles.SubYTickLabel);
    hout=suptitle_withpatch({handles.fname,handles.ShotNumber,'
'});...
        %       ['Filter Frequency =
',num2str(handles.FourierFilterFreq),' GHz'],' '});
    set(hout,'interpreter','none');
    exportfig(gcf,[handles.pname handles.pname(end-2:end-1) ' '
...
        int2str(gcf) ' SubPlot'],handles.SubOpts);
    exportfig(gcf,[handles.AllFigs handles.pname(end-2:end-1) '
' ...
        int2str(gcf) ' SubPlot'],handles.SubOpts);

hout=suptitle_withpatch({handles.fname,handles.ShotNumber,...
        ['Filter Frequency =
',num2str(handles.FourierFilterFreq),' GHz'],' '});
    set(hout,'interpreter','none');
    exportfig(gcf,[handles.pname handles.pname(end-2:end-1) ' '
...
        int2str(gcf) ' '
strrep(num2str(handles.FourierFilterFreq),...
        '.','_') 'Ghz' ' SubPlot'],handles.SubOpts);
else
    figure;
    subplot(2,2,1);
    plot(-handles.TimeStep*handles.Extra:handles.TimeStep:...
        handles.TimeStep*(length(handles.Interferometric)-1-
handles.Extra)...
        ,handles.Interferometric);
    grid on;
    %    title({'Interferometric Signal'},'interpreter','none');
    xlabel('Time (ns)');
    ylabel('Photodiode output (V)');
    set(gca,'XLim',handles.SigXLim);
    set(gca,'YLim',handles.SigYLim);
    set(gca,'XTick',handles.SigXTick);
    set(gca,'YTick',handles.SigYTick);
    set(gca,'XTickLabel',handles.SigXTickLabel);
    set(gca,'YTickLabel',handles.SigYTickLabel);
    subplot(2,2,2);
    plot(0:handles.TimeStep:handles.TimeStep*...
        (length(handles.mod_Displacement)-
1),handles.mod_Displacement);
    grid on;
    %    title({'Displacement'},'interpreter','none');
```

```
    xlabel('Time (ns)');
    ylabel('Displacement (nm)');
    set(gca,'XLim',handles.DisXLim);
    set(gca,'YLim',handles.DisYLim);
    set(gca,'XTick',handles.DisXTick);
    set(gca,'YTick',handles.DisYTick);
    set(gca,'XTickLabel',handles.DisXTickLabel);
    set(gca,'YTickLabel',handles.DisYTickLabel);
    subplot(2,2,3);

plot(0:handles.TimeStep:handles.TimeStep*(length(handles.SubStre
ss)-1),handles.SubStress);
    grid on;
    %    title({'Substrate Stress
History'},'interpreter','none');
    xlabel('Time (ns)');
    ylabel('Substrate stress (MPa)');
    set(gca,'XLim',handles.SubXLim);
    set(gca,'YLim',handles.SubYLim);
    set(gca,'XTick',handles.SubXTick);
    set(gca,'YTick',handles.SubYTick);
    set(gca,'XTickLabel',handles.SubXTickLabel);
    set(gca,'YTickLabel',handles.SubYTickLabel);
    subplot(2,2,4);

plot(0:handles.TimeStep:handles.TimeStep*(length(handles.IntStre
ss)-1),handles.IntStress);
    grid on;
    %    title({'Interface Stress
History'},'interpreter','none');
    xlabel('Time (ns)');
    ylabel('Interface stress (MPa)');
    set(gca,'XLim',handles.IntXLim);
    set(gca,'YLim',handles.IntYLim);
    set(gca,'XTick',handles.IntXTick);
    set(gca,'YTick',handles.IntYTick);
    set(gca,'XTickLabel',handles.IntXTickLabel);
    set(gca,'YTickLabel',handles.IntYTickLabel);
    hout=suptitle_withpatch({handles.fname,handles.ShotNumber,'
'});
    set(hout,'interpreter','none');
    exportfig(gcf,[handles.pname handles.pname(end-2:end-1) ' '
...
        int2str(gcf) ' SubPlot'],handles.SubOpts);
    exportfig(gcf,[handles.AllFigs handles.pname(end-2:end-1) '
' ...
        int2str(gcf) ' SubPlot'],handles.SubOpts);
```

```
end

% close all figures, pause so user can see any obvious issues
and is
% reanalysis is needed

pause;
close all;

% Save Workspace Data
% Make filename

handles.AllData=[handles.pname(1:TmpC(end-1)) 'AllData\'
handles.ShotNumber ' data'];
save(handles.AllData);
save([handles.pname handles.ShotNumber ' data']);

% display shot number of analysis just performed to inform user
handles.ShotNumber
```